Elisabeth Wruß, BSc

Influence of van der Waals interactions on the adsorption of flat-lying organic molecules on metallic surfaces

MASTER THESIS

For obtaining the academic degree
Diplom-Ingenieur

Master Programme of
Technical Physics

Graz University of Technology

Supervisor:

Ao.Univ.-Prof. Dipl.-Ing. Dr.techn. Egbert Zojer

Institute of Solid State Physics

Graz, April 2014

Deutsche Fassung:
Beschluss der Curricula-Kommission für Bachelor-, Master- und Diplomstudien vom 10.11.2008
Genehmigung des Senates am 1.12.2008

EIDESSTATTLICHE ERKLÄRUNG

Ich erkläre an Eides statt, dass ich die vorliegende Arbeit selbstständig verfasst, andere als die angegebenen Quellen/Hilfsmittel nicht benutzt, und die den benutzten Quellen wörtlich und inhaltlich entnommenen Stellen als solche kenntlich gemacht habe.

Graz, am …… ……..
(Unterschrift)

Englische Fassung:

STATUTORY DECLARATION

I declare that I have authored this thesis independently, that I have not used other than the declared sources / resources, and that I have explicitly marked all material which has been quoted either literally or by content from the used sources.

…… ……..
date (signature)

Acknowledgements

At this point I would like to mention several people and organisations who supported me during my thesis.
Special thanks go to my supervisor, Egbert Zojer, who guided and supported me. I also want to thank the former and current members of his group at Graz University of Technology, David Egger, Manuel Vieider, Iris Hehn, Bernhard Kretz, Elisabeth Verwüster, Veronika Obersteiner, Gernot Kraberger, Thomas Taucher and Shashank Harivyasi. David Egger taught me a lot about the basics of this field and the application of the computational methods.
Several parts of this thesis are based on previous work by Yu Li Huang (National University of Singapore). In addition to providing her data, she also helped with scientific advice during our fruitful collaboration.
Oliver T. Hofmann (Fritz-Haber-Institut der Max-Planck-Gesellschaft, Berlin, Germany) and Georg Heimel (Humboldt-Universität zu Berlin, Germany) kindly provided unit cell geometries for certain systems I simulated and supported me with the calculations.
The applied vdW^{surf} codes were programmed by Wissam A. Saidi (University of Pittsburgh, United States) and Tomáš Bučko (Comenius University, Bratislava, Slovakia), who also helped me to understand the functionality and differences of their implementations. Tomáš Bučko additionally performed test calculations, modified parts of the code to resolve inconsistencies and helped with numerous application difficulties. He also provided a code version modified especially for our needs.
Finally, I want to thank my parents and friends for their moral support.
I gratefully acknowledge financial support by the Austrian Science Fund
(FWF): P24666-N20.
All calculations have been performed using the i-cluster and the d-cluster of the scientific computing department at the Graz University of Technology.

Abstract

In the scientifically highly active field of organic electronics, computational methods are of great importance, as they allow quick and simple modelling of various kinds of systems. Additionally, they provide deeper insight into the processes occurring at a microscopic level. One of the most versatile and widely used computational methods in this area is density functional theory (DFT).

This work presents an extensive DFT study on the adsorption of organic molecules on coinage metal surfaces, focusing mainly on the influence of van der Waals (vdW) interactions. These non-local electron-electron interactions are not accounted for in standard local and semi-local DFT, which prevents the treatment of "weakly" interacting interfacial systems, where vdW forces are often of crucial importance. Several approaches to overcome this shortcoming have been presented recently, one of them being the vdW^{surf} energy correction method by Ruiz et al. (Phys. Rev. Lett. 108, 2012). Based on the parameter-free *vdW-TS* approach by Tkatchenko et al. (Phys. Rev. Lett. 102, 2009), vdW^{surf} also accounts for many-body collective response effects of the metallic substrate, the so-called *screening*, by including the Lifshitz-Zaremba-Kohn theory. It is, therefore, very well-suited to describe adsorption processes on metallic substrates.

The main goal of this work was to benchmark the performance of vdW^{surf} for flat-lying organic molecules like phthalocyanines and pentacene derivatives on coinage metal fcc(111) surfaces.

As it has been shown in several earlier works, applying the *PBE* functional in combination with vdW^{surf} provides good results in most cases, although problems may arise when the surface unit cell is unknown or when the considered structure is in an intermediate state between physisorptive and chemisorptive bonding.

Although physisorption is generally considered to be a "weak" interaction, comparatively large binding energies due to van der Waals interactions in the range of several eV per molecule were found.

As soon as the adsorption geometries were known, further effort was put into the investigation of the electronic structure of the interfaces. The analysis of orbital ordering, charge rearrangements and work function modification due to adsorption led to a deeper understanding of the bonding processes at the examined interfaces and demonstrated the multitude of interactions responsible for the formation of hybrid metal-organic interfaces.

In addition to standard $PBE + vdW^{surf}$ simulations, the investigation of some systems required the use of hybrid functionals to analyse the electronic structure. These calculations turned out to be of great benefit for the description of bonding processes, as they allow to model orbital ordering more accurately.

Kurzfassung

Computersimulationen sind wichtige Methoden im hochaktuellen Forschungsgebiet der organischen Elektronik, da sie sowohl schnelle und einfache Untersuchungen von verschiedenartigen Systemen erlauben, als auch Einblick in die Vorgänge auf mikroskopischem Level gewähren. Eine der vielseitigsten und meistverwendeten Methoden in diesem Bereich ist die sogenannte Dichtefunktionaltheorie (DFT).
Die vorliegende Arbeit befasst sich mit DFT-Simulationen der Adsorption von organischen Molekülen auf Metalloberflächen, wobei besonderes Augenmerk auf den Einfluss der van der Waals (vdW) Wechselwirkungen gelegt wird. Diese nichtlokalen Wechselwirkungen zwischen Elektronen sind insofern von besonderem Interesse, als sie in den (semi-) lokalen Näherungen der Dichtefunktionaltheorie nicht korrekt beschrieben werden. Das führt zu Problemen mit der Modellierung von schwach wechselwirkenden metallorganischen Systemen, in denen der Einfluss von vdW-Kräften meist von großer Wichtigkeit ist. Verschiedenste Ansätze ermöglichen die Berücksichtigung dieser Wechselwirkungen in DFT, beispielsweise die Energiekorrekturmethode vdW^{surf} von Ruiz et al. (Phys. Rev. Lett. 108, 2012). Für diese wurde der zugrunde liegende Ansatz *vdW-TS*, vorgestellt von Tkatchenko et al. (Phys. Rev. Lett. 102, 2009), um die Lifshitz-Zaremba-Kohn-Theorie erweitert, sodass Vielteilcheneffekte des Substrats, die sogenannte *Abschirmung*, inkludiert werden können. Daher ist vdW^{surf} gut geeignet, um die hier behandelten Adsorptionsprozesse auf metallischen Oberflächen zu beschreiben. Das Hauptziel der vorliegenden Arbeit war es, diese Methode im Zusammenhang mit Grenzflächenberechnungen von flach liegenden organischen Molekülen wie Phthalocyaninen und Pentacen-Derivaten auf fcc(111)-Metalloberfächen zu testen. Dabei war der erste Schritt stets das Finden der Adsorptionsgeometrie.
Die Kombination des *PBE*-Funktionals mit vdW^{surf} führt in vielen Fällen zu guten Ergebnissen, obwohl es zu Problemen kommen kann wenn die Oberflächen-Einheitszelle nicht bekannt ist oder eine Situation an der Grenze zwischen Physisorption und Chemisorption vorliegt. Physisorptive Bindungen werden im Allgemeinen als "schwache" Wechselwirkungen beschrieben, was im Kontrast zu den vergleichsweise hohen Bindungsenergien von einigen eV pro Molekül durch vdW-Kräfte steht, die für die hier behandelten Systeme gefunden wurden.
Nach der Berechnung der Adsorptionsgeometrien konnten auch die elektronischen Strukturen der Grenzflächen analysiert werden. Zur Untersuchung der Bindungsprozesse wurden die Anordnungen der Orbitale und die durch die Adsorption verursachten Ladungsdichteverschiebungen und Austrittsarbeitsänderungen betrachtet. Dabei zeigte sich, dass die Bindung zwischen Metallen und organischen Molekülen durch eine Vielzahl von Wechselwirkungen verursacht wird. In einigen Fällen wurden die metallorganischen Grenzflächen zusätzlich zu den Simulationen mit dem bereits oben genannten *PBE*-Funktional auch mit Hybridfunktionalen modelliert, was sich als sehr nützlich für die Untersuchung der elektronischen Struktur erwies, da die Anordnung der Molekülorbitale mittels dieser Funktionale besser beschrieben werden kann.

Contents

Acronyms

DFT	density functional theory
DOS	density of states
vdW	van der Waals
SCF	self-consistent field
XSW	x-ray standing wave
UPS	ultraviolet photoelectron spectroscopy
GGA	the generalized-gradient approximation in DFT
PBE	the Perdew-Burke-Enzerhof exchange-correlation functional [1]
HSE	the Heyd-Scuseria-Ernzerhof hybrid functional [2]
HOMO	highest occupied molecular orbital
LUMO	lowest unoccupied molecular orbital
EA	electron affinity
IE	ionisation energy
CuPc	the copper phthalocyanine molecule
ZnPc	the zinc phthalocyanine molecule
SnPc	the tin phthalocyanine molecule
P2O	the pentacenequinone molecule
P4O	the pentacenetetrone molecule
GaClPc	the chlorgallium phthalocyanine molecule
PTCDA	the 3,4,9,10-perylene-tetracarbonxylic-dianhydrid molecule
vdW-TS	the vdW-correction method by Tkatchenko and Scheffler [3]
vdW^{surf}	the vdW-correction method by Ruiz et al. [4]
V5.3	VASP 5.3. with the *vdW^{surf}* extension by Wissam A. Saidi
V5.2.11(TS)	VASP 5.2.11 with the *vdW-TS* extension by Wissam A. Saidi [5]
V5.3.3	VASP 5.3.3 with *vdW-TS* implemented by default
sVDW	simulations using VASP 5.3.3 where the vdW interactions are switched off between the substrate atoms

1 Introduction

The present work documents a series of density functional theory calculations on interfaces consisting of flat-lying organic molecules adsorbed on metal substrates.
The first question one should be concerned with when presenting a project like this one is the motivation. Why was it useful to perform these simulations, and what were the desired achievements?
The most general answer to this question is, in this case, to reach a better understanding of metal-organic interfaces. This highly active field of research, positioned at an intersection of physics, chemistry and material sciences concerns itself with the basic principles of organic electronics. Devices based on organic materials offer various benefits compared to standard silicon-based semiconductors as mechanical flexibility, the possibility to be printed onto a substrate and direct band gaps, especially in the optical region [6]. Therefore, the adsorption of organic semiconductors on metal electrodes is of interest for the research on light-emitting devices like organic light emitting diodes, light-sensitive devices, sensors, organic transistors, and many more [7]. The function of the organic component can range from tuning the charge injection properties of a electrode to being the central piece of an electronic device.
The number of available organic semiconductor materials is huge, which offers an endless variety of metal-organic systems to investigate. Therefore, computational methods which allow studying geometrical as well as electronic properties of most kinds of systems are a commonly employed approach. Density functional theory (DFT) is the method of choice as it offers good results in most cases of high accuracy at comparably low computational effort [8].
This leads to the actual motivation of the present work: Although density functional theory is a tool of significant power, it still contains some flaws, one of them being the negligence of long-range van der Waals interactions in all common local and semi-local functionals [9]. To overcome this shortcoming several approaches have been proposed, including the non-self consistent energy correction method vdW^{surf} [4] which has been successfully applied on various metal-organic interfaces [4, 10]. One of the goals of this work was to benchmark vdW^{surf} for several other systems, namely metal phthalocyanine and pentacene derivative molecules on coinage metal surfaces. Also more complex systems, like the non-planar chlorgallium phthalocyanine were treated.
For every investigated system, the first target was to find an accurate adsorption geometry. To verify the obtained results, mainly systems for which experimental information on the adsorption geometry is available were chosen. With the system geometry at hand, it was possible to look deeper into the electronic structure at the interface to come to a better understanding of the bonding mechanisms at metal-organic interfaces.

1.1 Investigated properties

The main task for every system was the geometry optimisation, which was performed applying the Vienna Ab Initio Simulation Package VASP [11] and the geometry-optimisation software GADGET [12]. The bonding distances to the surface, positioning and rotation as well as deformation of the molecules were evaluated. If possible the results were compared to experimental data. In this context x-ray standing wave (XSW) results allowing the determination of bonding distances were of special interest.
Information on the bonding distance gives a first clue on the binding mechanism [13]. Small bonding distances below 3 Å hint strong chemisorptive bonding, while distances above 3 Å are a sign of a weak, physisorptive interaction.
Deeper insight into the adsorption mechanism can be gained by looking at the electronic properties of the interface. The first values to examine in this respect are the work-function of the metal and the work function modification due to adsorption. These values are closely related to the charge rearrangements caused by the bonding process between adsorbate layer and substrate. Also the density of states of the organic layer and the positions of the molecular orbitals relative to the Fermi energy of the metal, especially the highest occupied molecular orbital HOMO and the lowest unoccupied molecular orbital LUMO, are relevant. All these properties can be used to draw conclusions on the interaction of the molecules with each other within the adsorbate layer and on the bonding mechanisms between metal and organics.

1.2 Overview

This work starts with a summary of the important fundamental concepts of metal-organic interfaces, van der Waals interactions and density functional theory, including hybrid functionals. Also the possible approaches to include van der Waals interactions are reviewed and the method vdW^{surf} is explained in more detail (Sec. 2). The applied DFT code, VASP, is introduced and important approaches and parameters, which were used in the following, are mentioned briefly (Sec. 3). Moreover, basic tests on different calculation methods, metal lattice constants and unit cells which were performed prior to the actual simulations are summarized (Sec. 4). Subsequently, the results of geometry optimisations on various investigated systems, namely metal phthalocyanines and pentacene derivatives on coinage metal surfaces are presented (Sec. 5). Finally, the electronic structure of the the copper and zinc phthalocyanine molecules adsorbed on Au(111) and Ag(111) surfaces is discussed extensively (Sec. 6). The latter results have been published in Ref. [14] with Yu Li Huang and the author of this work acting as equally contributing first authors.

2 Fundamentals and theoretical background

2.1 Van der Waals forces

The following considerations are based on the general overview of van der Waals interactions in Ref. [15].

The discussion of van der Waals forces is a logical starting point, as the main focus of this work was on testing and applying vdW^{surf}, a method which is designed to include van der Waals interactions at metal surfaces into standard DFT calculations. Therefore, the concept of these forces is necessary for many basic considerations, methodological details and computational findings which are to follow.

Generally speaking, one can distinguish between three different kinds of vdW interactions: Keesom-, Debye- and London-interactions.

- Keesom interactions: These are the electrostatic interactions of several permanent dipoles which would be oriented randomly due to rotational freedom if they were interaction-free. But due to these interactions the randomness of the dipolar orientation in the system is perturbed, which results in a net attractive energy. Alignment of two dipoles in opposite directions leads to an attractive force between the particles, varying with the inverse third power of the distance if the dipoles are fixed. But in the case of freely rotating dipoles it depends on the inverse sixth power of the distance.
- Debye interactions: A particle with a permanent dipole which is brought close to a nonpolar particle induces a dipolar moment of opposite direction in the latter. The oppositely directed dipoles attract each other.
- London interactions: So-called London dispersion interactions appear between nonpolar particles which are polarizable. Due to charge fluctuations, instantaneous dipoles arise, which induce a dipolar moment in other polarizable particles. The result is a coupled movement of electrons in both systems, which lowers the total energy of the system and causes the particles to attract one another. The term "dispersion forces" stems from the frequency-dependency of the interaction; it can only appear if the particles share a resonance frequency and can, therefore, couple.

For all different kinds of vdW interactions the free energy varies with the inverse sixth power of the distance of the interacting objects.

$$E_{vdW} \propto \frac{C_{vdW}}{r^6} \tag{1}$$

The vdW coefficient C_{vdW} differs for the different kinds of interactions and interacting systems.

The dispersion interaction

Usually, the London dispersion forces are the dominating part of the above mentioned interactions. The terms *van der Waals interactions* and *dispersion interactions* are often used interchangeable, both referring to London dispersion forces, which is also the case in this work. vdW forces are generally considered to be "weak" interactions, as they are weaker than chemical covalent or ionic bonds. But in many cases they can be of considerable importance for the behaviour of a system, like the formation of noble-gas crystals at low temperatures or physisorption of molecules at surfaces [9]. In the latter case, the interacting surface area plays a crucial role, as the dispersion forces add up over the mutual surface region of two interacting systems.

The charge density of the electrons of an atom with filled electron shells should in principle have a matching center of mass with the atomic nucleus. Therefore, the atom appears neutral. But this is only the case, if the time average of the charge density is considered. At a specific point in time, the central-symmetric charge distribution of the electrons is disturbed due to the constant motion of the electrons. So the the center of mass of the charge density does momentarily not match the position of the nucleus and the atoms has a dipolar moment.

The dispersion interaction of two nonpolar particles, which interact due to mutual induction can be modelled using point dipoles [16, 17]. Due to the charge fluctuations, the first particle, for example a neutral atom, exhibits a dipole moment p_1. A neighbouring particle at the distance r will feel an electric field $E \propto \frac{p_1}{r^3}$. If it is polarizable it will exhibit charge rearrangement due to the field of this dipole and will itself be an induced dipole, with the induced dipole moment $p_2 \propto \frac{p_1}{r^3}\alpha$ with α denoting the polarizability. This leads to the attractive potential between two interacting particles, which is proportional to the electric field of the first and the induced dipole moment of the second dipole and therefore exhibits the characteristic $\frac{1}{r^6}$ behaviour [16, 17].

The interaction potential of the two particles can be written as

$$E_{pot}(r) = -C_{vdW}\frac{\alpha_A \alpha_B}{r^6} \tag{2}$$

with the vdW coefficient C and the polarizabilities of the atoms α_A and α_B.

So why are these dispersion interactions so interesting in the context of DFT investigations of metal-organic interfaces?

First, bonding of the considered systems consisting of flat-lying organic molecules on metal surfaces is mostly dominated or at least strongly influenced by vdW interactions. Second, their treatment in (semi-) local DFT is a problematic matter. Dispersion forces are non-local electron-electron interactions, due to the response of electrons in one region to charge fluctuations of electrons in a distant region. Most DFT functionals, on the other hand, are semi-local or local approximations to keep the computational effort manageable [9]. Therefore, they fail to include vdW forces, which prohibits the

description of physical interactions at interfaces. How this problem can be overcome will be discussed extensively in the following chapters.

2.2 Metal-organic interfaces

When studying the effects of adsorption on metal-organic interfaces, first one needs to recall the electronic structure of the interaction-free systems [18]. The metal substrate is held together by metallic bonds, where the positively charged nuclei are more or less fixed to their grid position, while the electrons form an electron gas and are delocalized over the whole crystal. The Fermi energy lies within a partly filled band.
An organic molecule, on the other hand, is held together by covalent bonds and exhibits discreet energy levels. The highest occupied molecular orbital (HOMO) and the lowest unoccupied molecular orbital (LUMO) are separated by an energy gap. The Fermi energy lies within this gap.
When the two materials are brought into contact, interaction effects appear [18].
In principle one can distinguish between two kinds of adsorption behaviours, namely physisorption and chemisorption [16, 17]. While physisorption is a "weak" interaction solely due to physical effects, chemisorption appears due to "strong" chemical bonding. These definitions of bonding processes are somehow problematic, as it is not always possible to define a system as exhibiting "strong" chemisorptive or "weak" physisorptive interactions. The type and strength of the interactions depend on several factors, including, of course, the involved materials but also the preparation of the surface [19]. Also the term *"weak" interaction* should not be applied carelessly. As mentioned in the previous chapter, vdW forces add up over the mutual areas of interacting bodies. Therefore the total value of the vdW interaction energy can become formidable, for example, for large molecules adsorbing an a substrate, like it was shown for PTCDA on Ag(111), where the vdW energy adds up to several eV per molecule [10].

2.2.1 Physisorption

Physisorpion is a surface bonding process, where the electronic structure of the adsorbed molecule or atom as well as the electronic structure of the solid substrate is hardly perturbed [16]. The bonding processes happens due to van der Waals forces, precisely due to London dispersion forces. The (neutral) bonding partners exhibit correlated charge fluctuations, which lead to an attractive interaction [16].
As explained earlier, the attraction of two nonpolar particels due to vdW forces can be approximately expressed as a $\frac{1}{r^6}$-potential [16]. For a particle adsorbing on a material and therefore interacting with an infinite halfspace the situation is different.

A particle with charge q_1 which lies above a surface with a dielectric constant ϵ induces an image point charge $q_2 = \frac{1-\epsilon}{1+\epsilon} q_1$ within the surface. For a metallic surface, $\epsilon = \infty$ and therefore $q_1 = q_2$. The interaction of the atom and the surface can be described as the interaction of the atom and its image [16]. So in this case the vdW interaction is a screening effect, where the charge of the nucleus and the charge of the electrons interact with their image charges. Writing down the potential one finds that it is proportional to the inverse third power of the distance z between the particle and the mirror plane $V(z) \propto \frac{1}{z^3}$ [16]. When defining the distance z one has to consider the fact that there is a decaying electron cloud right outside the surface, so the charge density "leaks" out of the material [20].
Equilibrium separations of physisorbed particles from the surface are mostly higher than 3 Å, and the binding energy per atom is between 10 and 100 meV [16]. Because of the large bonding distances and the fact that, e. g., in case of a molecule, the attractive force is distributed over the whole system (as interaction appears between all fragments of the molecule and the substrate) the adsorbed structure is often quite mobile on the surface [16].

2.2.2 Chemisorption

While physisorption is solely due to charge fluctuation effects, bonding due to orbital overlap and actual perturbation of the electronic structure is called chemisorption. Chemical binding processes as covalent and/or ionic interactions appear, leading to charge transfer between the fragments and/or the formation of hybrid orbitals [16]. It mostly leads to smaller bonding distances below 3 Å [16]. In case of (flat-lying) molecules on substrates with covalent bonding it also leads to larger deformations of the molecules compared to physisorption. This is due to the bonding process being a direct interaction of a part of the molecule with the substrate, while physisorptive interactions due to vdW forces act similar on the whole molecule. Chemisorption can also lead to the dissociation of the adsorbed molecule [16].

2.2.3 The work function

The work function ϕ of a surface is defined as the difference between the materials Fermi level E_{Fermi} and the vacuum energy E_{vac} [16, 18].

$$\phi = E_{vac} - E_{Fermi} \tag{3}$$

The adsorption of atoms or molecules on a substrate influence the electronic structure and, therefore, the work function of the system. This change is called the the work-function modification, $\Delta\phi$, and consists of two parts. First the dipole moment of the

molecule itself changes the work function (ΔE_{mol}), and, secondly, charge rearrangements due to the adsorption (ΔE_{bond}) appear [19, 21].

$$\Delta\phi = \Delta E_{mol} + \Delta E_{bond} \tag{4}$$

The influence of charge transfer, ΔE_{bond}, can either increase or decrease the work function. In case of charge transfer to the molecule, an upwards shift of the vacuum level happens, while charge transfer from the molecule to the substrate causes a down-shift, because a dipole-induced potential step appears at the interface [19]. Noteworthy there is also a work function modification due to charge transfer when the adsorbate interacts only physisorptive. This is caused by the the so-called *push-back* (or *pillow*) effect [22], which arises from the adsorbate pushing the electronic tail "leaking out" of the substrate back toward the surface. This effect causes a lowering of the work function [19, 22, 23].

2.2.4 Modification of the electronic structure due to adsorption

Many properties of metal-organic interfaces are determined by the relative positions of the Fermi energy of the metal and the energy levels of the organic system, most importantly the HOMO and the LUMO, which are the relevant electronic transport levels [18]. The coupling of the molecular states to metal states determines how charge transport through the interface works [19, 18]. These properties are generally denoted as energy level alignment and are one of the most important aspect of the interface electronic structure. Another important aspect is band bending, which was of less relevance for this work as only monolayer structures were investigated. Band bending mainly becomes relevant for a thicker layer of organic adsorbate, as it demands a large number of mobile charge carriers [24]. Molecules which are close enough to each other can form molecular solids through non-covalent bonds. Electrons which were delocalized in the π-conjugated systems of a single molecules first can now move more ore less freely in delocalized states which spreads out over several molecules due to the intermolecular interactions [24]. This leads to a transformation of the discrete energy levels of the single molecule to energy bands. If they are close enough to share one interface and if the electrons are in thermodynamic equilibrium, the Fermi levels of the organic bulk and the metal align due to band bending [18, 24].
For a monolayer structure, the simplest model of the interaction of a metal and an organic adsorbate can be described through the metal work function ϕ, the electron affinity EA and the ionization energy IE of the organic compound. The electron affinity can be approximated by the difference between the LUMO and the vacuum level E_{vac}, while IE can be approximated by difference between HOMO and E_{vac}. The work function, as mentioned earlier, gives the difference between the metal Fermi level and its vacuum energy [24].

In the approximation for minimal interaction, the electronic structure of the interface can simply be described by the alignment of the vacuum levels of both systems. The energy differences between HOMO / LUMO and the Fermi energy are called the electron / hole injection barrier, respectively. These barriers need to be overcome to realize electron or hole transport through the interface.
If the Fermi level lies within the (tail of the) peak of the HOMO or LUMO energy, it gets "pinned" to the edges of the organic gap [18]. This means the penetration of the Fermi level deep into the occupied or unoccupied states below the HOMO or above the LUMO, respectively, is avoided by partial emptying/filling the HOMO or LUMO. These charge exchange shifts the levels in a way that the Fermi level again lies within (at the edge of) the gap [18, 24].
The previous chapter lists some possible causes for the modification of the work function. With the picture of level alignment at hand it is now possible to give a more general overview of the causes for a vacuum level shift, which is linked to a work-function modification. These typically involve the formation of an additional interface dipole [24]:

- Charge transfer between the metal and the molecular layer occurs, e.g. due to the formation or change of chemical bonds, which might lead to a higher or lower vacuum level.
- The surface dipole, which arises from the tailing of the electron cloud outside of a metal surface, is modified due to the *push-back* effect. The Pauli repulsion of the electron cloud of the adsorbate and the tailing electron cloud of the metal pushes the latter back towards the surface, and the vacuum level is lowered.
- The electron cloud of the adsorbate is polarized due to the formation of an image charge inside the metal substrate, which results in an attractive "mirror" force, also lowering the vacuum level.
- Interfacial states, for example due to metal-organic gap states, which are formed when the metal wavefunctions penetrate into the adsorbate layer, causes charge exchange.
- Adsorption of molecules with a permanent dipole moment shift the vacuum level, with the direction of the shift depending on the direction of the dipole.

Visualisation of charge rearrangements
Adsorption processes generally causes charge rearrangements at metal surfaces. They depend on several factors, including the adsorption distance, the work function of the metal and the donor/acceptor strength of the adsorbed molecules [24]. To shed light onto the details of the bonding at a surface, it is, therefore, interesting to look at the charge redistribution, $\Delta\rho$. It is calculated from the charge density of the interacting system ρ_{sys} and the charge densities of the independent parts, the substrate ρ_{subst} and the monolayer ρ_{ml}, applying the unit cell and geometry which were used for the system

also for the system parts [23, 25].

$$\Delta\rho = \rho_{sys} - \rho_{subst} - \rho_{ml} \tag{5}$$

To visualize $\Delta\rho$, one can either print it in 3D using isodensity plots or integrate/average the charge density over the x-y-plane and print it along the z-direction (with the z-direction being the one perpendicular to the surface). Another useful quantity in this context is the cumulative charge rearrangement (net charge transfer) $Q(z)$, which is derived by integrating $\Delta\rho(z)$ over z and gives the total amount of charge that is shifted from the left of a plane at position z to its right [23, 25, 26].

$$Q(z) = \int_0^z \Delta\rho(z')dz' \tag{6}$$

Another possible way to analyse charge transfer is raised by the density of states (DOS). The molecular orbitals of a system experience changes in occupation arising from the metal-organic interaction, which can be seen in the DOS. In principle, broadening of the molecular states appears as hybridisation between the metal and the organic states occurs, with the broadening depending on the strength of hybridisation [27]. This effect is mostly not visible in DFT results due to artificial broadening, which is necessary for convergence reasons (see Sec. 3). The hybridized states can be fully or partially filled, with partial filling occurring commonly if a state lies close to the Fermi energy [27].

2.3 Density-functional theory

Several approaches exist to describe correlated many-body systems in a quantum-mechanical manner. One of the most widely used approaches is density-functional theory (DFT). The fundamental idea of DFT is that a system consisting of many interacting particles can be described using the ground state density $n_0(\mathbf{r})$, which contains all the information of the ground state many-body wavefunctions [8]. The properties of the systems, for example the total energy, are functionals of the ground state density [28]. The complexity and the computational effort needed to describe a many-electron system with N electrons is massively reduced by using the electron density instead of 3N spatial coordinates [8].
Originally, the first density functional approach was already formulated in 1927 by Thomas and Fermi, where the kinetic energy of a many-electron systems is described as a functional of the density. Although exchange and correlation among the electrons are neglected and the practical applicability of the Thomas-Fermi method is very limited, it set a starting point for modern day DFT electronic structure calculations [8].

2.3.1 The Hoheberg-Kohn theorems

Hohenberg and Kohn formulated two theorems to describe particles in an external potential $V_{ext}(\mathbf{r})$, like electrons in the field of atomic nuclei. These theorems serve as the basis for DFT [28].
The first theorem establishes a direct connection between the potential $V_{ext}(\mathbf{r})$ and the ground state particle density $n_0(\mathbf{r})$, showing that $V_{ext}(\mathbf{r})$ is, except for a constant, an unique functional of $n_0(\mathbf{r})$ [28].
This means that the Hamiltonian is, apart from a constant shift in energy, fully determined by the electron density. Therefore, the electron density determines the many-body wavefuctions and consequently all properties of the investigated system in the ground state [8, 28].
The second theorem defines an energy functional $E[n]$ which is valid for any external potential $V_{ext}(\mathbf{r})$ and any number of particles N. For a given $V_{ext}(\mathbf{r})$, the ground state energy is the global minimum of this functional. The electron density which minimizes the functional is the ground state density $n_0(\mathbf{r})$ [8, 28].
In the following, a schematic description of the Hohenberg-Kohn theorem as presented in Ref. [8] is shown. The standard approach, denoted by single black arrows, derives all states of a system $\Psi_i(\{\mathbf{r}\})$ by solving the Schrödinger equation including $V_{ext}(\mathbf{r})$. From this the ground state $\Psi_0(\{\mathbf{r}\})$ can be derived, and consequently the ground state density $n_0(\mathbf{r})$. The Hohenberg-Kohn theorem on the other hand, denoted by the red double arrow, directly links the ground state density to the external potential.

$$\begin{array}{ccc} V_{ext}(\mathbf{r}) & \Longleftarrow & n_0(\mathbf{r}) \\ \downarrow & & \uparrow \\ \Psi_i(\{\mathbf{r}\}) & \rightarrow & \Psi_0(\{\mathbf{r}\}) \end{array}$$

The main challenge in applying the Hohenberg-Kohn theorem is to determine the functional which, by minimisation, would give the particle density and total energy of the many-body interacting system [8, 28].

2.3.2 The Kohn-Sham approach

In Ref. [29] Kohn and Sham propose an approach to treat complicated interacting many-body problems by using an auxiliary system with the same electron density as the described system to simplify the problem. A density functional $E[n]$ consisting of a kinetic energy part of a system of non-interacting electrons and an exchange-correlation part to describe the many-body interaction effects is applied [29]. The system of independent particles can be solved exactly, while the complicated interaction properties are considered in the exchange-correlation functional of the density [8]. A general assump-

tion necessary for this description is that the ground state density of any considered interacting system can be represented by the ground state density of a non-interacting system. The accuracy of the found ground state electron density and energy of course depends on the quality of the approximations in the exchange-correlation functionals [8, 29].
Eq. 7 gives the ground state energy functional E_{KS} with the independent particle kinetic energy T_S, the external potential of the atomic nuclei $V_{ext}(\mathbf{r})$, the interaction between the nuclei E_{II}, the coulomb interaction energy $E_{Hartree}$ and the exchange-correlation energy E_{XC} [8].

$$E_{KS} = T_S[n] + \int d\mathbf{r} V_{ext}(\mathbf{r}) n(\mathbf{r}) + E_{Hartree}[n] + E_{II} + E_{XC} \tag{7}$$

Mostly local or semi-local approximations are used for E_{XC}, which allows to lower the computational effort [8].
The Kohn-Sham eigenvalues have no direct physical equivalent, but can be used to approximate physical quantities [8]. This is due to the fact that the Kohn-Sham theory is constructed to derive the ground state energy and ground state electron density of an interacting system, modelled by a non-interacting system. Therefore, the eigenvalues do not correspond to the physical energies of adding or removing electrons to/from a system [8]. According to Levy et al. [30] there is only one exception to this rule: In a finite system, the ionisation energy corresponds to the highest eigenvalue multiplied by -1.

2.3.3 Exchange-correlation functionals

The Kohn-Sham equations separate the kinetic energy of independent particles and the long range Hartree terms from the exchange-correlation functional, which suggests the use of approximations for E_{XC} that are local or semi-local functionals of the density [8, 31].

The local density approximation (LDA)
One of the most basic approximations for the exchange-correlation functional is the local density approximation. It is based on the idea of using the exchange-correlation energy of a homogeneous electron gas (which is often used to describe the electronic situation in metallic solids) to approximate E_{XC} [29]. This approximation is possible if the electron density is considered to be slowly varying. The local spin density approximation (LSDA) is an enhancement and generalisation of LDA, where a spin-polarisation function is included [8]. As L(S)DA is designed to describe on uniform electron gas, it is not very well suited for molecular systems, where it strongly underestimates the exchange energy and overestimates the electron correlation, leading to on

overestimation of bond strengths [8]. It should be mentioned here that the correlation term is often much more difficult to describe mathematically, but it also contributes less to the total energy in most cases [8].

The generalized gradient approximation (*GGA*)
Generalized gradient approximations build on the local density approximation. While LDA only uses the local electron density, *GGA* goes beyond that and applies a functional of the local density as well as the gradient of the density at every point in space [8]. Several different approaches exist, which do not all necessarily lead to an improved behaviour compared to LDA, as they often fail for real materials, where the gradients can become very large [8]. It is not really possible to nominate the "best" functional, as there is no ideal functional in general but only for the application in specific cases. Partly empirical *GGA* functionals exist, where one or more parameters are derived from experimental results [8]. This is in contrast to totally nonempirical functionals such as *PBE* [1], which was employed in this work.

2.3.4 Solution of the Kohn-Sham equations

The Kohn-Sham equations are a set of independent-particle equations to derive the electron density $n(\mathbf{r})$, using the effective potential $V_{eff}(\mathbf{r})$, which consists of the external potential $V_{ext}(\mathbf{r})$, the Coulomb potential $V_{Hartree}[n]$ and the exchange correlation potential $V_{XC}[n]$ [8, 29]. An iterative solution of the KS equations is necessary, as the effective potential depends on the electron density, which is also the desired solution. Therefore, an initial guess for the electron density $n_i(\mathbf{r})$ is taken, from which the effective potential is calculated and the KS equation is solved. After that, a new electron density $n_{i+1}(\mathbf{r})$ is calculated and compared to the original electron density. This process is repeated until the electron densities of successive steps match and self-consistency is reached [8]. Convergence depends on the choice of the new effective potential, which can for example be achieved by so-called "linear mixing", which means the derivation of a new input density from a linear combination of the input and output densities of the former step (or from more than one previous steps) [8]. This procedure is schematically shown in the following.

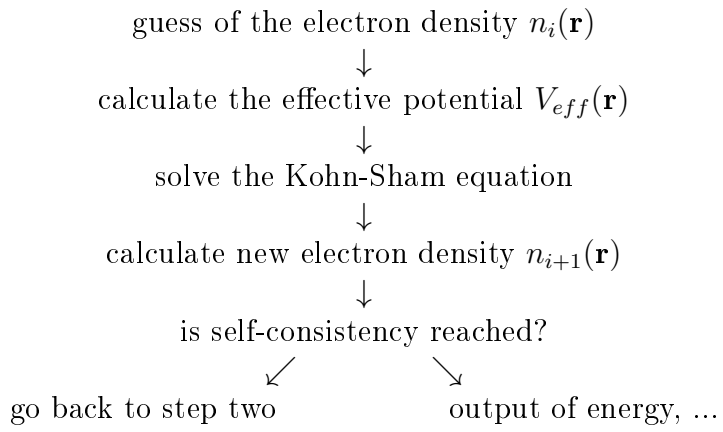

2.3.5 Describing the electronic structure

To describe the electronic states of a material, different basic approaches can be applied, with the most common ones in DFT being plane-wave methods and atomic orbital methods such as the linear combination of atomic orbitals LCAO [8, 31]. Plane wave methods are especially well-suited for periodic crystal systems, while (localized) atomic orbital methods are widely applied in chemistry, as they are for example very useful to describe molecular systems [31].
The electronic structure of an investigated system can be approximated by a suitable set of basis functions. Many different types of basis sets exist, and DFT procedures use either all-electron methods or pseudopotential methods [8]. The goal of pseudopotentials is to limit the computational effort by reducing the effective number of electrons which have to be described explicitly [8]. This is done by combining the strong Coulomb potential of the nucleus and the strongly bonded core electrons into one effective potential, which the weakly bonded valence electrons feel [8]. Pseudopotentials have a characteristic core radius, as they are limited to a certain physical extend and the atomic potential inside the core region is described by an analytic function [31]. Outside this region the electronic structure is described by pseudo-wavefunctions, which are required to match a reference all-electron wavefunctions beyond the core radius [31]. The core radius determines the "hardness" of a potential. A small core radius, denoted as hard pseudopotential, requires more basis functions and leads to more accurate results and good transferability to other systems, while soft pseudopotentials with a large core radius speed up the calculations [31].
The projected augmented wave formalism (PAW) [32], which was used in this work builds on orthogonalized plane wave methods and combines the principal idea of pseudopotentials with the use of full all-electron wavefunctions to be able to perform very accurate density functional theory calcualtions of total energies and forces. It offers the possibility to keep the applied basis sets relatively small [8].

2.3.6 Shortcomings of (semi-) local DFT methods

Although DFT proves to be a very powerful tool for a large variety of applications, some situations persist to be challenging. It is, therefore, necessary to chose the applied method with caution and keep an eye on possible error sources which could adulterate the outcome when performing DFT simulations.
First, although DFT outperforms most other quantum mechanical techniques, the systems size still is a strong limiting factor in many cases [33].
When DFT simulations lead to qualitatively or quantitatively wrong results, this is mostly due to the approximations made to obtain the exchange-correlation potential [8]. The main problems include the notorious failure to predict the fundamental gap of materials [34, 35], the spurious effects of single electron self-interaction errors [35, 36] and the neglect of long-range van der Waals interactions [31, 34].
In this work, mostly the missing of long-range interactions and the single electron self-interaction errors were of interest. Their consequences and possible workarounds will be presented in the following sections.

2.3.7 Hybrid functionals

A problem in (semi-) local DFT with generalized gradient functionals as *PBE* is the appearance of a single electron self-interaction error (SIE), that denotes the Coulomb interaction of on electron with itself [37, 38]. The consequence of this error is an exaggerated delocalization of electron density, which hardly affects total energies but causes an spurious increase in the Coulomb repulsion, pushing the affected orbitals up in energy [37, 38]. This leads to a decrease of the binding energy, with the effect being stronger the more localized an orbitals is [36, 39]. Unoccupied orbitals may also be affected, when an orbital is divided from an occupied one by hybridisation or spin-splitting [39]. If the occupied orbital is shifted due to the SIE, for symmetry reasons the corresponding unoccupied one must be shifted in the opposite direction. The SIE may, therefore, cause pure *PBE* calculations to place the LUMO too low and the HOMO too high in energy, resulting in a reduction of the gap. It might also cause *PBE* to predict orbital ordering incorrectly [38, 40].
The single electron self-interaction error is not present in Hartree-Fock, due to the exact Fock-exchange, which compensates the self interaction term of one electron [2, 41].
To improve the results of DFT simulations, so called hybrid functionals can be employed [36]. Hybrid functionals join the exchange-correlation functionals from standard DFT (e.g. *PBE*) with an exact exchange part as used in Hartree-Fock methods [8]. Depending on the hybrid functional, different portions of HF exact exchange can be applied. This mixture leads to a reduction of the SIE, which can be minimized for a specific system by tuning the fraction of exact exchange [38].
Organic molecules such as metal phthalocyanines have been investigated with *GGA* and

hybrid functionals (*PBEh* [42], *B3LYP* [43], *HSE* [2]) to compare the outcomes of the different methods [36, 39, 40]. The resulting spectra showed several differences, mainly a compression of the filled states in the *PBE* spectra relative to the hybrid functional spectra, resulting in a higher density of states in these areas, a smaller HOMO-LUMO gap for *PBE* and also different orbital orderings in some cases. The incorrect orbital ordering can also lead to misidentification of the HOMO and LUMO levels. In case of metal phthalcyanine, hybrid functional calculations yielded much better results compared to experimental outcomes than *GGA* simulations [36, 39, 40].
Hybrid functionals are computationally more costly, especially if periodic boundary conditions are applied, caused by the long-range Fock exchange [44]. Therefore, the use of screened hybrid functionals like the Heyd-Scuseria-Ernzerhof (*HSE*) functional [2] is desirable for the simulation of large systems. *HSE* is based on the generalized gradient functional *PBE* [1] and its corresponding hybrid functional *PBEh* [42]. In contrast to *PBEh*, *HSE* does not only mix in a fraction of exact exchange from Hartree-Fock but also applies a range separation parameter ω. A screened Coulomb potential is applied to describe the exchange interaction, where the screening of the long-range part of exact exchange is modelled using an error function [2]. This means the exchange interaction is subdivided into a long-range and a short-range part and exact exchange is only applied in the short range region.
As the SIE is stronger for localized orbitals, neglecting the long-range part still yields good results and the computing time is reduced. This is, for example, shown in Ref. [36], where *HSE* calculations yield similar results than those obtained by hybrids without range separation.
The hybrid functional *HSE06* was applied in this work. It uses a fraction $\alpha = 0.25$ of exact exchange and a range separation parameter $\omega = 0.2$ Å^{-1} is applied. It proved to be successful especially for the description of metallic systems [2].
GGA functionals, especially with included vdW corrections, have yielded good results for the simulation of the geometry of organic molecules on metal surfaces [4, 45]. When it comes to the description of electronic properties going beyond the work function modification, hybrid functionals like *HSE* can, however, often provide much better insight and give much more accurate results compared to experimental data [36, 44].

2.4 Treating vdW interactions in DFT

The basic principle of DFT, as described in the previous chapter, enables an exact description of the electronic structure of matter. However, to put it to practical use, approximations are necessary, especially regarding the exchange-correlation potential, which describes the interaction part of the electrons in a many-body problem. These XC approximations keep computational cost low and still lead to surprisingly good results of DFT simulations in many cases [8, 9]. But there are some situations where the standard DFT methods like *GGA* fail, for example, when describing noble gas crystals or the interaction of graphene sheets [9]. This is due to the semi-local character of the

applied approximations, where weak interaction over bigger distances are neglected as the approximations rely on the overlap of electron densities to describe interactions [9]. Semi-local approximations work well for strongly bonded systems, and the neglect of long-range interactions saves an enormous amount of computation time.
The most interesting long-range interactions are dispersion or van der Waals forces. Dispersion forces are non-local attractive electron-electron interactions due to the response of electrons in one region to charge fluctuations of electrons in a distant region [15]. Therefore, it is a dipole-induced dipole interaction which causes a decay of the interaction energy with the atomic separation r of $\frac{1}{r^6}$ (see Sec. 2.1).
In contrast to Hartree-Fock methods, which cannot describe dispersion interactions as they arise from electron correlation, DFT would in principle be able to include electron dispersion. But due to i) their nonlocal character and ii) their instantaneous nature, they are not captured by the (semi-) local functionals which also not account for instantaneous density fluctuations.

Van der Waals corrections for metal-organic interfaces
Metal-organic interfaces as investigated in this work experience bonding due to several effects, including van der Waals interactions. They are well-suited as an example to show the failure of standard DFT functionals for "weakly" bonded systems. It should be mentioned here that vdW interactions are not only crucial in these mainly physisorbed systems, but can also play an important role in "strongly" bond chemisorbed systems. It has been demonstrated for several situations (e. g. PTCDA on Au [46], PTCDA on Ag(111) [4, 47], CuPc on PTCDA on Ag(111) [10]) that for this kind of systems, there is often no bonding behaviour to be observed if vdW forces are neglected. For this work, the case of CuPc on Au(111) and Ag(111) was investigated in detail and will be discussed in Sec. 5. Fig. 1 shows the binding energy curve of CuPc on Au(111), where a CuPc molecule with a fixed geometry is placed at different distances (average carbon atoms distance to top metal layer) to the substrate and the binding energy (Eq. 23) is calculated. The standard functional *PBE* is compared with the vdW-corrected $PBE{+}vdW^{surf}$, which will be discussed later in more detail. The red curve shows the binding energies calculated with the *PBE* functional, while the green curve is calculated using $PBE{+}vdW^{surf}$. While there is no minimum for *PBE* and, therefore, no bonding behaviour, the $PBE{+}vdW^{surf}$ curve exhibits a distinct minimum. It would, therefore, not be possible to perform a geometry optimisation of such a system without a vdW correction, as the molecule simply does not adsorb on the substrate.
In addition to standard vdW corrections it has been shown that the inclusion of screening (as done in $PBE{+}vdW^{surf}$) can be an additional improvement when looking at metal-organic interfaces [4, 48].
Aside from the examples where standard functionals totally fail to predict the geometry, there are many other intermediate cases, where dispersion forces are not solely responsible for bonding, but still have a large influence on the bonding process and, therefore, cause the DFT results to predict too large bonding distances [9].

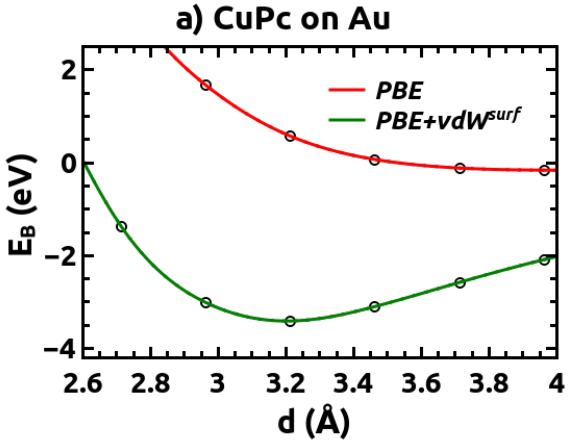

Figure 1: Binding energy E_B of CuPc adsorbed on Au(111) as a function of the height d between the average position of the molecule carbon atoms and the average position of the relaxed topmost metal layer, calculated with the *PBE* functional with and without the vdW correction vdW^{surf}. Soft PAW potentials were used. This graph is taken from [14].

It is one of the most important challenged in present-day DFT to include vdW forces in standard simulations. Ref. [9] gives an overview of different present DFT-correction methods, sorted by the the amount of approximation made in every method. Klimes et al. [9] suggest that this gives latter (more sophisticated) methods not necessarily a higher accuracy in every case, but a lower probability to fail.

Simple empirical C_6 corrections: *DFT-D*

The first requirement to a dispersion correction scheme is to provide a reasonable $\frac{1}{r^6}$ asymptotic behaviour for separated particles in the gas-phase. As the dispersion forces are solely attractive, this can be simply done by adding an extra energy term (E_{vdW}) to the total system energy (E_{sys}).

$$E_{sys} = E_{DFT} + E_{vdW} \tag{8}$$

The dispersion interaction itself is calculated from the dispersion coefficients C_6 and the distance of the particles r. A and B in Eg. 9 denote the atomic pairs interacting with each other.

$$E_{vdW} = \sum_{A,B} \frac{C_6^{AB}}{r_{AB}^6} \tag{9}$$

This form of dispersion correction is called "pairwise additive", as for every pair of atoms A, B a portion of vdW energy is added to the system energy [9]. So-called *DFT-D* methods, which represent the simplest pairwise additive correction methods use empirically determined, constant coefficients, which are independent of the spacial

direction [9, 49]. This makes these methods simple and the associated computational cost is low, as the correction happens outside the DFT self-consistent field routine. The simplicity of the routine, of course, limits the accuracy of the correction, because only the leading C_6/r^6 terms are considered and faster decaying terms are ignored [9]. An additional challenge is, of course, to obtain the C_6 coefficients. They are mostly derived from experimental data [49, 50], which limits treatable systems to experimentally investigated element combinations. Also the fact that the coefficients are kept constant is a strongly limiting factor, as changes of the environment and changing chemical properties are ignored [9].
Grimme [51] proposed a method, which offers a very effective way to derive the C_6 coefficients, using a coupling of static polarizabilities and ionization potentials of isolated atoms. Therefore, data for (nearly) all elements are available and the *DFT-D2* scheme is one of the most widely used vdW corrections [9], although it still suffers from some shortcomings, like the arbitrary choice of coefficients for some problematic elements like alkali and alkali earth atoms [9].
A problem from which all simple C_6 methods suffer is the divergence at small separations that has to be removed [9]. This is done in *DFT-D2* by applying a damping function, which decreases the dispersion energy to zero at low distances [51].

C_6 corrections with "environment-dependence"
Ref. [9] defines a second level for methods which still use pairwise corrections to determine an additive contribution to the energy, but with one main enhancement: The approximation made in the former approach, where the C_6 coefficients are constant, is a large source of impreciseness, as the actual coefficients differ strongly for different hybridization or oxidation states of a material. It is, therefore, useful to make the coefficients "environment-dependent".
The basic idea of the methods at this level is that the dispersion coefficient C_6 of an atom depends on its effective volume, which, of course, depends on the environmental conditions [9]. If the effective volume is lowered, the polarizability of the atoms goes down.
Examples for these methods are the *DFT-D3* method by Grimme [52], the Tkatchenko-Scheffler *vdW-TS* [3] approach and the Becke-Johnson model [53].
Grimme et al. propose an environment-dependence by considering the number of neighbouring atoms, which then decrease the C_6 coefficient as the atom is considered to occupy less space the more neighbours it has [52]. The coefficients for different atomic pairings in different hybridization states are precalculated and chosen depending on the actual situation during a simulation. *DFT-D3* is widely used and very accurate for various situations [9].
The Becke-Johnson method calculates the dispersion coefficients from the exchange-correlation hole dipole [53]. The XC hole is a region of electron depletion around an electron, which creates an asymmetric electron density and gives rise to a dipole moment which induces dipoles in surrounding atoms. The Becke-Johnson method uses an approximate exchange-hole and the polarizability of atoms to calculated the C_6 coef-

ficients. The drawback of this relatively accurate method is the higher computational effort compared to other methods on this level [9, 54].
The Tkatchenko-Scheffler method uses reference atomic polarizabilities and coefficients and the effective volume is derived using the Hirshfeld partitioning scheme [3]. *vdW-TS* will be discussed in more detail later.

Beyond C_6 corrections: long-range density functionals
Until now, all methods needed an additional input of C_6 coefficients and/or polarizabilities to determine the dispersion energy. The next step are so-called non-local correlation functionals, which use the electron density to derive the dispersion interactions and add it to local or semi-local functionals [9].
These methods still apply a pairwise correction as the non-local correlation energy is calculated in a pairwise form from electron density. An example is the so called van der Waals density functional *vdW-DF* by Dion et al. [55], where an overall dispersion calculation for all ranges is performed directly within the DFT functional.

Beyond pairwise additives
All former methods calculated dispersion energies as a pairwise additive. Therefore the interaction of two atoms is considered separately from all other parts of the system, and screening effects due to other atoms and collective effects are ignored [9]. This approximation works fine in the gas phase, but it is problematic when describing adsorption and condensed matter systems.
Several different approaches exist to include dispersion beyond pairwise corrections [9]. Examples are three-body interactions [56], many-body dispersion (*MBD*) interactions by coupled dipoles [57] or the use of orbitals to calculate the dispersion correction energy using the adiabatic-connection-fluctuation-dissipation theorem (*ACFDT*) [58]. The most promising method is based on *ACFDT* and is called the random phase approximation (*RPA*) [59], which is, for example, capable of describing complicated features of graphite, which all pairwise correction methods fail to reproduce [60].
Finally, so-called range separated methods use a combination of DFT for short range an and post-HF methods for long range interactions [61].
The computational cost is, of course, an important factor when choosing the vdW correction scheme. The methods using C_6 corrections do not increase the computational effort of DFT calculations significantly, as only simple calculations outside the self consistent field routine are needed. While *DFT-DF* already increases the computing time notably (by about 50 %), the methods described in this step increase the effort by orders of magnitude [9].

2.4.1 Tkatchenko-Scheffler vdW correction: *vdW-TS*

One of the pairwise-correction methods presented in the previous section is the Tkatchenko-Scheffler dispersion correction [3]. It will be discussed in more detail as it is the basis for vdW^{surf} [4], which was used in this work.
The additive energy term for an atom pair A and B is calculated in terms of the interatomic distance R_{AB}, the vdW radii R_A^0 and R_B^0 and the vdW coefficients C_6. To get rid of the singularity at small distances, a damping function f_{damp} is applied [49, 50].

$$E_{vdW} = -\frac{1}{2}\sum_{A,B} f_{damp}(R_{AB}, R_A^0, R_B^0) C_{6AB} R_{AB}^{-6} \tag{10}$$

vdW-TS derives the C_6 coefficients, which depend on the environment of a particle, from the electron density, a reference electron density and reference coefficients for free atoms. It does, therefore, not rely on any empirical parameter input [3].
Charge polarization effects are included by calculating the relative polarizability of an atom in a molecule from the electron density.
The C_{6AB} coefficient to describe the vdW interaction between two atoms (or molecules) A and B is derived from the homonuclear C_6 parameters and frequency-dependent polarizabilities $\alpha(i\omega)$ of A and B. The effective coefficients of an atom in a solid or molecule requires the definition of an effective volume, which links the volume of the atom to the interaction-free gas-phase volume. Due to the direct relation between polarizability an volume [62] it is possible to employ the Hirshfeld partitioning scheme of the electron density [63] to subdivide the electron density of the whole system (molecule) between the contained atoms. In Ref. [3] the ratio between effective and relative volume is shown in terms of effective and relative polarizability α and the proportionality constant κ between volume and polarizability [64, 65].

$$\frac{V_A^{eff}}{V_A^{free}} = \frac{\kappa_A^{eff}}{\kappa_A^{free}} \frac{\alpha_A^{eff}}{\alpha_A^{free}} \tag{11}$$

In terms of the Hirshfeld partitioning the ratio of effective and relative volume is

$$\frac{V_A^{eff}}{V_A^{free}} = \left(\frac{\int r^3 w_A(\mathbf{r}) n(\mathbf{r}) d^3\mathbf{r}}{\int r^3 n_A^{free}(\mathbf{r}) d^3\mathbf{r}}\right) \tag{12}$$

with the Hirshfeld atomic partitioning weight for an atom A next to another atom B

$$w_A(\mathbf{r}) = \frac{n_A^{free}(\mathbf{r})}{\sum_B n_B^{free}}. \tag{13}$$

The effective C_6^{eff} coefficients can now be obtained by scaling the reference C_6^{free}, which is the vdW coefficient for the free atom. The scaling is done using the effective and

relative frequency η, which depends on the polarizability, the proportionality constant κ and the volume V [3].

$$C_{6AA}^{eff} = \frac{\eta_A^{eff}}{\eta_A^{free}} (\frac{\kappa_A^{free}}{\kappa_A^{eff}})^2 (\frac{V_A^{eff}}{V_A^{free}})^2 C_{6AA}^{free} \tag{14}$$

Going to larger systems (as molecules) can be done easily, as the C_6 coefficients are additive and can be derived as the sum over all interatomic contributions in a molecule [66].
When the method is applied to correct DFT calculations, a damping function, depending on the interatomic distance and the vdW radii of both atoms needs to be applied. This is necessary for the treatment of short distances, where the C_6 correction diverges (see Eq. 10). A Fermi-type damping function [49] is applied [3].
vdW-TS performs very well for various systems, and does not deviate strongly for different exchange-correlation functionals [3].

2.4.2 Modelling hybrid inorganic-organic systems: vdW^{surf}

To accurately describe the adsorption geometry of metal-organic interface systems it can be an enhancement to include Coulomb screening effects of the bulk in the vdW correction method. As mentioned in the introduction of this work, no further computational investigations of the electronic properties can be done reliably without first knowing the geometry.
Ruiz et al. present the *PBE+*vdW^{surf} method [4] to extend the standard pairwise correction schemes especially for the description of adsorption processes on solid surfaces. It combines the above discussed *vdW-TS* method with the Lifshitz-Zaremba-Kohn theory, which models Coulomb screening of the bulk.
vdW^{surf} is a correction method of the total energy for DFT simulations. It works non-self consistently, as it modifies the DFT energy outside the self-consistent field (SCF) loop, and does not directly act on the charge density [4].
It calculates the vdW correction energy by a sum of $C_6^{ab} R_{ab}^{-6}$ terms, with R_{ab}^{-6} giving the interatomic distances, similar to *vdW-TS* (see Eq. 10). Additionally, the many-body collective response ("screening") of the substrate electrons is included [20]. The determination of the C_6 coefficients, therefore, includes i) interface polarization effects due to their dependency on the electron density (which is already included in *vdW-TS*) and ii) screening effects. This means vdW^{surf} actually goes beyond a pairwise description as defined in the former chapter (see Sec. 2.4).
The LZK theory describes the vdW interaction of an atom which is brought close to a crystalline solid surface [20, 67]. The attractive polarization force between the parts of the system is described using an atom-solid potential dependent on the position of a reference plane Z_0. The vdW interaction energy between the atom a and the solid B is calculated as [20, 67]

$$E_{vdW} = \frac{-C_3^{aB}}{Z^3}. \tag{15}$$

Z marks the distance to the image plane at Z_0, and C_3^{ab} are the vdW coefficients [20]. The expression for C_3^{aB} depends on the polarizability of the atom α and the dielectric function of the solid ϵ_B [20, 67].

$$C_3^{aB} = \frac{\hbar}{4\pi} \int_0^\infty d\omega(i\omega)\alpha(i\omega)\frac{\epsilon_B(i\omega) - 1}{\epsilon_B(i\omega) + 1} \tag{16}$$

To derive the C_6 coefficients of an atom a and the solid B one can sum the pair potentials of atom a with every single atom b in the solid B [68]. This leads to the following relation between the C_3^{aB} and the $C_{6,LZK}^{ab}$ coefficients with the image plane position $Z_0 = \frac{d}{2}$ and the interlayer distance d [4, 68], where n_s gives the density of atoms in the bulk:

$$C_3^{aB} = n_s(\frac{\pi}{6})C_{6,LZK}^{ab} \tag{17}$$

The screened $C_{6,LZK}^{ab}$ coefficients can now be derived by combining Eq. 16 and Eq. 17. Compared to *vdW-TS*, the inclusion of screening leads to a reduction of the C_6 coefficients.
Similar to *vdW-TS*, the heteronuclear $C_{6,LZK}^{ab}$ coefficients can be fragmented into C_6^{aa} and $C_{6,LZK}^{bb}$ coefficients [4].

$$C_{6,LZK}^{ab} = \frac{2C_6^{aa}C_{6,LZK}^{bb}}{\frac{\alpha_{LZK}^b}{\alpha_0^a}C_6^{aa} + \frac{\alpha_0^a}{\alpha_{LZK}^b}C_{6,LZK}^{bb}} \tag{18}$$

The C_6^{aa} describe atoms in molecules and are, therefore, equal to the coefficients derived for *vdW-TS*, while the $C_{6,LZK}^{bb}$ are coefficients for bulk atoms and differ from the free atom values.
α_0^a and α_{LZK}^b are the polarizabilities of free and bulk atoms, respectively. Eq. 18 can be used to derive the unknown bulk parameters $C_{6,LZK}^{bb}$ and α_{LZK}^b, as the molecular atom parameters C_6^{aa} and α_0^a are already known from *vdW-TS* considerations [3].
Ruiz et al. [4] solved Eq. 18 for a given solid B and two different adsorbing atoms. The pool of atoms which were used included H, C, Ne, Ar and Kr. It turned out that the bulk parameters are virtually independent of the nature of the adsorbed atom, which makes them an intrinsic property of the bulk [4].
After the calculation of $C_{6,LZK}$ and α_{LZK} coefficients, the effective "environment dependent" values for C and α as well as for the vdW radii R and R_{LZK} can be computed. They are derived using the effective volume v_{eff}^i for an atomic species i.

$$v_{eff}^i = (\frac{\int r^3 w_i(\mathbf{r})n(\mathbf{r})d^3\mathbf{r}}{\int r^3 n_i^{ref}(\mathbf{r})d^3\mathbf{r}}) \tag{19}$$

The Hirshfeld partitioning scheme is used to subdivide the electron densities and relate it to specific atoms. The effective volume then consists of reference and free electron densities $n(\mathbf{r})$ and the Hirshfeld atomic partitioning weight of the species $w_i(\mathbf{r})$ (Eq. 13). The reference electron density is the spherical electron density of an atom in the bulk or the free atom electron density, depending on whether it is a solid or a free atoms [4]. The effective and reference $C_{6,LZK}$, α_{LZK} and R_{LZK} are linked through the effective volume.

$$C_{6,eff}^{ii} = (v_{eff}^{i})^2 C_{6,ref}^{ii} \tag{20}$$

Ruiz et al. tested vdW^{surf} for the experimentally and computationally well-investigated system of PTCDA on Ag(111) [13, 23, 46, 47, 69]. They showed that vdW^{surf} outperforms most other common dispersion-correction methods for DFT when it comes to the description of metal-organic interfaces [4]. For PTCDA on Ag(111), vdW^{surf} predicts the adsorption height of all atomic species in the molecule with an error below 0.1 Å and also gives a good estimation of the binding energy. It can be applied for insulating, semiconducting or metallic substrates [4]. Moreover, due to the fact that it is a simple C_6 correction outside the self-consistent field routine it does not significantly prolong the simulation time.

3 Methodology

To perform density functional theory calculations, the Vienna Ab Initio Simulation Package VASP [11] was applied. VASP is a code to perform quantum-mechanical ab initio simulations. In this work the versions VASP 5.2.11, VASP 5.3 and VASP 5.3.3 with several add-ons were applied. The different versions of the code will be discussed in the following chapters. To optimize system geometries either the build-in geometry optimisation function of VASP was used, or a combination of VASP and GADGET [12], which is a tool specialized for this task. When using both, the energy is calculated by VASP while GADGET updates the geometry.
The applied exchange-correlation functionals where *PBE* [1], a *GGA* functional presented by Perdew, Burke and Enzerhof and the *HSE06* functional [2], which was used for the electronic structure calculations in the last chapter (see Sec. 6). The electronic structure was described using the projected augmented wave method PAW [32].
It was already mentioned earlier that the inclusion of van der Waals interactions is crucial for a meaningful description of metal-organic interfaces as investigated in this work. The method vdW^{surf} was designed to add a vdW energy correction to DFT calculations for exactly this kind of situation.
Two different implementations of vdW^{surf} were applied, firstly the vdW correction by Wissam A. Saidi [5] added to VASP 5.3 and secondly the implemented *vdW-TS* correction of VASP 5.3.3, also with an additional modification by Tomáš Bučko. These methods will be reviewed in more detail in Sec. 4.2.
To make convergence in DFT calculations easier, or, in some cases, even possible, artificial broadening of the otherwise sharp electronic states is necessary. This so-called smearing was performed using a Methfessel-Paxton occupation scheme of first order [70], with a default smearing width of 0.2 Å. The smearing will be discussed in more detail in the following section.
The calculations were carried out on the i-cluster and the d-cluster at TU Graz.
The graphical representations of 3D systems, including charge density and LDOS plots were created using the XCrysden tool [71].

3.1 The unit cell, periodic boundary conditions and dipole correction

The unit cell for every investigated metal-organic interface consisted of 3-4 metal layers, with the lowest layer positioned at $z = 0$ and a molecule above the metal slab. Three layers proved to be sufficient, as no significant charge rearrangements could be noted at the lowest metal layer in any case. To obtain a more general picture of the adsorption process, the topmost metal layer was allowed to relax during the geometry optimisations.
Several molecule geometries were adopted from previous projects: The chlorgallium-

phthalocyanine (GaClPc) molecule was originally constructed by Oliver T. Hofmann, the copper phthalocyanine (CuPc) and zinc phthalocyanine (ZnPc) molecule geometries were adopted from previous work by Yu Li Huang, and the pentacentequinone (P2O) and pentacenetetrone (P4O) molecule geometries were kindly provided by Georg Heimel.
For the input most molecules (also the adopted geometries) were pre-optimised using GADGET in a large unit cell (at least 20 Å of vacuum in every direction) to speed up the convergence of the metal-organic interface simulation.
All simulations were performed using periodic boundary conditions and the repeated slab approach to simulate a substrate with a metallic character. To keep the layers of metal-organic slabs from interacting, a vacuum region of at least 20 Å was applied in every case. Additionally an artificial dipole sheet was introduced in the vacuum region to cancel the dipole of the interface.
All metal slabs were fcc(111) surfaces, with lattice constants according to the applied functional and vdW correction (see Sec. 4 for more details). Therefore, two different lattice constants for every metal (Au, Ag and Cu) were applied, namely a *PBE* and a *PBE* + vdW^{surf} lattice constant. The necessity of different lattice parameters and their application will be clarified in Sec. 4.
In this work, surface unit cells are given in matrix representation. The surface unit cell vectors **A** and **B** are given in multiples m_{ij} of the primitive surface unit cell vectors **a** and **b** of the fcc(111) surface (see Eq. 21).

$$\begin{bmatrix} \boldsymbol{A} \\ \boldsymbol{B} \end{bmatrix} = \begin{bmatrix} m_{11} & m_{12} \\ m_{21} & m_{22} \end{bmatrix} \begin{bmatrix} \boldsymbol{a} \\ \boldsymbol{b} \end{bmatrix} \tag{21}$$

3.2 The Vienna Ab Initio Simulation Package VASP

VASP is a parallel plane wave simulation package for quantum-mechanical simulations, which treats Kohn-Sham functionals in a self-consistent loop to determine the ground-state energy of a system [72]. It applies pseudopotentials or the projected augmented wave method.
In the following, some important details on the mode of operation of VASP will be reviewed, going along with the necessary control parameters. The description of the parameters is based on the VASP manual [72].

3.2.1 VASP Input

The input which is required for every simulation includes a unit cell, the starting geometry and several parameters to determine the course of the simulation. This information is contained in the input files *POSCAR*, *INCAR*, *POTCAR* and *KPOINTS*.

The *POSCAR* file
The *POSCAR* file contains the geometry information for a VASP simulation [72]. It specifies the size of the unit cell using three spacial coordinates for the three unit cell vectors and the number of elements of every atomic species present in the system. The ordering of this list must be consistent with i) the listing of atomic coordinates below ii) the ordering of atomic potentials in the *POTCAR* file and iii) the listing of parameters which are different for different atomic species in the *INCAR* file.
The *POTCAR* file also specifies a scaling factor for the unit cell, the type of coordinates (cartesian or direct) and a list with coordinates for every atom in the system. If *Selective Dynamics* is activated, there is an additional set of three variables for every atom, defining its freedom to move in every spacial direction during a geometry optimisation.

The *KPOINTS* file
The *KPOINTS* file contains all necessary information on the k-point grid [72]. The k-points can either be entered explicitly or by using an automatic k-point mesh. One needs to specify the type of the k-point mesh, the subdivisions of the lattice vectors in every direction and the shift of the mesh in every direction. The latter option can be used to avoid k-points in the center of the unit cell in x or y direction in case of an odd number of subdivisions these directions, which could be troublesome due to symmetry reasons.
In this work the Monkhorst-Pack k-point mesh was used [73].
As many of the unit cells were of similar size and quite large, a *2x2x1* k-point grid was applied in most simulations. For all other cases the k-point grid is listed with the unit cell description.

The *POTCAR* file
In the *POTCAR* file the pseudopotentials (or PAW potentials) for the atomic species in the system are listed [72]. *POTCAR* needs to contain the same number of data sets in the same order as the header of *POSCAR*, where the atomic species are listed. The classification as an element of every fragment in a VASP calculation is determined by the potentials which are assigned in the *POTCAR* file. The header of every data set contains the maximum and minimum cutoff energies. For several atomic species, soft, normal and hard potentials are available. For the sake of saving computation time mostly soft potentials were applied in this work.
Two different sets of PAW potentials were used, "old" potentials and "new" 5.3 potentials released in 2012. Their comparability was tested and the results are reviewed in Sec. 4.2 and Sec. 5 for different metal-organic systems.
Tab. 1 lists the titles of all used PAW potentials.

Table 1: Applied PAW potentials. "Old" potentials refer to the original set of VASP PAW potentials, while "new" means the newly release set of 2012, going with VASP 5.3 and higher.

	old potentials	new potentials
H soft	-	PAW_PBE H_s 15May2010
H normal	PAW_PBE H 15Jun2001	PAW_PBE H 15Jun2001
H hard	-	PAW_PBE H_h 06Feb2004
C soft	PAW_PBE C_s 06Sep2000	PAW_PBE C_s 06Sep2000
C normal	PAW_PBE C 08Apr2002	PAW_PBE C 08Apr2002
C hard	-	PAW_PBE C_h 06Feb2004
N soft	PAW_PBE N_s 07Sep2000	PAW_PBE N_s 07Sep2000
O soft	-	PAW_PBE Cl 06Sep2000
O normal	PAW_PBE O 08Apr2002	PAW_PBE O 08Apr2002
O hard	-	PAW_PBE O_h 06Feb2004
F soft	-	PAW_PBE F_s 06Sep2000
Cl	PAW_PBE Cl 06Sep2000	PAW_PBE Cl 17Jan2003
Cu	PAW_PBE Cu 05Jan2001	PAW_PBE Cu 22Jun2005
Zn	-	PAW_PBE Zn 06Sep2000
Ga	PAW_PBE Ga 08Apr2002	PAW_PBE Ga 08Apr2002
Ag	PAW_PBE Ag 06Sep2000	PAW_PBE Ag 02Apr2005
Sn	-	PAW_PBE Sn 08Apr2002
Au	-	PAW_PBE Au 04Oct2007

The *INCAR* file

The *INCAR* file specifies the simulation parameters needed by VASP and can contain a huge number of parameters. In the following, some parameters which were of importance for this work will be explained and the values applied in the performed simulations will be listed [72].

ENCUT: This parameter gives the cutoff energy in eV which is applied to the plane wave basis set. In this work, the highest cutoff energy of the contained atoms as specified in the *POTCAR* file was used for all calculations.

EDIFF: The self consistent loop is terminated as soon as the energy change between two steps lies below a certain threshold, specified by the *EDIFF* tag. In case of systems with many different states lying close in energy it might be useful to set a lower value to reach a more distinct result. In this work *EDIFF* was set to 10^{-4} if not stated differently.

LWAVE and *LCHARG*: The files *WAVECAR* and *CHGCAR* contain the wavefunction and the charge density of a system, respectively. For geometry optimisations or

other calculations where several SCF routines are performed, it is either possible to use the wavefunctions and charge densities of the last step as a starting configuration or to create them newly in every step, which normally slows down the calculation. *LWAVE* and *LCHARG* define whether these files should be written out after every SCF loop.

ISTART and *ICHARG*: If *WAVECAR* and *CHGCAR* exist from previous calculations, they can be read in to accelerate the convergence of the simulation. *ISTART* and *ICHARG* define, whether existing *WAVECAR* and *CHGCAR* files should be used. This feature is useful for *HSE* calculations, which can be based on previous *PBE* calculations, or to do a spin-polarized simulation in two steps as described below.

NELM and *NELMIN*: These tags give the maximum and minimum number of self consistent steps, respectively. For slowly converging spin-polarized simulations the *NELM* parameter should be set to a higher value than the default 60 steps, as this is often not enough.

ISMEAR and *SIGMA*:
As mentioned in the beginning of this chapter, artificial broadening of the states is necessary for convergence reasons. *ISMEAR* an *SIGMA* determine the smearing type and the smearing width, respectively.
The chosen smearing type in this work was Methfesse-Paxton of first order (*ISMEAR = 1*) [70]. The default value for *SIMGA*, the smearing width in eV was *SIGMA = 0.2*. This parameter should be chosen with caution, as a large smearing width speeds up the simulation, but might deteriorate the outcome, as it can lead to artificial overlapping of states, which could lead to a wrong total energy. Small values of *SIGMA* can be problematic for large systems or complicated simulations as *HSE*, as more k-points are demanded for larger values of the smearing width.
If for some reasons a calculation needs to be performed with a low smearing width, it is also possible to broaden the states after the simulation to make the DOS easier to read. If no artefacts due to a too large smearing widths appear, the results of calculations should not depend on whether the broadening was done before or after the calculation.

Spin-polarized simulations
Spin-polarized simulations are often problematic, as the additional degree of freedom can slow down the simulation significantly. Also it has to be checked carefully if the magnetic moments are distributed in a physically meaningful way after every calculation.
If no spin-convergence can be reached, it might be useful to perform the simulation in two steps: First a non-spin polarized calculation is performed and then repeated in a spin-polarized manner, using the *CHGCAR* and *WAVECAR* files obtained in the first step as a starting point. This method should be used with caution as the result is somehow prejudiced due to the first, spin-unpolarized calculation.
It might also be helpful to use the *MAGMOM* tag to predefine the distribution of the

magnetic moment or the *NUPDOWN* tag to fix the total magnetic moment of the system.

ISPIN: If the calculation should be performed spin-polarized, which is necessary when the (isolated) organic adsorbate contains an odd number of electrons, *ISPIN* is set to 2, while *ISPIN = 1* leads to a non-spin polarized calculation.

MAGMOM: This tag allows to set an initial magnetic moment in multiples of μ_B on every atom. As spin-polarized simulations can be very cumbersome, the predefinition of unpaired spins can be very useful, and the VASP-manual [72] recommends to set about 1.3 times the expected actual magnetic moment onto the concerned atoms.

NUPDOWN: If the difference in the number of of spin up and spin down electrons for a system is known, the *NUPDOWN* tag can be used to fix it during the whole simulation, which can speed up convergence. Experience with *HSE* calculations on CuPc on Ag(111) showed that, if the spin density at the beginning of the simulation does not agree with *NUPDOWN*, convergence can be decelerated.

IDIPOL: The dipole correction of the unit cell can be activated or deactivated with this tag. It might me useful for cumbersome (spin-polarized) simulations, (e. g. spin-polarized *HSE*) to do a first calculation without dipole correction and read in wavefunctions and the charge density for a second run, this time switching on the dipole correction.

***HSE* simulations**:
For *HSE* simulations, convergence is especially problematic, as a slower convergence, which could, for example, double the calculation time or an erroneous simulation which has to be repeated, might lead to a delay of several weeks. Therefore, the simulation parameters should be chosen with much caution and the course of the simulation has to be monitored frequently. The first few steps of an *HSE* simulation are performed non-self-consistently to find a starting configuration for the wavefunctions and the charge density [72]. The elaborated tests on CuPc and ZnPc on Au(111) and Ag(111) (see Sec. 6) showed that, if a reasonable set of input files and parameters enables a good first guess, the simulation will converge significantly faster. Especially spin-polarized simulations demand a good starting configuration to not become prohibitively time-consuming.
In the course of testing *HSE* simulations, several different approaches which allow to speed up convergence were investigated:

- pre-defining the distribution of the magnetic moment: using the *MAGMOM* tag or reading in the *CHGCAR* file from a previous calculation.
- fixing the difference between spin up and spin down electrons with *NUPDOWN*,

but only if the system allows it

- performing the *HSE* simulation in two dipole-correction steps: first without a dipole correction, then repeat it with the obtained *WAVECAR* and *CHGCAR* with dipole correction.
- performing the *HSE* simulation in two steps with different functionals: simulating the system with *PBE* and reading in the resulting *WAVECAR* and *CHGCAR* files for the actual *HSE* calculations, but caution is on order as the *PBE* starting configuration might influence the *HSE* simulation.
- constructing a *CHGCAR* file from previous *HSE* or *PBE* simulations of the system parts (e. g., for metal-organic interfaces the metal and the organic layer separately), if one has reasons to suspect that the outcome of a *PBE* simulation of the whole systems is not a good starting point for *HSE* (e. g., because of strongly differing orbital ordering); VASP also offers the possibility to use the *CHGCAR* file to construct a *WAVECAR* file [72].

HFSCREEN: To select *HSE06*, the range separation parameter has to be set to *HFSCREEN=0.2*.

TIME: This parameter is very important for *HSE* simulations. It controls the step size of the trial steps and is, therefore, crucial for the convergence. If the step size is chosen too large, it can lead to instabilities, while a too small step size causes slow convergence. The default value is *TIME = 0.4*, which works fine especially for metals [72], but in this work *TIME = 0.2* was chosen, as this value turned out to be more reliable for metal-organic systems as investigated here (see Sec. 6).

NPAR: The *NPAR* parameter determines the parallelisation behaviour of the VASP simulation. *HSE* simulations demand *NPAR* to be set to the total number of cores [72].

3.2.2 VASP Output

The most important output files and quantities printed out by VASP during every simulation will be discussed briefly [72].
The main output files are the *.out* and the *OUTCAR* file. For single-point calculations as well as for geometry optimisations, the convergence has to be checked as the results of a non-converged simulation are rather meaningless. At the end of every SCF loop, *VASP* writes out the total energy and the line *"writing wavefunctions"* in the *.out* file, which indicates the end of a simulation. It should be checked then if the convergence criteria were really met or if the maximal number of steps was reached. If the latter is the case, the calculation should be repeated (or continued) with a higher number of

steps *NELM*.
For spin-polarised calculations, also the magnetisation *"mag"* is written out at the end of the *.out* file. It can be monitored over the course of a GADGET geometry optimisation in every **.vaspout* file, to see if it really converged properly. The distribution of the magnetic moment on atoms in the investigated system is written out at the end of the *OUTCAR* file. One needs to look at the section *"magnetization (x)"*, where the magnetisation of every ion is given, appearing in the same order as in the *POSCAR* file. Several tests on the CuPc molecule showed, for example, about 0.6 μ_B on the centring Cu atom and 0.1 μ_B per surrounding N atom. When the magnetic moment instead turns out to be equally distributed over the whole molecule the simulation appears to be flawed.
If demanded, VASP also writes out the wavefunctions and the charge density in the *WAVECAR* and *CHGCAR* files, respectively. This is done after every completed SCF loop.

3.2.3 Geometry optimisation using VASP and GADGET

The VASP code is suited to do geometry optimisation, but the optimisations of the investigated systems were mostly performed with the GADGET ([12]) tool, which works "in collaboration" with VASP. While the forces and energies are computed by VASP, the geometry step, which means the updating of the spacial coordinates of every atom, is done by GADGET. It offers several different optimisation algorithms, including an enhanced version of the direct inversion of the iterative subspace (DIIS) method [74, 75], and is capable of optimising in internal coordinates, which were the options applied in this work. This results in a faster and more accurate geometry optimisation compared to VASP [12] especially regarding the tilting behaviour (e.g. "falling over" of upright standing molecules), which is very hard to recover in cartesian coordinate optimisations. The geometry optimisation of GaClPc using VASP serves as an example for that, as will be discussed in Sec. 5. While GADGET finds tilted configurations in all cases, the molecule remains upright when optimised with VASP, which is the energetically unfavourable configuration.

Application of VASP for geometry optimisation
To perform geometry optimisations with VASP three important tags need to be set [72]:

IBRION: With the ionic relaxation tag *IBRION*, the motion of ions in a system is determined. For geometry optimisations with VASP, relaxation into local minima by *IBRION = 2*, which applies conjugate gradient algorithm and *IBRION = 3*, which applies a damped molecular dynamics algorithm were used in this work [72]. According

to Ref. [72] these algorithms are more suited for starting configurations further away from the local minimum than the RMM-DIIS algorithm (*IBRION = 1*) [76, 77].

POTIM: The *POTIM* parameter is a scaling constant for the forces in case of minimization algorithms, where an internal scaling of the forces is done before the minimization process starts [72]. It should be set in a manner to avoid divergence of the total energy, which happens in case of a too high value [72]. *POTIM* should also not be too low because this leads to slow convergence. *POTIM = 0.1* proved to be a reasonable value for the systems described in this work.

SMASS: This tag defines a damping factor in case of molecular dynamics optimisations (*IBRION = 3*), where the ionic degrees of freedom are described using a damped second order equation of motion [72]. *SMASS = 0.45* proved to be a reasonable value for the systems described in this work.

A good selection of *POTIM* and *SMASS* for damped molecular dynamics optimisations will lead to faster convergence [72]. The convergence can be checked by looking at the forces during the calculation. The best suited values depend strongly on the system and the approach recommended in Ref. [72] is to set *SMASS* to a fixed value, find the highest possible value for *POTIM* and subsequently decrease *SMASS*. For the damped molecular dynamics optimisations presented here, this approach was adopted. To confirm the convergence of the geometry optimisation, *VASP* writes out *"reached required accuracy - stopping structural energy minimisation"* at the end of the **.out* file.

Application of GADGET

The GADGET input file *INPDAT* can contain several parameters to determine the course of the simulation. The most important relaxation parameters are *GCRITER*, *SCRITER* and *ECRITER*, which give the convergence parameters for gradient, geometry and energy, respectively. In order to avoid getting stuck in local minima, GADGET can take large geometry steps, but then automatically removes the *WAVECAR* file to avoid convergence problems in the SCF-cycle of VASP.
GADGET writes out a *report* file to summarize the simulation output. An important value is the identified number of degrees of freedom, which describes, whether the algorithm was able to connect all fragments of the system by internal coordinates. The number is written out marked as *"Deg._ of_ freedom"* for every GADGET optimisation step. If the identified number does not correspond to the actually set number of degrees of freedom, no meaningful optimisation can be performed. To reach the correct number of degrees of freedom, the parameters *FRAGCOORD*, which gives the type of long-range coordinates and *ASCALE* and *BSCALE*, determining the scaling for standard and long-range coordinates, respectively, have to be modified. These scaling parameters determine the construction of the internal coordinate positions for every atom. Two atoms with an overlap of their covalent radii scaled using *ASCALE* are

considered as being bonded. To connect non-bonding fragments via internal coordinates, the covalent radii are scaled using *ASCALE*BSCALE* [12].
As finding appropriate settings is often problematic, several tests using different sets of parameters were performed for the flat-lying organic systems of this work. A standard setting with *FRAGCOORD = 2* (inverse power long-range coordinates, which are an improvement to standard internal coordinates and were proposed by Baker and Pulay in Ref. [78]), *ASCALE = 1.3* and *BSCALE = 2.1* was obtained by extensively testing the GaClPc on Cu(111) system with different parameters. These settings proved to be successful for all systems investigated in this work. Another parameter which may help with finding the correct number of degrees of freedom is *ATRADII*, which is used to modifies the covalent radii of the contained elements.
GADGET also contains an atomic substrate detection activated by the *SUBST* parameter. It specifies the number of next neighbours of on atom to define it as part of the substrate. If an atom is detected as part of the substrate, its spacial coordinates are updated different and the optimisation is less time consuming. By default, *SUBST* is set to 100, which switches off the substrate detection. *SUBST* $\approx$ *6* proved to be a reasonable choice. The number of identified substrate atoms has to be checked carefully in the *report* file, as an incorrect (too high) number will cause treating of molecular atoms as substrate and therefore prevent full geometry optimisation. In this work, several systems were optimised with and without substrate detection, but as it turned out to be problematic getting degrees of freedom as well as number of substrate atoms correct, only results obtained without substrate detection are presented in the following.
When monitoring GADGET geometry optimisations, the convergence of i) the VASP SCF steps (in the **.vaspout* files) and ii) the convergence of GADGET itself have to be checked. When the required accuracy is reached, GADGET writes out *"CONVERGENCE REACHED"* at the end of the *report* file.

4 Setting up the unit cell and testing vdW^{surf} implementations

4.1 Generation of the unit cell

4.1.1 Optimising the substrate lattice constants

The geometry optimisations of molecule-substrate systems done in this work leave full freedom of movement to all atoms of the molecule as well as to the first substrate layer. The latter allows studying surface relaxation due to molecular adsorption. Therefore, it is necessary to first optimise the lattice constant using the applied simulation method to avoid spurious relaxations inside the substrate during optimisation and to find the appropriate size of the supercell. This means that different unit cells are needed for *PBE* simulations and for vdW-corrected simulations (in case the vdW correction also applies to the substrate atoms). Why this is necessary will be explained in more detail in Sec. 4.2.2.
In the following, the optimisation of Cu with *PBE* will be described, the values for Au and Ag as well as for *PBE+vdW*^{surf} were obtained using similar procedures.

Lattice constant optimisation of Cu for *PBE*
The principle for the lattice constant optimisation is based on [79] and [80].
Two different geometries were used, the primitive fcc unit cell (1 atom), the "conventional" fcc unit cell (4 atoms) and a 1x$\sqrt{3}$x$\sqrt{6}$ unit cell (6 atoms). Different lattice constants in the area of the experimental values were probed, varying the value between 2.5500 and 2.6100 Å in steps of 0.0025 Å. The unit cells sizes were scaled according to these lattice constants and for every value a VASP simulation using V5.3 and soft PAW potentials was performed (repeated later with V5.3.3 and "new" PAW potentials for comparison). The generated parable of total energies as a function of the lattice constant was fitted with a quadratic function to find the minimum.
In case of small unit cells and too small k-point densities numerical noise effects cause deviations of the energy curve from a perfect parabolic shape. Therefore, the "conventional" unit cell was tested with different k-point densities (6, 12 and 24 k-points in every direction). For the primitive unit cell a 6x6x6 k-point grid and for the 1x$\sqrt{3}$x$\sqrt{6}$ cell a 15x8x6 grid were used.
The primitive unit cell and the conventional unit cell with small k-point numbers did not lead to satisfactory results, as the resulting energy curves exhibited more than one minimum for the reasons explained above. To improve the outcome, the k-point densities were increased. The primitive unit cell demanded too large k-point densities to simulate the system with reasonable computational effort. But both the "conventional" cell with 24 k-points in all directions and the 1x$\sqrt{3}$x$\sqrt{6}$ cell showed strictly parabolic energy curves and the lattice constant at the energy minimum could be determined

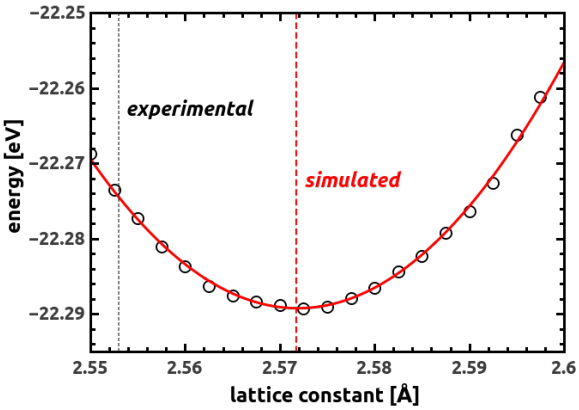

Figure 2: Lattice constant optimisation of Cu, using a 1x$\sqrt{3}$x$\sqrt{6}$ and a 15x8x6 k-point grid. Experimental lattice constant from Ref. [81].

Table 2: Lattice constants of Au, Ag and Cu, comparing calculated (*PBE* and *PBE+vdW*^{surf}) and measured values from Ref. [81]

	literature [Å]	*PBE* [Å]	*PBE+vdW*^{surf} [Å]
Au	4.08	4.175	4.141
Ag	4.09	4.154	4.031
Cu	3.61	3.637	3.583

easily, agreeing up to the third decimal point.
The energy curve of the 1x$\sqrt{3}$x$\sqrt{6}$ cell is shown in Fig. 2 and the obtained lattice constants for Cu, Au and Ag, calculated with *PBE* and *PBE+vdW*^{surf}, are summarized in Tab. 2, which also shows experimental values from [81] for comparison.

4.1.2 Generation of the unit cells

To benchmark the vdW correction method it was necessary to test several different metal-organic systems. This led to the necessity to create several different unit cells and, therefore, metallic substrates. The metal slabs differed in element (Au, Ag and Cu), lattice constants, size and form. Different lattice constants are needed for different elements and also for different simulation methods (*PBE* and *PBE+vdW*^{surf}), as explained above.
When generating new unit cells, especially the shape proved to be tricky, as rather complicated adsorption supercells appeared in case of some systems (e.g., for the pentacene derivatives on Cu(111), see Fig. 5).
To avoid cumbersome manual assembly of the unit cells for every system, the construction of the metal slab and the cell was automated using a GNU octave [82] script,

called *fcc111*.
fcc111 builds the VASP input file *POSCAR*, which defines the unit cell geometry and the positions of every atom contained in the simulated system for a fcc(111) surface unit cell. The substrate metal layers are positioned at the bottom of the unit cell. The following input parameters are required:

- lattice constant
- form and size of the unit cell
- number of substrate layers
- dynamics of the substrate layers (which layers shall be allowed to relax during the simulation)
- starting layer (a fcc(111) surface unit cell is composed of repeating units of three substrate layers, so three different layers can be chosen for the topmost metal layer)

A POSCAR file containing the substrate atom coordinates is build. The molecule coordinates can then be added manually.
Two different versions of the *fcc111* code were implemented: The first implementation is capable of building unit cells which are multiples of the following cells:

- 1x$\sqrt{3}$
- 1x1
- $\sqrt{3}$x$\sqrt{3}$

To create a unit cell, one has to choose between these basic cells and manually insert the units of repetition in every direction. Alternatively it is also possible to choose the basic cell and give the size of the desired cell in total Angstrom values.
For more complicated cells a different version exists, which does not need an exact input of the unit cell geometry. The desired geometry has to be known approximately and put in a 3x3 matrix (giving the lattice vectors). This can be done either in multiples of the lattice constant (see Eq. 21) or absolute Angstrom values. The program calculates the closest possible substrate unit cell. This is done by creating the lattice positions for a large area and finding the grid points (and according lattice vectors) closest to the input lattice vectors. Afterwards the full unit cell is constructed.

4.2 Used versions of VASP implementations of vdW^{surf}

During the first part of this work, VASP 5.2.11 and VASP 5.3 (which do not account for vdW interactions by default) with vdW corrections added by Wissam A. Saidi [5] were applied. In VASP 5.3.3, which was released during the realization of this work, a vdW correction is implemented by default. Therefore, it was one of the goals to compile and test the new VASP version and to check the agreement of results between the different vdW corrections, looking at optimised geometries, total energies and binding energies. Additionally, Tomáš Bučko (Department of Physical and Theoretical Chemistry, Comenius University, Bratislava, Slovakia) provided a version of VASP 5.3.3 which includes the possibility of selectively switching off the vdW correction for specific atomic species, which was not possible in former versions and is a big advancement. Without this feature the interaction of substrate atoms with each other is spuriously treated like a molecule-substrate interaction. Calculations which were performed with this version of VASP 5.3.3 and switched-off vdW corrections between the atoms of the metal slabs will be denoted as *sVDW* calculations in the following.
To apply *vdW-TS* [3] an extended version of VASP 5.2.11 was used, referred to as *V5.2.11(TS)* in the following. *vdW^{surf}* applications on the other hand were done using an extended version of VASP 5.3, referred to as *V5.3*. Both include a similar vdW correction, the only difference are the vdW coefficients. VASP 5.3.3 (*V5.3.3*) was applied with both *vdW-TS* and *vdW^{surf}*, which is possible because the vdW coefficients can be manually inserted for every calculation.
In the following the versions *V5.3* and *V5.3.3* are going to be reviewed briefly.

4.2.1 VASP 5.3 with a vdW extension by Wissam A. Saidi: *V5.3*

To calculate vdW interactions according to *vdW-TS*, it is necessary to define the coefficients C_6, R and α for every atomic species present in the investigated system [3]. Additionally, reference electronic densities of the atoms are needed for the Hirshfeld partitioning which are here given in pre-calculated files [5]. The reference electron densities are all-electron densities, while the interacting electron densities (to calculate the effective volume) contain only valence electrons.
The coefficients are defined in the file *vdwts_mod.F*. To use the vdW extension, the *INCAR* file needs two extra lines:

- *LVDWTS = .TRUE.* which activates *vdW-TS*
- *aeden_dir = ...* which gives the path to the files containing the reference electron densities

The calculated vdW energy is written out as *"Estimated vdwTS energy (eV):"* in the *OUTCAR* file.
To use vdW^{surf} instead of *vdW-TS* two changes are necessary [4, 3]. First, the vdW coefficients for the substrate atoms need to be changed in the file *vdwts_mod.F*. If an atomic species is present in the bulk as well as in the molecule, it needs to be defined twice, with its bulk and free-atom coefficients, also in the list of atomic species in the *POSCAR* and *POTCAR* files. Every change of coefficients for a specific element, as well as adding new sets of coefficients requires a recompilation of VASP, which is rather cumbersome.
The effective coefficients determined by the program can be read out from the **.out* file after the calculation.
vdW^{surf} also requires different reference electron densities for bulk atoms [4]. But according to several tests done by Wissam A. Saidi and the author of this work, the use of free or bulk electron densities does not cause a significant difference, so free electron reference densities were used for all atomic species in case of *vdW-TS* and vdW^{surf} calculations.
Several systems where tested using the code as described above and yielded excellent agreement between simulation and experimental outcomes for bonding distance and geometry. Some examples are CuPc and ZnPc on Au(111) and Ag(111) [14], CuPc on PTCDA on Ag(111) [10] and P2O and P4O on Au(111), Ag(111) and Cu(111) (see following chapters).

4.2.2 VASP 5.3.3 with implemented *vdW-TS*: *V5.3.3*

VASP 5.3.3 includes an implementation of *vdW-TS* [83]. To use vdW^{surf} instead, the vdW coefficients need to be overwritten. As mentioned above, it would in principle be necessary to use bulk reference electron densities for vdW^{surf} calculations, but as the caused difference seems to be negligible all used densities are free-electron densities also in this case. The reference electron densities are calculated "on the fly" whenever needed and both reference and interacting electron densities are calculated including core electrons.
While *V5.3* applies the vdW^{surf} approach to all atoms of the system, *V5.3.3* was extended by Tomáš Bučko to allow to selectively switching off vdW corrections between the atoms of a specific atomic species. vdW^{surf} is designed to describe interactions between molecule and substrate atoms, so it is not well suited for also describing the vdW interactions inside a metal substrate. Switching off these spurious correction between the slab atoms allows the use of the *PBE* lattice constant instead of the $PBE{+}vdW^{surf}$ value.
To activate *vdW-TS* and overwrite the coefficients, the *INCAR* file needs to contain a tag to activate the vdW correction and the new vdW coefficients, given in order of appearance of the atomic species in the *POTCAR* file:

- *IVDW = 2* which activates *vdW-TS*
- *VDW_ C6 = ...* the vdW coefficients given in $\frac{J*nm^6}{mol}$
- *VDW_ alpha = ...* the polarizability given in $Bohr^3$
- *VDW_ R0 = ...* the vdW radius given in Å

To use the extension mentioned in the beginning to selectively switch off vdW interactions between the atoms of one atomic species, additionally the line

- *LVDW_ SAMETYPE = F T ...*

needs to be added. One character for every atomic species present in the *POTCAR* file is needed, *F* to switch off the interactions or *T* for activating the interaction. The feature to modify the coefficients directly in the *INCAR* file also allows to easily switch off all vdW interactions for an atomic species. This can be simply done by setting the coefficients to zero.
The default values for the coefficients can be found in the file *vdwforcefield.F*, subroutine *vdw_ forces_ TS*. To use the bulk coefficients, as given in the original paper [4] one needs to be careful with the units, as C_6 is given in $Hartree * Bohr^6$ and R is given in $Bohr$ there. A table of C_6, R and α as needed for the *INCAR* file can be found in the appendix of this work.
The calculated vdW energy can be read out form the line *"Estimated vdW energy (eV):"* in the *OUTCAR* file, together with the effective coefficients as determined by the program.

4.2.3 Comparison of "old" and "new" PAW potentials

V5.3.3 requires the use of a new set of *POTCAR* files released in 2012. Up to VASP 5.2 the "old" PAW potentials were in use, while "new" PAW potentials are recommended since VASP 5.3. Several tests using "old" and "new" *POTCAR* files on similar systems showed different total energies, but no significant difference in binding energies. For two of these systems, ZnPc on Au(111) and CuPc an Ag(111) the results of these comparisons using *V5.3* are shown in Tab. 3. The total system energies E_{tot} and the vdW energies E_{vdW} were calculated using "old" and "new" potentials. Also work function modification $\Delta\phi$ and the convergence *conv*, which gives the number of steps the simulation needed to achieve SCF-convergence, are compared. From the comparison of the CuPc on Au(111) and ZnPc on Ag(111) systems it becomes apparent that the total energies are different and convergence is a little slower with "new" potentials. A comparison of the binding energy will be presented later in this chapter for the PTCDA on Ag(111) system.

Table 3: Total energy E_{tot}, vdW energy E_{vdW}, work function modification $\Delta\phi$ and convergence *conv* (number of SCF steps) of ZnPc of Au(111) and CuPc on Ag(111), calculated using *V5.3* and comparing "old" and "new" potentials. Soft PAW potentials were used.

ZnPc on Au(111)	E_{tot} [eV]	E_{vdW}	$\Delta\rho$ [eV]	conv
"old" potentials	-731.20	-43.99	-0.59	24
"new" potentials	-726.91	-43.98	-0.59	31
CuPc on Ag(111)	E_{tot} [eV]	E_{vdW}	$\Delta\rho$ [eV]	conv
"old" potentials	-762.45	-70.72	-0.45	44
"new" potentials	-752.35	-70.78	-0.45	45

4.2.4 Comparison of *V5.3* and *V5.3.3*

The tests to compare *V5.3* and *V5.3.3* were performed in close cooperation with programmers of these codes, Wissam A. Saidi (*V5.3* [5]) and Tomáš Bučko (*V5.3.3* [83]) and the explanations for the different results obtained in some cases were found due to extensive discussions with them. Also the question whether the inclusion of core electrons in the reference electron density is useful and/or necessary, as they are (nearly) not polarizable, was treated. Tomáš Bučko modified the VASP 5.3.3 code to allow several tests to shed light on these matters, which will be discussed in more detail later. A short summary of the main differences between *V5.3* and *V5.3.3* is given in the following.

- *POTCAR* files: Calculations with *V5.3* can be done with "old" or "new" POTCAR files, while *V5.3.3* requires "new" POTCAR files.
- Electron densities for the Hirshfeld partitioning:

  V5.3: Only valence electrons are included to calculate the interacting electron density, but all electrons are included in the reference densities, which are taken from pre-calculated files.

  V5.3.3: All electron densities are included in the calculation of interacting and reference densities, which are calculated "on the fly".
- In this work, free-electron reference densities are used for *vdW-TS* as well as for vdW^{surf} calculations, although originally vdW^{surf} demands bulk electron reference densities for the substrate atoms [4].
- *sVDW*: *V5.3.3* allows to switch off the interactions between one atomic species (only in the extended version).

- replacement of coefficients:

  The coefficients are defined directly and only in the source code in *V5.3*, which leads to the necessity of recompiling the code whenever the coefficients are changed. Therefore either multiple definitions of several atomic species or different code versions for *vdW-TS* and vdW^{surf} are required.

  The coefficients for *vdW-TS* are defined in the source code of *V5.3.3*, but can be easily changed for every calculation in the *INCAR* file.

4.2.5 Comparing total energies for *V5.3* and *V5.3.3*

To compare the two different implementations of vdW corrections, several systems were calculated using both codes. The *PBE* and vdW energies were compared.
To probe the influence of different coefficients, some of the test were performed using only *vdW-TS* coefficients also for metal-organic interfaces. So there was no correction of the screening due to surface atoms for these systems. The outcomes are, therefore, not meant to correctly describe these systems, but the calculations were done for the sake of comparing the energies only.
The *PBE* and vdW energies for every system are given. The *PBE* part is the result of the SCF cycle of the DFT calculation and the vdW part is the total vdW correction energy calculated according to the *vdW-TS* or vdW^{surf} scheme.

Tests using *vdW-TS* coefficients

benzene molecule, 12 atoms in the unit cell:

	E_{PBE} [eV]	E_{vdW} [eV]
V5.3	-75.52	-0.07
V5.3.3	-75.52	-0.07

ZnPc molecule, 57 atoms in the unit cell:

	E_{PBE} [eV]	E_{vdW} [eV]
V5.3	-412.54	-1.06
V5.3.3	-412.54	-1.10

PTCDA on Ag(111), 157 atoms in the unit cell:

	E_{PBE} [eV]	E_{vdW} [eV]
V5.2.11(TS)	-819.58	-28.35
V5.3.3	-819.58	-33.51

Copper surface, 6 atoms in the unit cell:

	E_{PBE} [eV]	E_{vdW} [eV]
V5.2.11(TS)	-20.56	-1.87
V5.3.3	-20.56	-2.08

Summarizing these tests, the total vdW energies compare quite well for *vdW-TS* calculations if the systems are small and do not contain heavy elements, but they differ significantly if the systems are larger and/or contain metals.

Tests using vdW^{surf} coefficients for the substrates

Copper surface, 6 atoms in the unit cell:

	E_{PBE} [eV]	E_{vdW} [eV]
V5.3	-20.56	-3.59
V5.3.3	-20.56	-3.78

Gold surface, 6 atoms in the unit cell:

	E_{PBE} [eV]	E_{vdW} [eV]
V5.3	-18.04	-2.63
V5.3.3	-18.04	-2.63

P4O on Au(111), 116 atoms in the unit cell:

	E_{PBE} [eV]	E_{vdW} [eV]
V5.3	-504.39	-40.21
V5.3.3	-504.39	-28.26

ZnPc on Cu(111), 225 atoms in the unit cell:

	E_{PBE} [eV]	E_{vdW} [eV]
V5.3	-987.20	-107.51
V5.3.3	-987.20	-112.81

When doing calculations for metal containing systems with vdW^{surf} coefficients, the total vdW energies differ strongly in most cases. The only exception is the gold surface, where both *PBE* and vdW energies compare quite well. The reason for the good agreement in this single case is not clear.

4.2.6 Comparing binding energies for *V5.3* and *V5.3.3*: Binding energy curve of PTCDA on Ag(111)

In most simulations performed using *V5.3* the simulated and experimental adsorption heights were in good agreement. This is the case for PTCDA on Ag(111) [10], and also for other systems as CuPc and ZnPc on Au(111) and Ag(111). The results for the latter systems are shown in Tab. 4. The *V5.3* simulations of CuPc and ZnPc were performed by Yu Li Huang.

Table 4: Comparing computed average adsorption heights of the CuPc molecule on Au(111) and Ag(111) using *V5.3* and *V5.3.3* with soft PAW potentials.

CuPc	**Au(111)**		**Ag(111)**	
	$h_{V5.3}$ [Å]	$h_{V5.3.3}$ [Å]	$h_{V5.3}$ [Å]	$h_{V5.3.3}$ [Å]
Cu	3.16	3.23	2.81	3.03
C	3.22	3.26	2.98	2.99
N	3.24	3.29	2.93	3.06
H	3.18	3.20	3.00	2.92

ZnPc	**Au(111)**		**Ag(111)**	
	$h_{V5.3}$ [Å]	$h_{V5.3.3}$ [Å]	$h_{V5.3}$ [Å]	$h_{V5.3.3}$ [Å]
Cu	2.96	3.01	2.74	2.78
C	3.21	3.28	2.99	2.96
N	3.21	3.30	3.03	2.97
H	3.18	3.22	3.03	2.94

Further tests to compare the binding energy of PTCDA on Ag(111) using the different implementations showed that these values do not compare as well as the adsorption distances.
To be able to compare the newly calculated binding energy curves with the original data reported in Ref. [4], the same unit cell as used there was applied. This unit cell contained 3 layers of substrate atoms and 175 atoms in total, with a lattice constant for the Ag substrate of 4.159 Å (equal for all simulations). No geometry relaxation was performed and the PTCDA molecule was kept flat. To obtain a binding energy curve, the adsorption distance was varied between 2.36 and 4.36 Å and the binding energy

for every adsorption distance was calculated by subtracting the energies of slab and monolayer alone from the energy of the whole system (see Eq. 23).

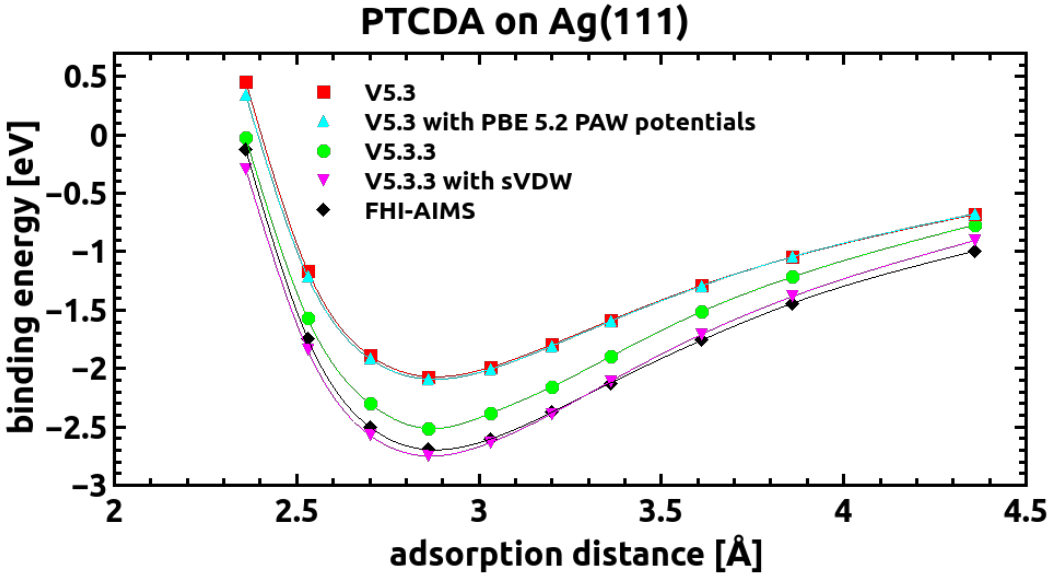

Figure 3: Binding energy curve of PTCDA on Ag(111) calculated with different implementations of vdW_{surf}. Soft PAW potentials were used.

Table 5: Binding energy of PTCDA on Ag(111) at the minimum adsorption distance (d = 2.86 Å) calculated with different implementations of vdW^{surf} and soft PAW potentials.

	E_B [eV]
V5.3, "old" and "new" PAW potentials	-2.07
V5.3.3	-2.52
sVDW	-2.70
FHI-aims	-2.75

Fig. 3 shows the binding energy curve of PTCDA on Ag(111) compared for different implementations. First, there is obviously no relevant discrepancy in the adsorption distances, as the energy curves all exhibit their minima at similar distances. The adsorption energies, on the other hand, differ significantly.
Both simulations performed using *V5.3* underestimate the binding energy by about 0.7 eV, regardless whether "old" 5.2 PAW potentials (blue triangles) or "new" 5.3 PAW potentials (red squares) are applied.
Using *V5.3.3* (green circles) improves the situation, but still does not reproduce the binding energy obtained by *FHI-aims* in Ref. [4] (black rotated squares). Finally, when applying *sVDW* and switching off the vdW correction between the substrate atoms

(magenta triangles) the results match with *FHI-aims*. This is reasonable as these spurious interactions are also not present in the calculations by Ruiz et al.
At first it might seem surprising to find a difference in binding energy due to switching off the substrate vdW correction, as its contribution to the vdW energy should cancel when subtracting the energy of the slab from the energy of the combined system. The remaining difference stems from the changed vdW parameters of the vdW^{surf} calculation due to the charge transfer between PTCDA and Ag(111). These parameters depend on the local charge density. Switching off the Ag-Ag vdW interactions changes the charge transfer between molecule and substrate, consequently the charge density is also changed, which leads to different vdW coefficients and a different binding energy curve.
In simulations including geometry optimisations, the necessity to use different unit cells for calculations without spurious substrate vdW corrections (*PBE* instead of $PBE+vdW^{surf}$) causes an additional difference in energy.
The binding energies at the minimum (d = 2.86 Å) for different implementations are shown in Tab. 5.

4.2.7 Comparing effective volumes for *V5.3* and *V5.3.3*

To understand what causes the difference in vdW energies between *V5.3* and *V5.3.3*, the effective C_6 coefficients of different systems were monitored.
The vdW^{surf} algorithm uses the Hirshfeld partitioning of the electron density to derive the effective volume, which is then used to calculate the effective C_6 coefficients (Ref. [4], Eq. 4). So the effective volume v_{eff} gives the ratio between the reference and effective vdW coefficients and can, therefore, be consulted to compare the performance of the two different vdW algorithms.

$$v_{eff} = \frac{C_{6,eff}}{C_{6,ref}} \tag{22}$$

The effective C_6 is written out in the *OUTCAR* file at the end of every calculation.
To find out which differences between the codes cause the energy discrepancy, Tomáš Bučko modified the VASP 5.3.3 code in different ways to make the outcome directly comparable to the results obtained with the code by Wissam A. Saidi.
The Hirshfeld partitioning to determine the effective volume was done in several different ways:

- using all electrons for reference and interacting densities: default VASP 5.3.3 implementation
- only valence electrons for reference and interacting densities: modifications of VASP 5.3.3 for testing reasons

- all electrons for reference and only valence electrons for interacting densities: modifications of VASP 5.3.3 for test reasons and implementation in *V5.3*

The applied test system was bulk Ag. *vdW-TS* with the primitive unit cell and vdW^{surf} coefficients with primitive and "conventional" unit cell of Ag were used, and the different versions of the Hirshfeld partitioning explained above were applied.

Bulk Ag, *vdW-TS* coefficients, $C_{6,ref} = 339 Hartree * Bohr^6$

	$C_6\ [Hartree * Bohr^6]$	v_{eff}
V5.3	275.99	0.902
V5.3.3, all electrons for int. and ref. densities	380.19	1.059
V5.3.3, valence electrons for int. and ref. densities	384.30	1.065
V5.3.3, valence electrons for int., all electrons for ref. densities	278.52	0.906

Bulk Ag, vdW^{surf} coefficients, $C_{6,ref} = 122 Hartree * Bohr^6$

primitive unit cell:

	$C_6\ [Hartree * Bohr^6]$	v_{eff}
V5.3	100.02	0.905
V5.3.3, all electrons for int. and ref. densities	136.79	1.059
V5.3.3, valence electrons for int., all electrons for ref. densities	100.95	0.910

conventional unit cell:

	$C_6\ [Hartree * Bohr^6]$	v_{eff}
V5.3	100.04	0.906
V5.3.3, all electrons for int. and ref. densities	136.82	1.059
V5.3.3, valence electrons for int., all electrons for ref. densities	100.97	0.910

V5.3 and *V5.3.3* yield very different C_6 coefficients and effective volumes, which is not surprising when recalling the different total vdW energies of earlier tests.
When comparing the modification of *V5.3.3* which uses only valence electrons for the Hirshfeld partitioning to the default version, which includes all electrons, no large differences of v_{eff} can be observed. This is easily explained by the fact that the core electrons are in principle not polarizable and, therefore, contribute only minimally to the C_6 coefficients.
When, however, the electron densities for the Hirshfeld partitioning are mixed, i. e. only valence electrons are included to calculate the interacting densities but all electrons for the reference densities, the results change significantly. The agreement of v_{eff} between *V5.3* and *V5.3.3* in the modified version with "mixed" densities is pretty good, so this mixing of electron densities is, obviously, the reason for the disagreement of total vdW energies of these two versions.

4.2.8 General remarks about *V5.3.3*

It should be mentioned that caution is in order when comparing the vdW coefficients. As mentioned above, the default *vdW-TS* values can be found in the source code, file *vdwforcefield.F*. The C_6 coefficients are given in $\frac{J*nm^6}{mol}$, if the conversion which is done right after the definition is taken into account. This conversion is done using the variable *conversion2*, which is defined there. R and α are given in *Angstrom* and $Bohr^3$, respectively. These are also the units which are demanded for the input in the *INCAR* file. The effective coefficient which are written out in the *OUTCAR* file are given in the following units: $C_6 : [Hartree * Bohr^6]$, $R : [Bohr]$ and $\alpha : [Bohr^3]$.
When applying vdW^{surf} with coefficients from Ruiz et al. [4] not only C_6, which is also given in $Hartree * Bohr^6$ there, but also R, which is given in $Bohr$ there, has to be converted.
When first using *V5.3.3* many simulations crashed after several geometry optimisation steps, producing the error *"Error: some force-field parameter for the following atom is not defined:"*. According to Tomáš Bučko this is caused by an "inaccurate" setting, e.g. *PREC=Normal*, which sets "accuracy" parameters. In general, this setting would be suitable for the systems investigated in this work, but it can cause small noise effects in the charge density and can even lead to negative values at certain grid points. For the SCF routine of the VASP calculation this causes no errors, but it leads to problems with the determination of the vdW coefficients. Tomáš Bučko provided a version of VASP 5.3.3 where this problem is resolved. The computed energies differ slightly from older versions, in the range of a few meV.

5 Adsorption of organic molecules on metal substrates

The centerpiece of this work was the simulation of several metal-organic systems and the comparison of calculated results to experimental data. Mainly planar molecules like metal phthalocyanines and pentacene derivatives were investigated. Also one non-planar system, chlorgallium phthalocyanine GaClPc was calculated. To allow the comparison of experimental and simulated adsorption heights, mainly systems for which XSW data is available were chosen.
In this section, the performed simulations will be presented and discussed. First, a geometry optimisation was carried out for every investigated system. Some systems were analysed in more depth, depending on convergence of the calculation, occurring ambiguities and comparability of the outcomes to available experimental data.
The input unit cells, obtained adsorption distances and work function modifications are presented for all investigated systems. In some cases also snapshots of the converged geometries are shown.
The applied unit cells for all systems contained only one molecule to keep the computational effort low. This was possible as for none of the simulated systems experimental evidence pointing to significantly different situations was available.
To demonstrate the geometries of the investigated systems, a top view picture of every metal-organic interface is shown. For most systems, an educated guess of the adsorption position and rotation of the molecule on the surface could be made. This was possible as experimental results or results from previous simulations on equal or similar systems were available. The molecules were positioned accordingly and, therefore, did mostly not reorient and reposition strongly during geometry optimisation. As the topmost metal layer is also allowed to relax during optimisation, the top view pictures of the end geometries become rather confusing due to the irregular positioning of the substrate atoms. Also small deformation of the molecule can cause the top views to become hard to read. For this reason, the top views of the starting geometries are displayed in all cases, an the relaxed geometries are only shown from above if necessary, e.g., because of a strong reorientation of a molecule.
Experimental information on the discussed systems was needed to i) find accurate unit cells and ii) compare and verify the simulated adsorption heights.
The simulated adsorption heights are given relative to the average position of the (hypothetical) unrelaxed topmost substrate layer (if not stated differently). This distance was chosen for the sake of comparability to XSW measurements, where adsorption heights relative to the substrate layer spacing are detected. For some systems also the distance to the actual position of the topmost metal layer, which is allowed to relax during geometry optimisation, is included.
The goal of all simulations was to reproduce the experimental findings and simulate the molecular adsorption heights within a range of 0.1 - 0.2 Å, which was considered as good agreement between experiment and simulation.
After successfully determining the adsorption geometry, further investigations concern-

ing the electronic structure can be made. In this chapter the work function modifications are listed for all treated systems, and in some cases also the density of states are given. For CuPc and ZnPc on Au(111) and Ag(111) the electronic structure was analysed in more depth, as presented in Sec. 6.

5.1 Planar molecules

5.1.1 Pentacene derivatives: Pentacenequinone (P2O) and pentacenetetrone (P4O)

The 6,13-pentacenequinone ($C_{22}H_{12}O_2$) and 5,7,12,14-pentacenetetrone ($C_{22}H_{10}O_4O$) molecules are pentacene derivatives with two and four oxygen atoms, respectively. Their structures are shown in Fig. 4. These systems were chosen as experimental information from Ref. [45] is available, on the adsorption heights as well as on the unit cell geometries. In this extensive study on the adsorption behaviour of these molecules by Heimel et al., also simulation results obtained using VASP with the *PBE* functional and a Grimme-type vdW correction [51] are presented. This enables a comparison of the $PBE{+}vdW^{surf}$ not only to experimental but also different computational data. Georg Heimel also kindly provided the unit cell geometries for all P2O and P4O systems, which were partly adopted in this work.

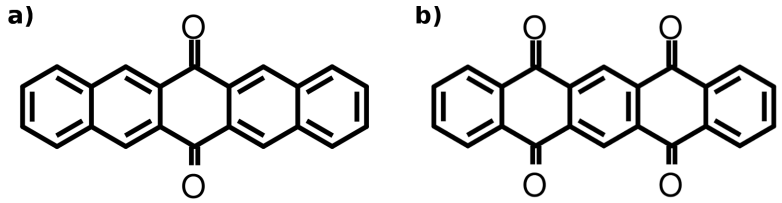

Figure 4: Structure of 6,13-pentacenequinone P2O (a) and 5,7,12,14-pentacenetetrone P4O (b).

According to the experimental study mentioned above, both molecules act as electron acceptors with P4O exhibiting the lower LUMO and therefore showing higher electron affinity [45]. P2O and P4O show varying absorption behaviours on the coinage metals Au, Ag and Cu which are, in this order, decreasingly noble. Therefore they exhibit different work functions. Due to the high work function of Au, both molecules experience weak bonding on this metal, with high adsorption distances and only minimal deformation of the molecule. They experience strong bonding on the less noble Cu, with low adsorption distances and strong deformation. Adsorption on Ag is an intermediate case. Experimental results show strong bonding of P4O due to its higher electron affinity, and weak bonding of P2O [45].

experimental data

Heimel et al. [45] studied the lateral structure of P2O and P4O on Au, Ag and Cu using low-temperature scanning tunnelling microscopy and the vertical adsorption distance using the normal-incident X-ray standing wave technique (NIXSW) at room temperature. Therefore, information on the unit cells as well as on the adsorption distances is available.

unit cells and input

The structures of all unit cells for the pentacene derivates were adopted from Ref. [45]. The actual sizes of the unit cells differ between this work and the work by Heimel et al. because of different lattice constant due to unequal vdW algorithms. They were constructed according to STM images of P2O and P4O on Au(111) and Cu(111). As P2O experimentally exhibits weak interactions on Ag(111) as well as on Au(111), the unit cell for P2O on Ag(111) was deduced from P2O on Au(111). For P4O on Ag(111) the unit cell was based the Cu situation, as P4O experimentally exhibits strong interactions on Cu(111) and Ag(111). The unit cell geometries are listed in Tab. 6, Fig. 5 shows the top views of all systems. The starting geometries of the molecules were adopted from the unit cells provided by Georg Heimel and slightly varied for the usage in this work. They were reshaped to obtain a planar geometry and were placed in a distance of about 4 Å to the top metal layer.
The k-point grids are also given in Tab. 6. The energy cutoff was set to 282.841 eV for calculations with soft, 400.000 eV for calculations with soft and normal and 700.000 eV for calculations with hard PAW potentials.

Table 6: Unit cell geometries and k-point grids for pentacene derivatives P2O and P4O on Au(111), Ag(111) and Cu(111), constructed according to STM images as presented in Ref. [45]. Unit cells for Au and Cu surfaces are based directly on these images while unit cells on Ag are deduced from similar structures.

	P2O	P4O
Au(111)	4 layers, 72 atoms $\begin{bmatrix} 6 & 0 \\ 0 & 3 \end{bmatrix}$, $2x4x1$ k-points	4 layers, 80 atoms $\begin{bmatrix} 4 & 0 \\ 2 & 5 \end{bmatrix}$, $3x3x1$ k-points
Ag(111)	4 layers, 72 atom $\begin{bmatrix} 3 & 0 \\ 0 & 6 \end{bmatrix}$, $4x2x1$ k-points	4 layers, 80 atoms $\begin{bmatrix} 3 & 1 \\ 4 & 8 \end{bmatrix}$, $5x2x1$ k-points
Cu(111)	4 layers, 96 atoms $\begin{bmatrix} 6 & 0 \\ 2 & 4 \end{bmatrix}$, $2x4x1$ k-points	4 layers, 84 atoms $\begin{bmatrix} 5 & 3 \\ -2 & 3 \end{bmatrix}$, $3x3x1$ k-points

Simulations using *V5.3*

All described pentacene derivatives were simulated with *V5.3*, using both soft and hard PAW potentials. In some cases the soft PAW potentials for oxygen led to simulation problems and were therefore replaced by normal ones.
The computed adsorption heights are listed in Tab. 7, compared to experimental values and calculations (*PBE* + Grimme-vdW) presented in Ref. [45]. Fig. 6 shows the side views of the obtained final adsorption geometries.
When looking at Fig. 6, on Ag(111) and Au(111) there is obviously stronger bonding of the oxygen atoms to the substrates compared to the rest of the molecule, as the oxygen atoms are bent down while the ends of the molecules bend up. On Au(111), the molecule stays mainly flat. All molecules were previously placed on the substrates in a way that the oxygen atoms were positioned above a top metal layer substrate atom.

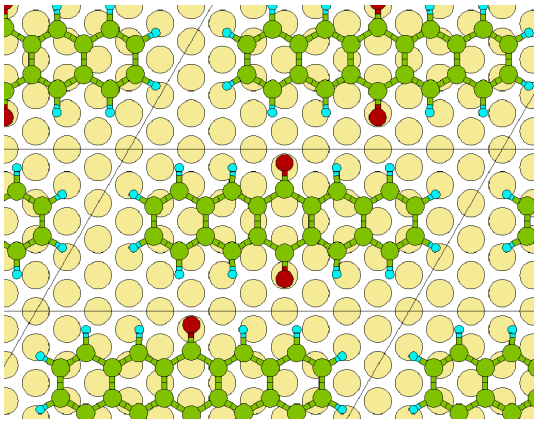

(a) P2O on Au(111)

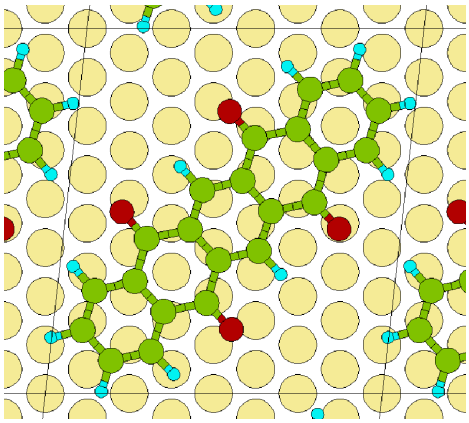

(b) P4O on Au(111)

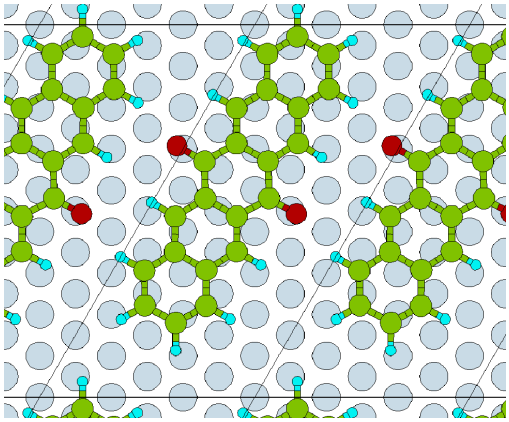

(c) P2O on Ag(111)

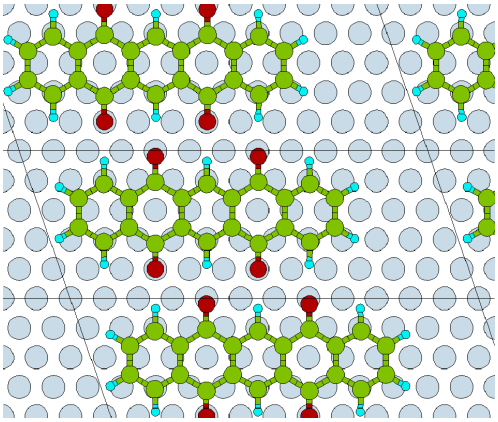

(d) P4O on Ag(111)

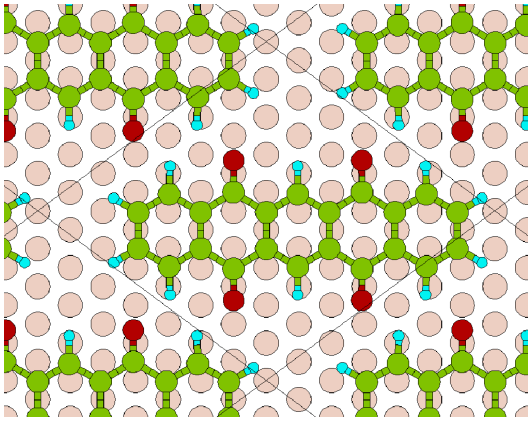

(e) P2O on Cu(111)

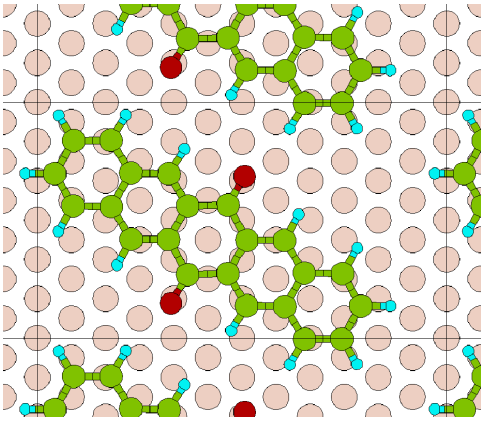

(f) P4O on Cu(111)

Figure 5: Top view of the unit cell geometries of P2O and P4O on Au(111), Ag(111) and Cu(111).

Therefore, no significant lateral repositioning of the molecules during simulation was observed.
Agreement between experiment and simulation proved to be good for both molecules on Au and Cu substrates. Weak interactions on Au(111) and strong interactions on Cu(111) were be observed, as expected from experiment and calculations by Heimel et al. [45]. The vertical distortion of the molecule due to the bending of the oxygen atoms toward the surface amounts to 0.13 Å (0.02 Å) for P2O (P4O) on Au(111) and 0.38 Å (0.20 Å) for P20 (P4O) on Cu(111), when comparing the outcomes obtained with hard PAW potentials. Consistent with experiment, P4O also shows strong bonding behaviour on Ag(111) in the simulations performed here. The molecular distortion amounts to 0.36 Å. The P2O on Ag(111) systems appears to be more complicated. Experimental data and simulations performed by Heimel et al. [45] find weak interaction, while the *VASP* simulations performed in this work predict adsorption heights that clearly indicate strong interaction. There is an intermediate distortion of the molecule amounting to 0.13 Å.
Several approaches to explain and overcome this mismatch of results were tested using *V5.3.3*.
The computed work functions and work function modifications of the pentacene derivate systems causes by molecular adsorption are listed in Tab. 8. The work function of Au (5.20 eV) is higher than the one of Cu(111) (4.79) which is still higher than Ag(111) (4.48 eV). This ordering is consistent with experimental outcomes of the (111) surfaces of noble metals [84].
The DOS for all six systems are presented in Fig. 7. For Au(111), the Fermi energy of both systems lies within the band gap. On Ag(111), the Fermi energy of P2O already lies on the edge of band gap, while for P4O on Ag(111) and for both molecules on Cu(111) it lies deep within the former unfilled states.

Table 7: Computed average adsorption heights of C (h_C) and O (h_O) atoms of pentacene derivatives P2O and P4O on Au(111), Ag(111) and Cu(111). V5.3 was used, applying different kinds of PAW potentials (soft, normal and hard). For comparison, experimental results from NIXSW measurements and calculated results using *PBE* + Grimme-vdW from Ref. [45] are listed.

P2O / Au(111)	h_C [Å]	h_O [Å]
soft(H, N) and normal(O) PAW potentials	3.18	3.26
hard PAW potentials	3.18	3.31
Ref. [45], VASP + Grimme-vdW	3.18	3.21
experiment	-	-
P2O / Ag(111)	h_C [Å]	h_O [Å]
soft PAW potentials	2.81	2.52
hard PAW potentials	2.92	2.79
Ref. [45], VASP + Grimme-vdW	3.24	3.25
experimen experiment	3.32	3.35
P2O / Cu(111)	h_C [Å]	h_O [Å]
soft PAW potentials	2.46	2.08
hard PAW potentials	2.49	2.11
Ref. [45], VASP + Grimme-vdW	2.56	2.19
experimen experiment	2.34	2.02
P4O / Au(111)	h_C [Å]	h_O [Å]
soft(H, N) and normal(O) PAW potentials	3.49	3.47
hard PAW potentials	3.33	3.35
Ref. [45], VASP + Grimme-vdW	3.24	3.25
experimen experiment	3.35	-
P4O / Ag(111)	h_C [Å]	h_O [Å]
soft(H, N) and normal(O) PAW potentials	2.77	2.38
hard PAW potentials	2.75	2.39
Ref. [45], VASP + Grimme-vdW	2.80	2.51
experimen experiment	2.69	2.43
P4O / Cu(111)	h_C [Å]	h_O [Å]
soft(H, N) and normal(O) PAW potentials	2.28	1.99
hard PAW potentials	2.24	2.04
Ref. [45], VASP + Grimme-vdW	2.49	2.19
experiment	2.25	1.98

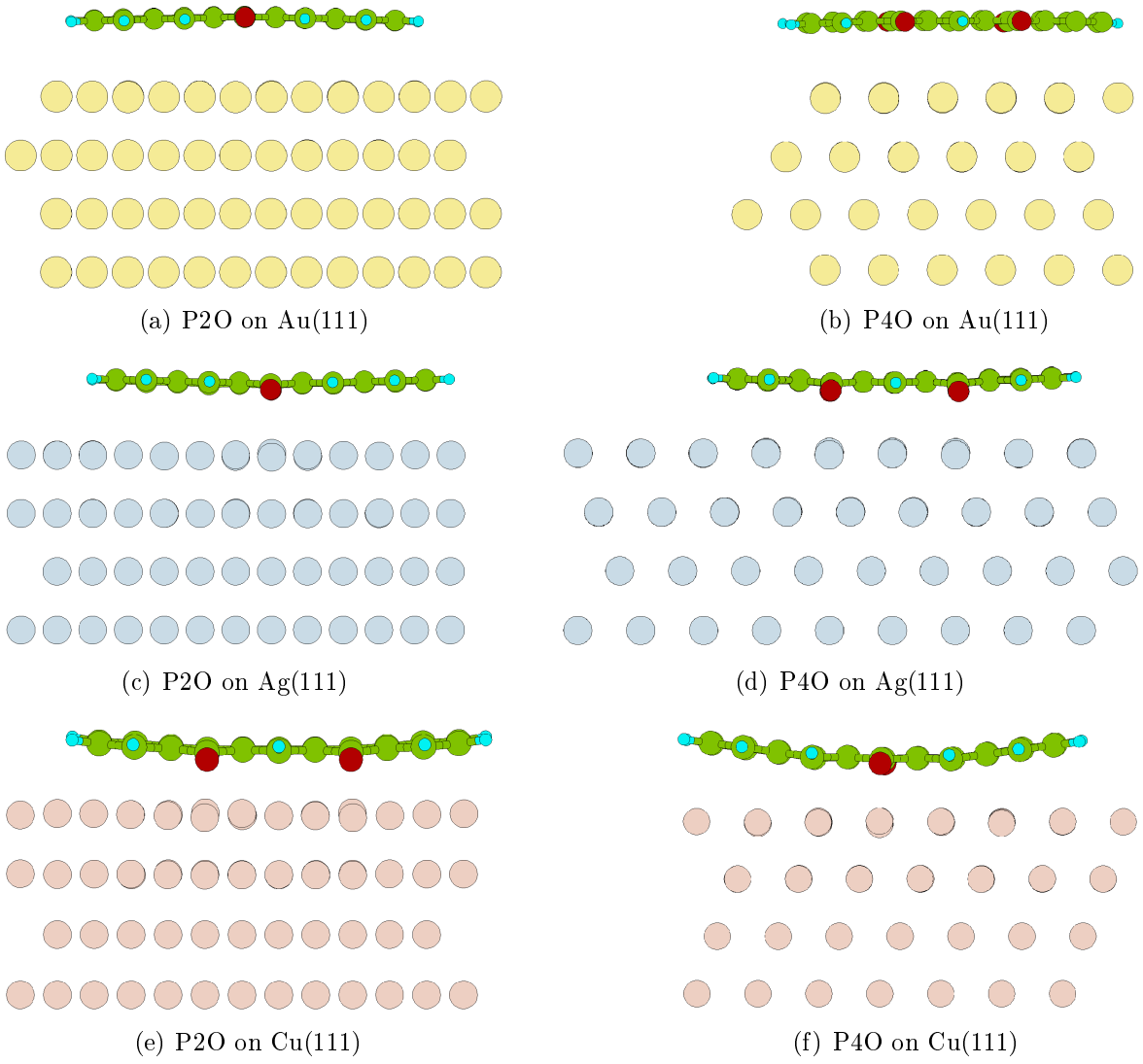

(a) P2O on Au(111)

(b) P4O on Au(111)

(c) P2O on Ag(111)

(d) P4O on Ag(111)

(e) P2O on Cu(111)

(f) P4O on Cu(111)

Figure 6: Side view of the relaxed adsorption geometries of P2O and P4O on Au(111), Ag(111) and Cu(111).

Table 8: Work functions ϕ and work function modification $\Delta\phi$ caused by the adsorption of the pentacene derivatives on a substrate, calculated with hard PAW potentials.

	ϕ [eV]	$\Delta\phi$ [eV]
P2O / Au(111)	5.20	-0.62
P2O / Ag(111)	4.48	-0.52
P2O / Cu(111)	4.79	-0.71
P4O / Au(111)	5.20	-0.33
P4O / Ag(111)	4.48	-0.17
P4O / Cu(111)	4.79	-0.58

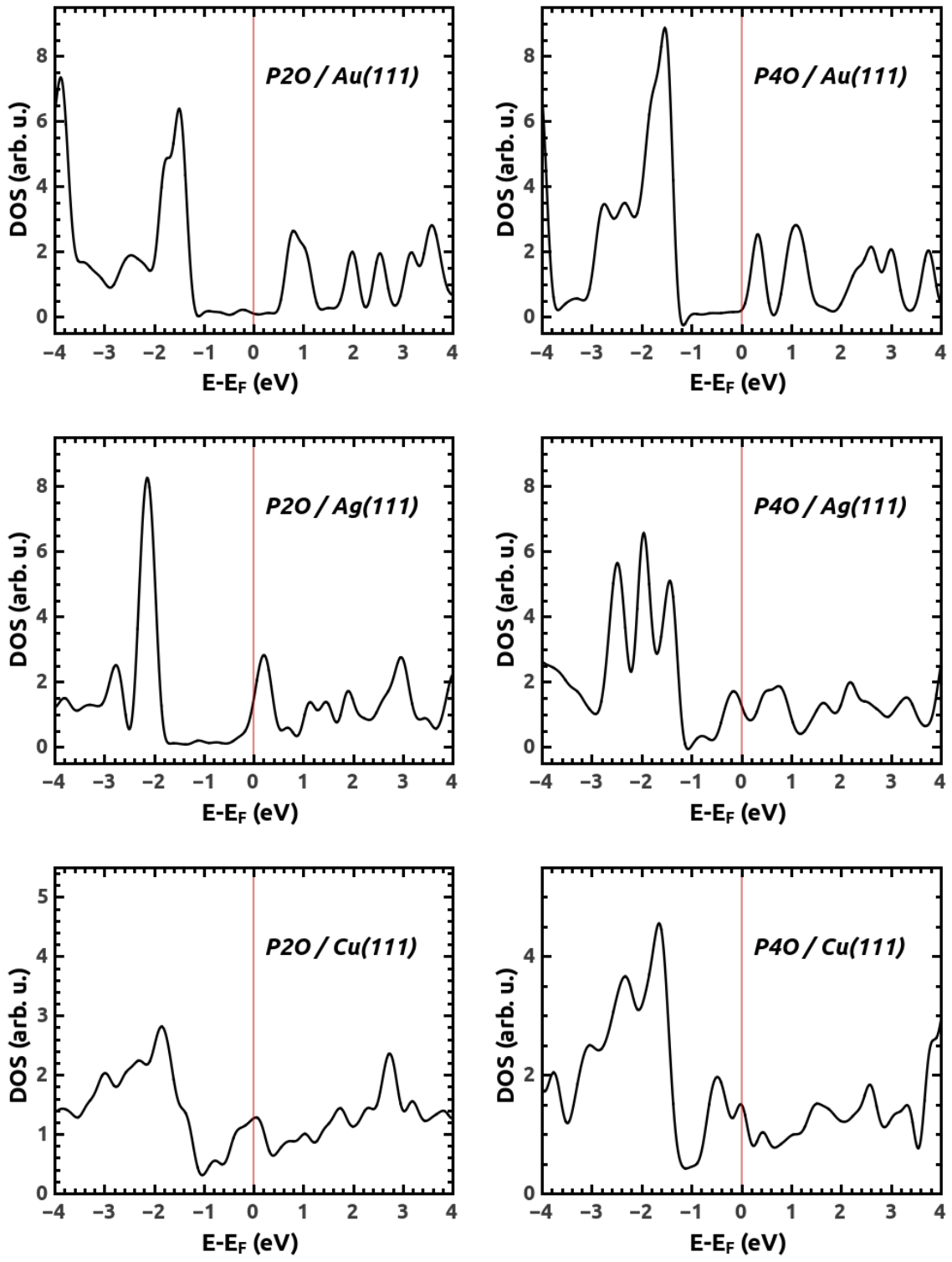

Figure 7: Density of states of the organic adsorbate P2O and P4O on Au(111), Ag(111) and Cu(111), calculated with hard PAW potentials. The red lines mark the Fermi energy.

Simulations using *V5.3.3*

The first possible reason for strong instead of weak interaction of P2O with Ag(111) is the influence of the unit cell size. As explained earlier, *V5.3* applies the vdW correction also to the substrate atoms and, therefore, requires a smaller lattice constant than standard *PBE* calculations (see Sec. 4.2). Having *V5.3.3* with the *sVDW* expansion available it was possible to resimulate the system with the *PBE* lattice constant.
The enlargement of the P2O on Ag(111) unit cell due to the changed lattice constant amounted to about 0.5 Å in the widest direction. Still no significant change in adsorption height could be observed when using *sVDW* (see Tab. 9).
Subsequently, several further tests were done to probe the bonding behaviour of this system, which will be briefly reviewed in the following. It turned out that using the exact unit cell as Heimel et al. in Ref. [45] led to weak bonding, but trying to reproduce this result with self-build unit cells failed. There appears to be a delicate balance causing the system to behave either one or the other way. To find the crucial parameter the simulation was redone with varied parameters several times. These variations are listed in the following and the (relevant) resulting adsorption heights are summarized in Tab. 9.

- The smearing parameter $SIGMA$ was reduced from the default $SIGMA = 0.2$ to $SIGMA = 0.02$.
- The adopted unit cell which led to weak bonding was simulated without surface relaxation, because the lattice constant used by Heimel et al. slightly differs from the Ag *PBE* lattice constant in this work.
- To check the influence of the lattice constant, the value used by Heimel et al. was adopted ($a = 4.156$ instead of the *PBE* lattice constant $a = 4.154$ for Ag used here).
- The bonding behaviour is determined by an interplay of the electron affinity of the molecule and the work function of the substrate, as shown by the pentacene derivatives on Au(111) and Cu(111). To modify the molecular part, the relative position of oxygen atoms to the carbon backbone can be varied. Therefore, the flat starting geometry of the molecule was modified and the oxygen atoms were bent down 0.15 Å (0.40 Å) relative to the backbone. Additionally, a fully geometry relaxed molecule from a geometry optimisation of the molecule-metal interface was lifted 1 Å away from its equilibrium position and a new geometry relaxation was started. But this also did not lead to different adsorption heights (results not shown).

The P2O on Ag(111) systems seems to exhibit two different adsorption possibilities: Strong bonding at a low distance, and weak bonding at a bigger distance. A binding energy curve which shows the binding energy at different adsorption distances should

help to examine these possible outcomes in more detail. As two outcomes are possible, the binding energy curve should display two minima. A quick test was performed, positioning the flat molecule in several adsorption distances between 2.70 and 3.50 Å above the surface and performing single point calculations, and the result is shown in Fig. 8. When drawing the binding energy curve a parable with only one minimum at 2.98 Å adsorption distance was found. To find an accurate binding energy curve in would most likely be necessary to keep the molecular backbone (or at least a part of the carbon atoms) on different fixed adsorption heights and relax the rest of the molecule, as the bending of the oxygen atoms should have an impact on the substrate sided electron affinity of the molecule and, therefore, on the adsorption. A similar effect was shown for F4TCNQ on Ag(111) by Hofmann et al. [21]. The other factor determining the adsorption is, as explained above, the metal work function. Tuning these two parameters should make the transition between "weak" physisorptive and strong "chemisorptive" interaction visible. This could be a very interesting matter to investigate, as there seems to be no continuous transition but rather a sharp switching between these two cases. Further simulations concerning the P2O on Ag(111) system will be done in the future, the first step being a stepwise work-function tuning of the Ag substrate, which can, for example, be obtained by "alloying" the substrate with different metal atoms and therefore adding electrons to or removing electrons from the system.

Table 9: Variation of the simulation conditions: Computed average adsorption heights of C (h_C) and O (h_O) atoms of P2O on Ag(111) using *V5.3.3* with different simulation conditions to test the variability of the adsorption behaviour. The standard value for the smearing parameter was $SIMGA = 0.2$ eV.

P2O / Ag(111)	h_C [Å]	h_O [Å]
V5.3(WS), soft PAW potentials	2.81	2.52
sVDW, normal PAW potentials	2.87	2.55
sVDW, less smearing ($SIGMA = 0.02$), normal PAW potentials	2.87	2.73
sVDW, no surface relaxation, normal PAW potentials	2.98	2.73
sVDW, smaller lattice constant ($a = 2.939$), normal PAW potentials	3.00	2.84
sVDW, O bent down 0.15 Å, normal PAW potentials	2.99	2.80
sVDW, O bent down 0.40 Å, normal PAW potentials	3.00	2.84

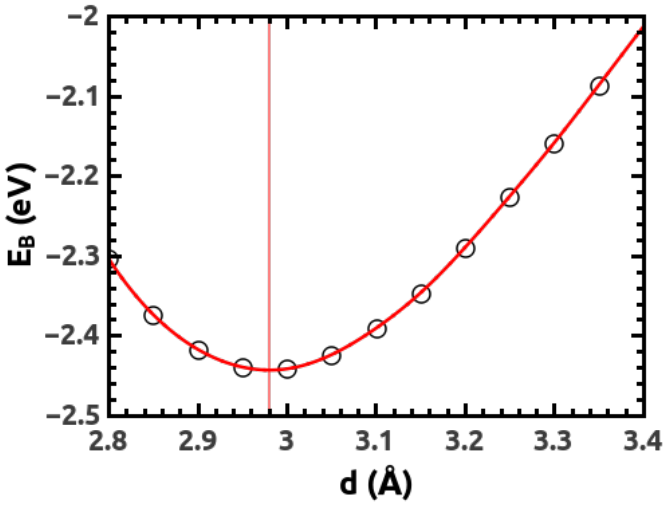

Figure 8: Binding energy curve of P2O on Ag(111). The flat molecule is positioned at different adsorption heights above the surface and the binding energy E_B is calculated. Soft PAW potentials were used.

5.2 Planar phthalocyanines

The second group of planar molecules which was investigated in this work are planar phthalocyanine molecules. The adsorption behaviour of copper and zinc phthalocyanine on Au(111) and Ag(111) was previously simulated by Yu Li Huang, using VASP 5.3 and vdW^{surf} implemented by Wissam A. Saidi. The investigation of these systems presented here is based on the work by Yu Li Huang, and the unit cells and the starting geometries of the the molecules used for CuPc on ZnPc systems are modified versions of the input originally used by her. The results presented in the following about the adsorption of CuPc and ZnPc on Au(111) and Ag(111), along with experimental results are presented in Ref. [14], with Yu Li Huang and the author of this work acting as equally contributing first authors.
The geometric and electronic properties of metal phthalocyanine molecules (MPcs) as well as their adsorption behaviour on metallic surfaces is mostly controlled by the centring metal atom [85, 86, 87]. The denomination *planar* is not totally accurate, as some of these molecules already arrange in a non-planar geometry in the gas phase due to the size of the centring atom (e. g. SnPc [85]), while most of them deviate from the planar form upon adsorption. The notation *planar* was mainly chosen for the sake of distinguishing between systems with only one metal atom in the middle as CuPc or ZnPc and systems with another atom attached to the centring metal, perpendicularly to the molecular backbone as chlorgallium phthalocyanine (GaClPc).
Another factor which changes the molecular properties is fluorination [88, 89], which was tested here on the CuPc and the ZnPc molecule on Cu(111). The structures of a phthalocyanine and a fully fluorinated phthalocyanine molecule are shown in Fig. 9.
In this work, several phthalocyanine molecules (CuPc, FCuPc, ZnPc, FZnPc and SnPc) were studied on Au(111), Ag(111) and Cu(111).

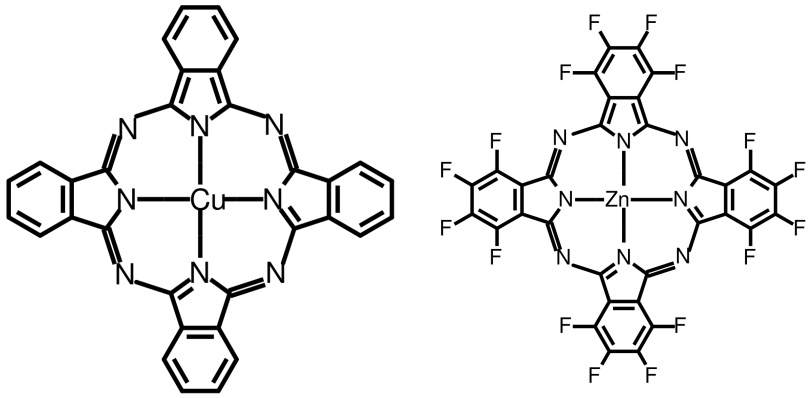

(a) CuPc molecule (b) FZnPc molecule

Figure 9: Structure of the planar CuPc and FZnPc molecules.

5.2.1 Copper phthalocyanine (CuPc) and fluorinated copper phthalocyanine (FCuPc)

The CuPc molecule contains an odd number of electrons, which makes it challenging to analyse as spin-polarised simulations are necessary. It was mentioned earlier that this is much more time-consuming than standard geometry optimisations due to the fact the spin adds an additional degree of freedom. Depending on the system, this can multiply the demanded simulation time, especially in case of strong charge transfer between molecule and substrate, with a prototypical system being CuPc on Ag(111).

experimental data
Kroeger et al. [90, 91] measured annealed CuPc films using SPA-LEED to determine the lateral structure and NIXSW to determine the adsorption heights. The experimental results used for comparison here were measured with full coverage at 300 K.
The lateral structure of CuPc and FCuPc on Cu(111) is based on room temperature STM measurements reported by Oteyza et al. in Ref. [89]. Also the experimental adsorption distances of FCuPc, which are given in Tab. 12, are taken from [89], where XSW measurements at room temperature of these structure are reported.
The work function modifications are determined by room temperature UPS measurements reported by Huang et al. [14].

unit cells and input
(based on Ref. [90], [91] and [92] for Au and Ag and on Ref. [93] and [89] for Cu substrates)

- CuPc on Au(111): 3 layers, 90 atoms $\begin{bmatrix} 5 & 0 \\ 3 & 6 \end{bmatrix}$, see Fig. 10 (a)
- CuPc on Ag(111): 3 layers, 90 atoms $\begin{bmatrix} 5 & 0 \\ 3 & 6 \end{bmatrix}$, see Fig. 10 (a)
- CuPc on Ag(111), bigger unit cell: 3 layers, 108 atoms $\begin{bmatrix} 6 & 0 \\ 3 & 6 \end{bmatrix}$, see Fig. 10 (b)
- CuPc on Cu(111): 3 layers, 102 atoms $\begin{bmatrix} 5 & -1 \\ 4 & 6 \end{bmatrix}$, see Fig. 10 (c)

As a starting point, planar molecule geometries and a distance of about 3.5 Å to the top metal layer were chosen.
The energy cutoff was set to 295.446 eV for all systems.

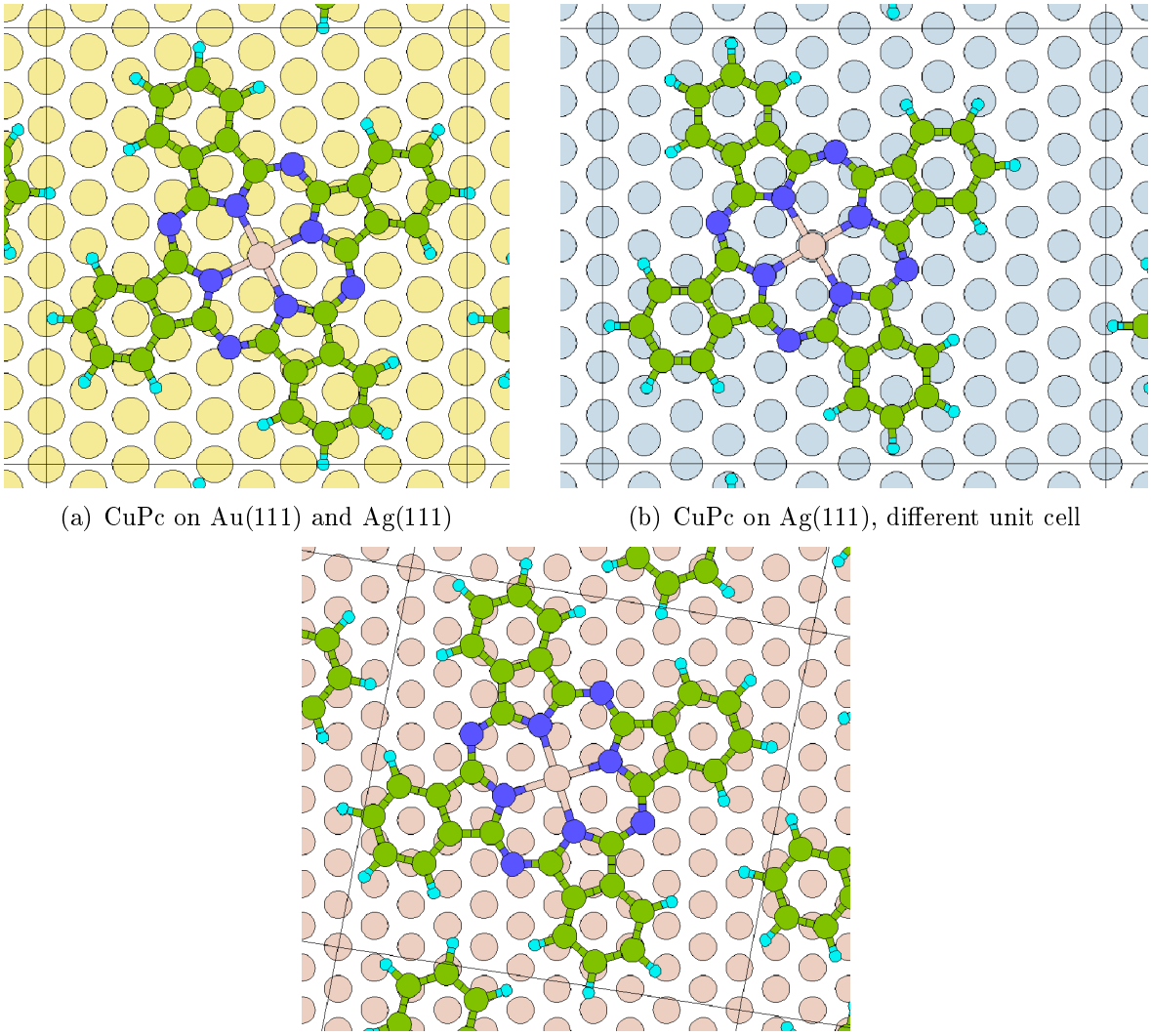

(a) CuPc on Au(111) and Ag(111)

(b) CuPc on Ag(111), different unit cell

(c) CuPc on Cu(111)

Figure 10: Top view of the unit cell geometries of CuPc on Au(111) and Ag(111) (a), CuPc on Ag(111) using the original, bigger unit cell (b) and CuPc on Cu(111) (c).

results

Tab. 10 lists the adsorption heights of CuPc on on Au(111) and Ag(111), simulated using *sVDW* and soft PAW potentials. Full geometry relaxations of the systems were performed and the results are in good agreement with experimental outcomes. As part of the experimental results (CuPc on Au(111)) are given relative to the topmost metal layer, the simulation results are reported here both relative to the hypothetical position of the unrelaxed topmost metal layer and also relative to the relaxed topmost metal layer. While the experimental outcomes are presented under the assumption of a 3% outward relaxation of the highest Au layer [90], the simulations show an inward relaxation (see Sec. 5.2.3). This disagreement is not unexpected, as gold displays long-range surface reconstructions, which can not be considered in the simulations done here because a much larger unit cell would be demanded.

According to the simulated and experimental adsorption heights, CuPc exhibits smaller bonding distances on Ag(111) than on Au(111). CuPc on Ag(111) also exhibits a higher distortion of the centring Cu relative to the C backbone. The molecule exhibits the smallest adsorption height on the Cu(111) surface, but, in spite of the strong bonding, there is no large distortion of the molecule.

The bonding of CuPc on Au(111) and Ag(111) is investigated in more depth by obtaining a binding energy curve (see Fig. 11), which shows the difference between the total system energy and the energies of the monolayer and the metal slab (see Eq. 23) as a function of the distance between molecule and substrate. The geometries from the full geometry relaxations performed earlier are applied, the distance is given relative to the average position of the carbon atoms. Both pure *PBE* and *PBE* + vdW^{surf} results are shown.

$$E_B = E_{Sys} - (E_{ML} + E_{Slab}) \tag{23}$$

The presented binding energy curves can suit as an excellent example of the necessity of a vdW correction in DFT for metal-organic systems. While both systems do not display bonding behaviour when simulated using *PBE*, a pronounced minimum can be seen in the binding energy curves for *PBE* + vdW^{surf}, with a binding energy amounting up to nearly 4 eV per molecule. This surprisingly large value is cause by the large number of atoms in one phthalocyanine molecule (57 atoms). The binding energy on Ag is by about 0.6 eV larger than on Au.

The calculation of the binding energy curves turned out to be somehow problematic because of the necessity to perform it in a spin-polarized manner. For several (unrealistically large or small) bonding distances, no convergence due to problems with the spin could not be obtained at first. Therefore, it was necessary to perform all calculations without spin-polarisation and using the obtained *WAVECAR* and *CHGCAR* files (information on wave functions and charge density) for a second, spin-polarized simulation. The convergence still was very slow in some cases, but finally satisfactory results could be obtained for all distances, leading to a spin of about $\mu \approx 0.9\mu_B$.

Table 10: Computed average adsorption heights (h_{sVDW}) of the CuPc molecule on Au(111), Ag(111) and Cu(111) using *sVDW* with soft PAW potentials, compared with experimental NIXSW values (h_{NIXSW}) from Ref. [90] and [91] for Au and Ag (measured with full coverage at 300 K) and [89] for Cu. Black values represent the distance relative to the relaxed topmost metal layer (experimental Au values: an outward relaxation of 3% of the topmost Au layer has been assumed, based on measurements for clean Au(111)). Red italic values represent the distance to the unrelaxed topmost metal layer.

	Au(111)		**Ag(111)**		**Cu(111)**	
	h_{sVDW} [Å]	h_{NIXSW} [Å]	h_{sVDW} [Å]	h_{NIXSW} [Å]	h_{sVDW} [Å]	h_{NIXSW} [Å]
Cu	3.15	3.25	2.84	-	2.75	-
	3.13	*3.32*	*2.81*	*2.97*	*2.71*	-
C	3.18	3.31	2.95	-	2.74	-
	3.16	*3.38*	*2.91*	*3.08*	*2.69*	*2.79*
N	3.22	3.26	2.94	-	2.81	-
	3.20	*3.33*	*2.90*	*3.04*	*2.77*	*2.69*
H	3.11	-	2.95	-	2.72	-
	3.10	-	*2.95*	-	*2.67*	-

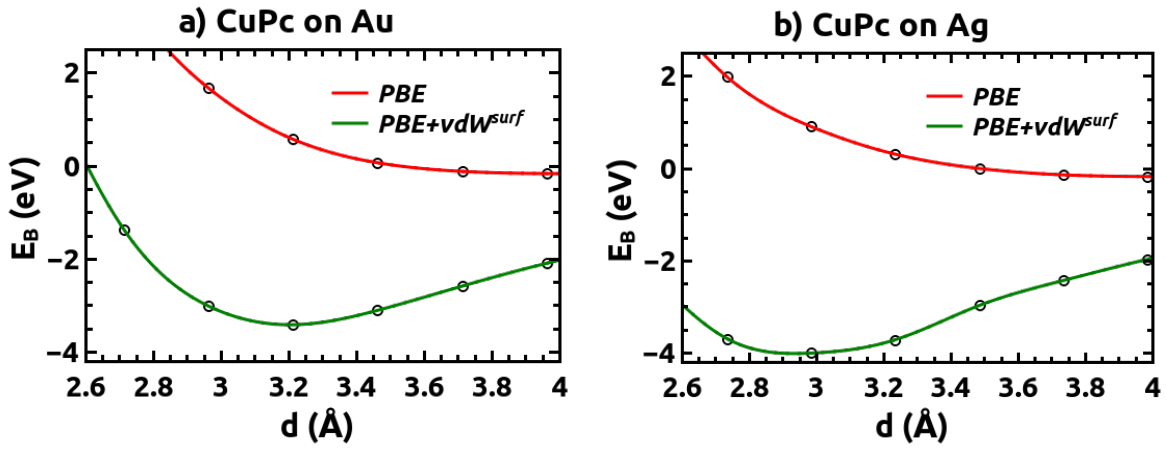

Figure 11: Binding energy E_B of CuPc adsorbed on Au(111) (a) and Ag(111) (b) as a function of the height h between the average position of the molecule carbon atoms and the average position of the relaxed topmost metal layer. Soft PAW potentials were used. This graph is taken from [14].

Comparison of standard *V5.3.3* and *sVDW* for CuPc on Au(111) and Ag(111)

CuPc on Au(111) and Ag(111) were calculated using both *V5.3.3* and *sVDW*. A comparison of the results of these two different approaches will be presented in the following. The unit cell of CuPc on Ag(111) differs slight from that used for calculations mentioned before as it contains 108 instead of 90 substrate atoms (see Fig. 10 (b)).

The computed average adsorption heights are shown in Tab. 11, comparing the results of *V5.3.3* ($h_{V5.3.3}$) and *sVDW* (h_{sVDW}) calculations, where the vdW interactions between the substrate atoms are switched off. As it has been discussed in earlier chapters, the binding energy differs for two reason when comparing *V5.3.3* and *sVDW*. Firstly, geometry relaxations have to be performed with a different lattice constant, which causes the unit cell to be bigger for *sVDW* calculations (around 0.15 Å in each direction for Au and 0.50 Å in each direction for Ag in the present case). Secondly, as shown for PTCDA on Ag(111), the vdW coefficients differ.

The results for CuPc exhibit small differences in adsorption heights, ranging between 0.01 and 0.10 Å.

The PTCDA on Ag(111) simulation (see Seq. 4.2) did not include the variation of lattice constant and therefore unit cell size for different implementations, which is necessary for geometry optimisations. When applying *sVDW*, the binding energy curve of PTCDA on Ag(111) displayed only a vertical and no horizontal displacement, so there is a change in binding energy but the minimum remains at the same position. This means that different vdW coefficients presumably do not strongly contribute to the shifting of the bonding distances when applying *sVDW*, but differences mostly stems from the modified unit cell size. Indeed, a change of adsorption distances due to closer packing of adsorbed molecules has been reported for several systems [91, 94].

Table 11: Comparison of standard *V5.3.3* and *sVDW* for CuPc on Au(111) and Ag(111). Simulated average adsorption heights h of the Pc molecule on Au(111) and Ag(111) values relative to the unrelaxed topmost metal layer are shown. The *V5.3.3* values ($h_{V5.3.3}$) are compared to *sVDW* values (h_{sVDW}), and soft PAW potentials were used. CuPc on Ag(111) was calculated with a slightly bigger unit cell here compared to previous calculations (108 instead of 90 substrate atoms).

	Au(111)		**Ag(111)**	
	$h_{V5.3.3}$ [Å]	h_{sVDW} [Å]	$h_{V5.3.3}$ [Å]	h_{sVDW} [Å]
Cu	3.23	3.13	3.03	3.02
C	3.26	3.16	2.99	2.96
N	3.29	3.20	3.06	3.04
H	3.20	3.10	2.92	2.89

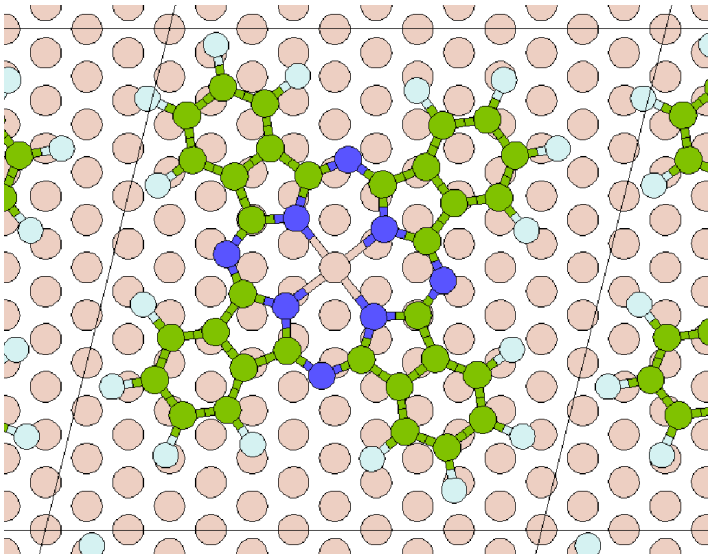

Figure 12: Top view of the unit cell geometry of FCuPc on Cu(111).

FCuPc on Cu(111)
The adsorption behavior of a molecule is also changed by fluorination, which was tested for the example of FCuPc on Cu(111).

unit cell and input
(based on Ref. [89])

- FCuPc on Cu(111): 3 layers, 126 atoms $\begin{bmatrix} 6 & 0 \\ 7 & 5 \end{bmatrix}$, see Fig.12

The energy cutoff was set to 289.825 eV for the *V5.3* calculations with "old " PAW potentials and to 295.446 eV for sVDW calculations with "new " PAW potentials.

results
Tab. 12 lists the adsorption heights of FCuPc on Cu(111), calculated with *V5.3* and *sVDW*. Compared to the non-fluorinated molecule, the centring Cu is closer to the substrate, while the molecular backbone has moved further away from the Cu substrate. While CuPc on Cu(111) exhibits a mainly flat geometry, FCuPc on Cu(111) forms a cone-like structure. This deformation is more distinct in case of the *V5.3* simulation, where the molecular distortion amounts to about 0.7 Å.
The simulation and experimental outcomes do not agree on this matter, although the calculated results are nearly within 0.2 Å to the measured adsorption heights. Fitting of the experimental data suggests a flat geometry of the molecule, with upward-bending of the F atoms.

Table 12: Computed average adsorption heights of the FCuPc molecule on Cu(111), measured relative to the unrelaxed topmost Cu layer. $h_{V5.3}$ and h_{sVDW} give the adsorption heights of every element for the different simulation methods, using soft PAW potentials. h_{exp} gives the XSW results from Ref. [89].

FCuPc / Cu(111)	$h_{V5.3}$ [Å]	h_{sVDW} [Å]	h_{exp} [Å]
Cu	2.54	2.62	2.68
C	3.08	2.89	2.68
N	2.86	2.76	2.68
F	3.26	3.04	3.21

Table 13: Calculated work function modification $\Delta\phi_{calc}$ caused by the adsorption of the CuPc and FCuPc molecules on different substrates, compared to experimental UPS results $\Delta\phi_{exp}$ [14]. In all cases the simulations using *sVDW* are adducted and soft PAW potentials were used.

	$\Delta\phi_{calc}$ [eV]	$\Delta\phi_{exp}$ [eV]
CuPc / Au(111)	-0.69	-0.69
CuPc / Ag(111)	-0.44	-0.44
CuPc / Cu(111)	-0.69	-
FCuPc / Cu(111)	-0.21	-

Work function modifications

The CuPc on Au(111) and Ag(111) systems were also investigated in more depth concerning their electronic properties, which will be discussed in more depth in Sec. 6. The work function modifications of Au(111), Ag(111) and Cu(111) caused by the adsorption of the CuPc and FCuPc molecule are presented in Tab. 13, calculated with *sVDW* (Tab. 10 and Tab. 12) and compared to experimental UPS results for the Au(111) and Ag(111) substrate. In both cases the agreement between calculation and experiment is excellent.

5.2.2 Zinc phthalocyanine (ZnPc) and fluorinated zinc phthalocyanine (FZnPc)

The ZnPc molecule is, due to its even number of electrons, less complicated to simulate than CuPc, as there is no need to perform cumbersome spin-polarised simulations. Aside from that, ZnPc was treated equally to CuPc on Au(111) and Ag(111), with the same unit cell sizes, a planar molecular geometry and a distance of about 3.5 Å to the top metal layer as a starting point.

experimental data
Yamane et al. present results of XSW measurements of ZnPc and FZnPc on Cu(111) in Ref. [88] at 300 K. Unfortunately, no experimental data on the adsorption heights of ZnPc on Au(111) and Ag(111) could be provided.

unit cells and input
(based on Ref. [95] for Au and Ag substrate and on Ref. [88] for Cu substrate)

- ZnPc on Au(111): 3 layers, 90 atoms $\begin{bmatrix} 5 & 0 \\ 3 & 6 \end{bmatrix}$, see Fig. 13 (a)
- ZnPc on Ag(111): 3 layers, 90 atoms $\begin{bmatrix} 5 & 0 \\ 3 & 6 \end{bmatrix}$, see Fig. 13 (b)
- ZnPc on Cu(111): 3 layers, 168 atoms $\begin{bmatrix} 7 & 0 \\ 2 & 8 \end{bmatrix}$, see Fig. 14 (a)

The energy cutoff was set to 279.692 eV for the systems on Au(111) and Ag(111) and to 295.446 eV for the systems on Cu(111).

results
Tab. 14 lists the adsorption distances of ZnPc on Au(111), Ag(111) and Cu(111), calculated with *sVDW* and soft PAW potentials.
Similar to the adsorption of CuPc, the lowest adsorption heights and are found on Cu(111), Ag(111) is an intermediate case and the largest bonding distances are observed on Au(111). The distortion of the molecule ranges between 0.2 Å on Ag(111) to 0.28 Å on Au(111).

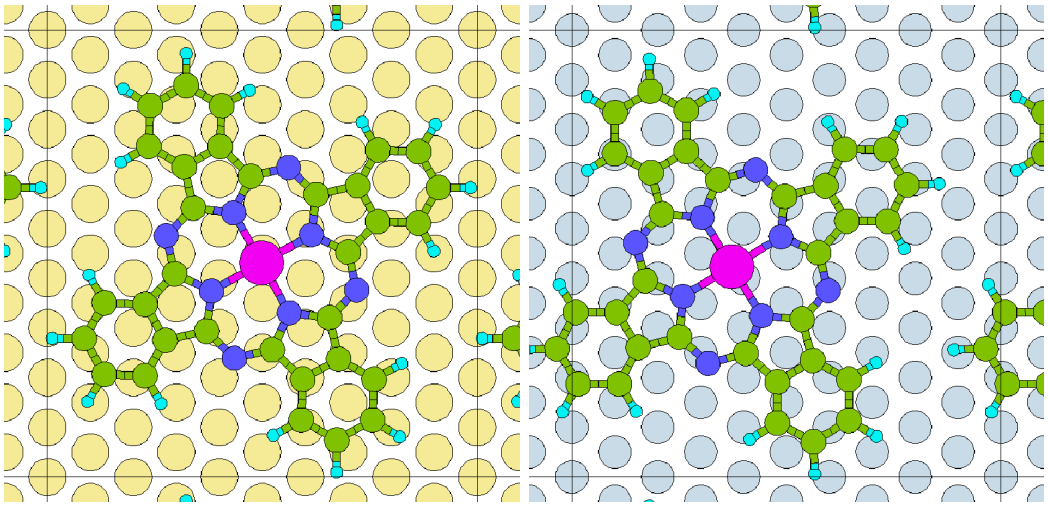

(a) ZnPc on Au(111) (b) ZnPc on Ag(111)

Figure 13: Top view of the unit cell geometries of ZnPc on Au(111) (a) and Ag(111) (b).

Table 14: Computed average adsorption heights of the ZnPc molecule on Au(111), Ag(111) and Cu(111) using *V5.3.3* with *sVDW* and soft PAW potentials. The adsorption heights are compared with experimental XSW values for ZnPc on Cu(111) (h_{XSW}) from Ref. [88] (measured with a coverage of 0.7 ML at 300 K). Black values represent the distance relative to the relaxed topmost metal layer. Red italic values represent the distance to the unrelaxed topmost metal layer.

ZnPc	**Au(111)**	**Ag(111)**	**Cu(111)**	
	h_{sVDW} [Å]	h_{sVDW} [Å]	h_{sVDW} [Å]	h_{XSW} [Å]
Zn	2.89	2.73	2.37	2.25
	2.88	*2.70*	*2.40*	-
C	3.17	2.93	2.62	2.49
	3.15	*2.90*	*2.66*	-
N	3.17	2.94	2.68	2.55
	3.16	*2.90*	*2.72*	-
H	3.13	2.92	2.63	-
	2.12	*2.89*	*2.66*	-

As there was no detailed experimental information on ZnPc on Cu(111) available the unit cell for this systems had to be guessed. Therefore, this system was chosen as a test-case for studying on the influence of the unit cell size on the adsorption distance, which has been discussed e.g. by Kroeger et al. [91], where for CuPc on Ag(111) a trend towards larger adsorption heights for increasing coverage is reported. Mete el al. [94], for pentacene on Ag(111), also report a similar behaviour, where increasing the packing density leads to stronger intermolecular forces, which causes a weakening of the molecule-substrate interaction and, therefore, an enlargement of the bonding distance.

Dependence of coverage

ZnPc on Cu(111) was recalculated twice, using a bigger (216 atoms) and a smaller (126 atoms) unit cell. These unit cell geometries are shown in Fig. 14. The area occupied by one molecule was decreased to about 75% of the original value for the smaller unit cell and increased to about 130% of the original value for the bigger unit cell.

unit cells and input

- "normal" unit cell: 3 layers, 168 atoms $\begin{bmatrix} 7 & 0 \\ 2 & 8 \end{bmatrix}$, see Fig. 14 (a)
- "small" unit cell: 3 layers, 126 atoms $\begin{bmatrix} 6 & 0 \\ 2 & 7 \end{bmatrix}$, see Fig. 14 (b)

- "large" unit cell: 3 layers, 216 atoms $\begin{bmatrix} 8 & 0 \\ 2 & 9 \end{bmatrix}$, see Fig. 14 (c)

The energy cutoff was set to 279.692 eV for the systems on Au(111) and Ag(111) and to 295.446 eV for the systems on Cu(111).

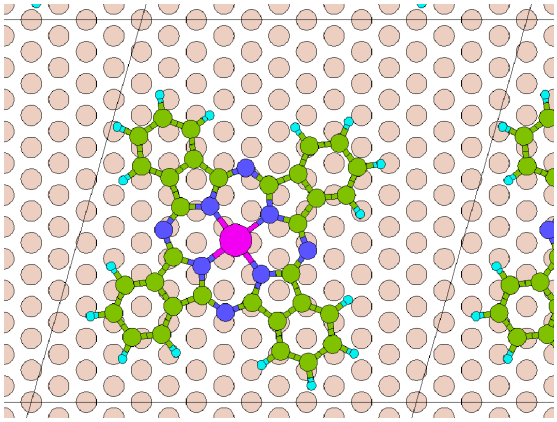

(a) normal unit cell

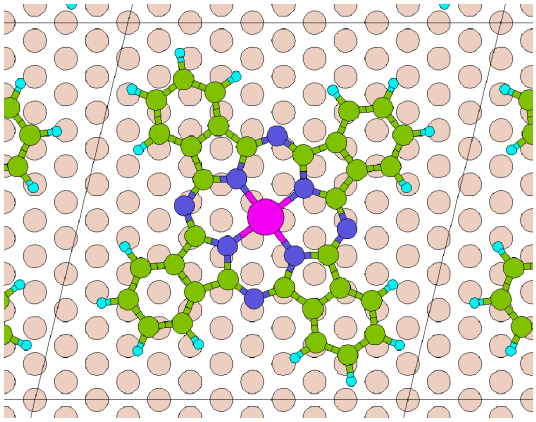

(b) small unit cell

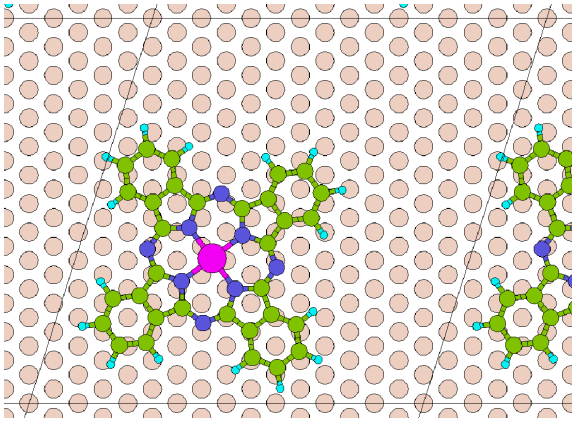

(c) big unit cell

Figure 14: Top view of the unit cell geometries of ZnPc on Cu(111). (a) shows the orignal sized unit cell, (b) and (c) show smaller and bigger unit cells, respectively, to test the influence of unit cell size on the adsorption distance.

results

The simulation results of ZnPc on Cu(111) using three different unit cell sizes are listed in Tab. 15. The adsorption heights follow the expected trend and decrease, as the unit cell size is increased an the molecules are moved further apart, but the change is minimal (0.06 Å at most). It is not very likely that the ZnPc molecule will adsorb in an even larger unit cell on Cu(111), as many similar systems have been investigated and mostly exhibited much smaller unit cells than the one used here.

Table 15: Comparison of different unit cells: Computed average adsorption heights of ZnPc on Cu(111), measured relative to the unrelaxed topmost Cu layer. Three different unit cells were simulated: small (126 substrate atoms), normal (168 substrate atoms, as presented in Tab. 14) and large (216 substrate atoms). All simulations were performed using *sVDW* and soft PAW potentials.

ZnPc / Cu(111)	h_{small} [Å]	h_{normal} [Å]	h_{large} [Å]
Zn	2.40	2.40	2.39
C	2.71	2.66	2.64
N	2.75	2.72	2.71
H	2.69	2.66	2.63

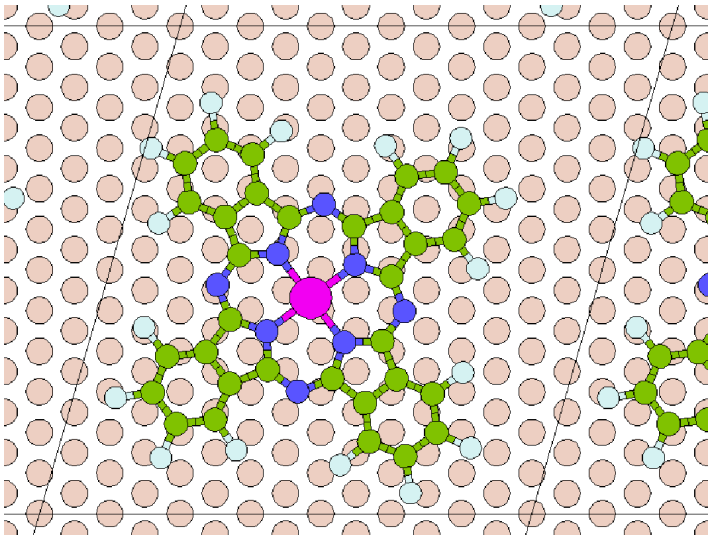

Figure 15: Top view of the unit cell geometries of FZnPc on Cu(111).

FZnPc on Cu(111)
The second fluorinated system (after FCuPc on Cu(111)) which was tested here is FZnPc on Cu(111), which was chosen because experimental information on the adsorption heights by Yamane et al. [88] is available. But similar to ZnPc on Cu(111), not detailed information on the unit cell was available and it had to be guessed, based on the data given in Ref. [88].

unit cell and input
(based on Ref. [88])

- FZnPc on Cu(111): 3 layers, 168 atoms $\begin{bmatrix} 7 & 0 \\ 2 & 8 \end{bmatrix}$, see Fig. 15

The energy cutoff was set to 289.825 eV.

results
The results of the geometry optimisation of FZnPc on Cu(111) with *V5.3* and soft PAW potentials are listed in Tab. 16. The agreement between simulation and experiment is not very good, particularly for the C atoms where they differ nearly 0.5 Å. Also the molecular distortion is much higher for the calculations, it amounts to nearly 0.8 Å. Especially the huge hight difference between the centring Zn and the C atoms (0.65 Å) is surprising. Note that no *sVDW* calculation was performed here in the course of this work.

Table 16: Adsorption heights of FZnPc on Cu(111), measured relative to the unrelaxed topmost Cu layer. $h_{V5.3}$ gives the adsorption heights of the different elements simulated with V5.3 and soft PAW potentials, while h_{exp} gives the XSW results from Ref. [88].

FZnPc / Cu(111)	$h_{V5.3}$ [Å]	h_{exp} [Å]
Zn	2.45	2.58
C	3.10	2.66
N	2.96	2.85
F	3.23	3.15

Work function modifications

Similar to CuPc, the work function modifications for all systems were determined and the electronic properties of ZnPc on Au(111) and Ag(111) were investigated in more depth, which will be reported later (Sec. 6). The work function modifications on Au(111), Ag(111) and Cu(111) caused by the adsorption of the ZnPc and FZnPc molecule are presented in Tab. 17, calculated with *sVDW* (*V5.3* for FZnPc on Cu) and compared to experimental UPS results for Au and Ag substrates. In both cases, the agreement between calculation and experiment is excellent. For ZnPc on Cu(111), the work function modifications are reported for the three different unit cells. Increasing the unit cell size and, therefore, decreasing the coverage, as expected, leads to a decrease in the work function modification.

Table 17: Calculated work function modification $\Delta\phi_{calc}$ caused by the adsorption of the ZnPc and FZnPc molecules on different substrates, compared to experimental UPS results [14]. For ZnPc the simulations using *sVDW* were adducted, while FZnPc was calculated using *V5.3*, and soft PAW potentials were used in all cases. For ZnPc on Cu(111) the work function modifications of all three different unit cells (small, normal, large) are given.

	$\Delta\phi_{calc}$ [eV]	$\Delta\phi_{exp}$ [eV]
ZnPc / Au(111)	-0.61	-0.66
ZnPc / Ag(111)	-0.41	-0.43
ZnPc / Cu(111) (small unit cell)	-0.64	-
ZnPc / Cu(111) (normal unit cell)	-0.58	-
ZnPc / Cu(111) (big unit cell)	-0.50	-
FZnPc / Cu(111)	-0.21	-

5.2.3 Surface relaxations of Au(111) and Ag(111)

To make a comparison with XSW results possible, the adsorption heights of molecules in this work are reported relative to the the hypothetical position of the unrelaxed topmost metal layer, which is the value actually determined in XSW experiments. To probe the adsorption process more realistically the topmost metal layer is always given the freedom to relax during geometry optimisations.
When the pristine metal substrate is given the freedom to relax the topmost layer, there already is a change of layer spacing arising from the fact that the used lattice constants are bulk values. When additionally a monolayer is adsorbed on the substrate, the outmost layer spacing is changed again.
Tab. 18 lists the unrelaxed and relaxed layer spacings of a metal slab consisting of three layers of Au(111) and Ag(111) for the pristine and the covered case, adsorbing CuPc and ZnPc monolayers. The covered situations are tested both with *V5.3.3* and *sVDW*.
Both metals exhibit an outward relaxation of the topmost layer when the pristine substrate is simulated. For Au(111) the relaxation amounts to about 0.5% of the original layer spacing, while for Ag(111) it is about 1.5%. This is in contrast to experimental results which state a 3% outward relaxation of the topmost Au(111) layer [96], measured using X-ray scattering. But as the Au surface displays long-range surface reconstructions [97] which cannot be reproduced with the small unit cells applied in this work, this discrepancy is not surprising. For Ag(111), experimental ion scattering results state an inward relaxation of the topmost layer, amounting to about 2.5 % [98]. In the covered case, Au(111) displays an outward relaxation when *V5.3.3* is applied, while *sVDW* leads to an inward relaxation.
Ag(111) on the other hand exhibits inward relaxations of the topmost layer for *V5.3.3* as well as for *sVDW* simulations.

5.2.4 Tin phthalocyanine (SnPc) on Ag(111)

The SnPc on Ag(111) system is experimentally very well investigated [85, 99, 100, 101, 102] and can, according to these measurements, display many different adsorption configurations. The variety of reported lateral structures and adsorption distances indicate a strong dependence of the adsorption structure on sample preparation, coverage and temperature [101].
The SnPc molecule is not planar in gas phase, as the central Sn atom does not lie in the molecular plane. This allows two different adsorption geometries: Sn up and Sn down.

experminetal data
Woolley et al. [101] deposited the SnPc molecules at ca. 300 °C, which results in a

Table 18: Relaxation of the topmost metal of Au(111) and Ag(111) layer during geometry optimisation. Uncovered and covered (CuPc and ZnPc molecules) Au(111) and Ag(111) were calculated with *sVDW* and *V5.3.3*, using soft PAW potentials. h_{unrel} gives the unrelaxed metal layer distances while h_{rel} gives the average distance between the relaxed topmost and unrelaxed second layer. For Ag the bigger unit cell with 108 substrate atoms was used.

Au(111)	h_{unrel}	h_{rel}	h_{unrel} - h_{rel}
pristine Au(111), sVDW	2.41	2.40	0.01
CuPc on Au(111), V5.3.3	2.39	2.46	-0.07
CuPc on Au(111), sVDW	2.41	2.40	0.01
ZnPc on Au(111), V5.3.3	2.39	2.46	-0.07
ZnPc on Au(111), sVDW	2.41	2.39	0.02
Ag(111)	h_{unrel}	h_{rel}	h_{unrel} - h_{rel}
pristine Ag(111), sVDW	2.40	2.37	0.03
CuPc on Ag(111), V5.3.3	2.33	2.30	0.03
CuPc on Ag(111), sVDW	2.40	2.37	0.03
ZnPc on Ag(111), V5.3.3	2.33	2.30	0.03
ZnPc on Ag(111), sVDW	2.40	2.36	0.04

coverage of ca. 0.75 ML with one molecule per unit cell. The NIXSW results show adsorption in the Sn down configuration.
In contrast to this deposition on a hot substrate, Stadler et al. [100] evaporated SnPc on Ag(111), which was kept at room temperature. Subsequent annealing at 290°C on the SnPc mulilayered film resulted in a saturated 1 ML film with one molecule per unit cell. This film was investigated at room temperature and showed Sn down configuration. The second structure investigated in [100] is a submonolayer structure with two molecules per unit cell which exists only at lower temperature (below 230 K) and exhibits a mixed Sn up and Sn down configuration with the benzene rings bent towards the surface.
The unit cell investigated in this work was constructed based on Ref. [101].

unit cell and input
(based on Ref. [101])

- SnPc on Ag(111): 3 layers, 99 atoms $\begin{bmatrix} 6 & -1 \\ 3 & 6 \end{bmatrix}$, see Fig. 16

The simulation was started using a flat geometry of the molecule with the Sn atom lying within the molecular plane.
The energy cutoff was set to 279.692 eV.

results

A full geometry optimization using *sVDW* and soft PAW potentials resulted in the adsorption heights presented in Tab. 19 and a bending of the Sn atom toward the surface (see Fig. 17). The simulation results compare well to Ref. [101] for the central Sn atom, which binds strongly to the Ag substrate and increase the deformation of the gas-phase molecule. But while the experimental NIXSW results state an adsorption distance of 3.61 Å for the C atoms, the simulated configuration sets the C atoms to 2.97 Å much closer to the surface. This is in strong contrast to DFT simulations (TURBOMOLE [103], *PBE* functional) reported in [85], which yield good agreement with the experimental outcome, for the central Sn as well as for the C atoms, but as a cluster representation of the Ag substrate and no vdW correction is applied there, this discrepancy is not surprising.

To come to a better understanding of the adsorption of SnPc on Ag(111) it would be necessary to also investigate larger unit cells with several molecules to make mixed Sn up and Sn down structures possible. It would be possible to apply different starting geometries with the Sn already positioned above and below the molecular plane. The outcome of geometry optimisations and the comparison of total energies should then shed light on the adsorption mechanisms of this system.

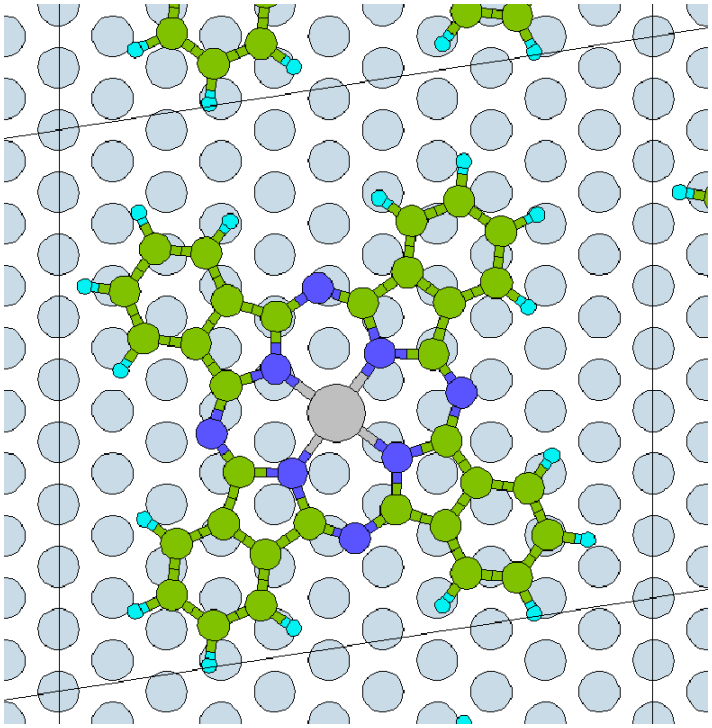

Figure 16: Top view of the unit cells of of SnPc on Ag(111).

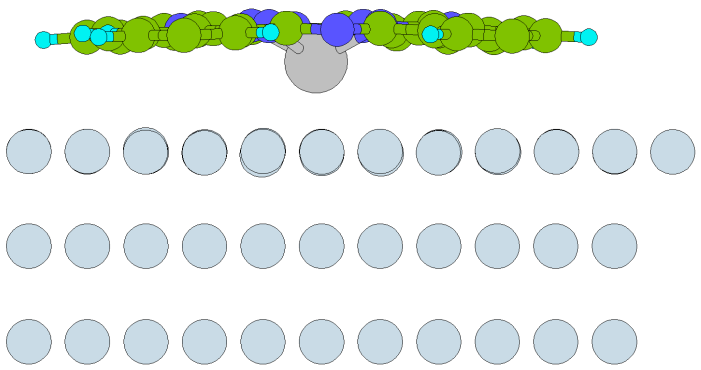

Figure 17: Side view the geometry optimized SnPc on Ag(111). Soft PAW potentials were used.

Table 19: Computed average adsorption heights of SnPc on Ag(111) with a coverage of about 75% , compared to experimental NIXSW values. The computed adsorption heights h are indicated relative to the unrelaxed topmost Ag layer, and soft PAW potentials are used. h_{sVDW} gives the adsorption heights of the different elements simulated with *sVDW* and soft PAW potentials. Several experimental studies of this system exist and the following experimental NIXSW results for adsorption heights are given here: $h_{[1,LT]}$: [100], low temperature, mixed phase; $h_{[1,RT]}$: [100], room temperature, Sn down; $h_{[2]}$: [101], 0.75 ML.

SnPc / Ag(111)	h_{sVDW} [Å]	$h_{[1,LT]}$ [Å]	$h_{[1,RT]}$ [Å]	$h_{[2]}$ [Å]
Sn	2.23	2.59 / 4.01	2.41	2.31
C	2.97	2.93	3.17	3.61
N	3.08	3.12	3.26	
H	2.87			

Table 20: Calculated work function modification $\Delta\phi_{calc}$ caused by the adsorption of the SnPc molecule on Ag(111), calculated with *sVDW* and using soft PAW potentials.

	$\Delta\phi_{calc}$ [eV]
SnPc / Ag(111)	-0.35

Work function modification

The calculated work function modification of the SnPc on Ag(111) system is presented in Tab. 20. Unfortunately, no experimental data could be provided. Using different (bigger) unit cells, as mentioned above, will presumably strongly influence the work function modification. This value should, therefore, be investigated in more detail as soon as these calculations are performed.

5.3 Non-planar phthalocyanines: Chlorgallium phthalocyanine (GaClPc) on Cu(111)

Several simulations of flat-lying organic molecules showed that, within certain limitations, vdW^{surf} is well suited to describe the geometry of planar organic molecules on metal substrates. Also multilayered systems have been described successfully [10].
One of the goals of this work was to investigate non-planar systems like chlorgallium phthalocyanine GaClPc and the ability of $PBE + vdW^{surf}$ to describe the adsorption behaviour of such systems.
GaClPc on Cu(111) was chosen because of the extensive experimental and computational study done by Gerlach et al. [104] providing data on adsorption geometry as well as electronic properties like work function modification. Another similar system with experimental information available is chloraluminum phthalocyanine (ClAlPc) on Cu(111) [105] and Au(111) [106] .
GaClPc is a gallium phthalocyanine molecule with a chlorine atom bond to the centring atom (see Fig. 18). In the gas phase, the molecule deforms slightly from the planar form of the backbone, which adopts a slightly cone-like structure when bending away from the Cl atom [104]. Due to the nonplanar geometry the GaClPc molecule can adsorb in two different configurations: Cl pointing away from the surface (Cl up, Fig. 18 (a)) and Cl pointing towards the surface (Cl down, Fig. 18 (b)).

experimental data

Gerlach et al. studied the adsorption behaviour of GaClPc on Cu(111) using XSW and photoelectron spectroscopy [104]. For submonolayer coverages (0.8 ML), a highly ordered configuration of the monolayer was reported, with Cl down adsorption and an umbrella-like deformation of the molecule. The adsorption heights are shown in Tab. 21. They also report DFT calculations of the molecule using VASP. An geometry optimisation of the gas-phase molecule was performed, but the adsorbed systems was calculated with a fixed geometry taken from experimental results. vdW interactions contribute strongly to the bonding of GaClPc, like for several other systems studied in this work. Therefore, a geometry optimisation using semi-local DFT without applying a vdW correction is hardly possible and Gerlach et al. mainly studied the electronic structure of the system with DFT.

unit cells and input

The unit cell for GaClPc on Cu(111) could only be guessed as no experimental information is available. Therefore, different unit cells were tested. The applied unit cell geometries are showed in Fig. 19.
First the geometry presented in [104] by Gerlach et al. was employed, with the molecular axes parallel to the edges of the unit cell. To avoid too close contact of the molecules a second unit cell was employed were the molecule was rotated by 45°.

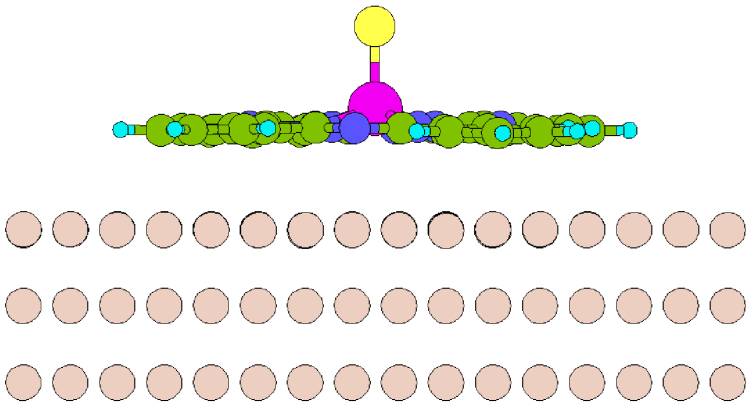

(a) Cl up

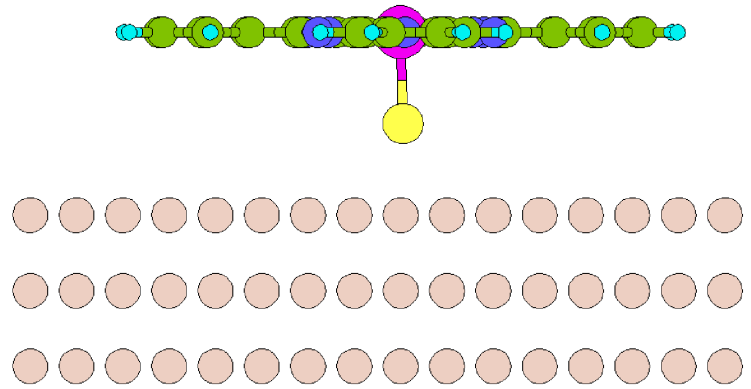

(b) Cl down

Figure 18: Possible adsorption configurations of the GaClPc molecule on Cu(111).

Furthermore, an experimental unit cell based on the chloraluminum phthalocyanine (ClAlPc) unit cell on Au(111) (see Ref. [105]) was used, which is smaller and the molecule is rotated 27° relative to the edges of the cell. This rotation angle was also combined in some cases with the bigger unit cell.

- big unit cell: 3 layers, 168 atoms $\begin{bmatrix} 7 & 0 \\ 4 & 8 \end{bmatrix}$; axes of molecule
  i) parallel to substrate axes
  ii) axes of molecule in a 45°-angle relative to substrate axes
  iii) axes of molecule in the experimental 27°-angle relative to substrate axes
- experimental unit cell: 3 layers, 144 atoms $\begin{bmatrix} 6 & 0 \\ 4 & 8 \end{bmatrix}$; axes of molecule in a 27°-angle relative to substrate axes

The energy cutoff was set to 295.446 eV for calculations with “new” and to 280.000 eV for calculations with“old” PAW potentials.

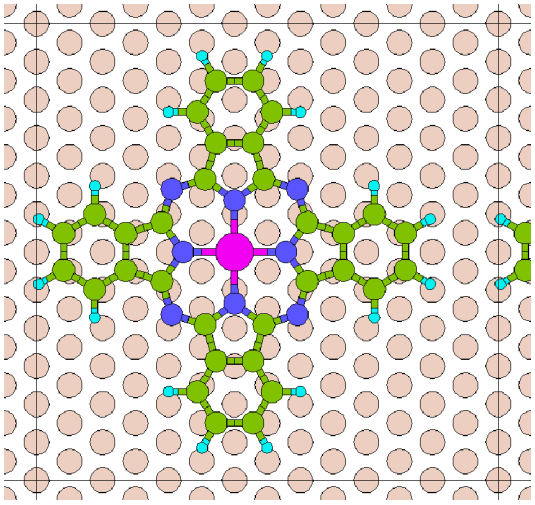

(a) big unit cell, parallel

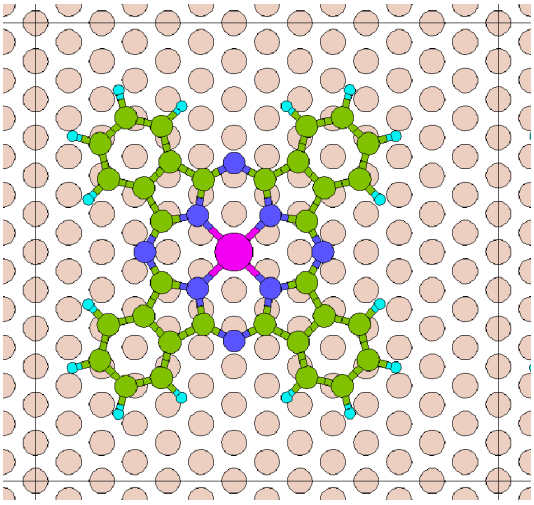

(b) big unit cell, 45°

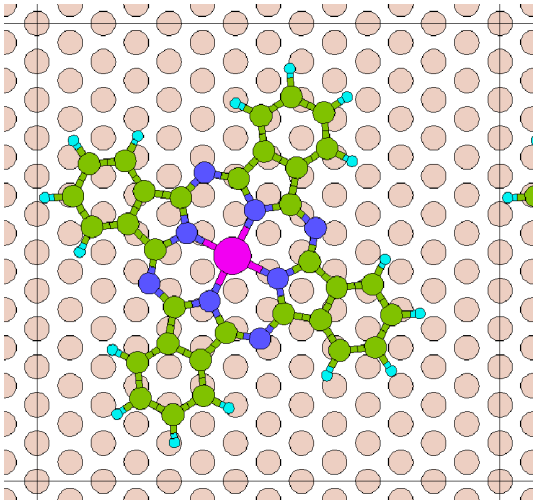

(c) big unit cell, 27° (experimental rotation angle)

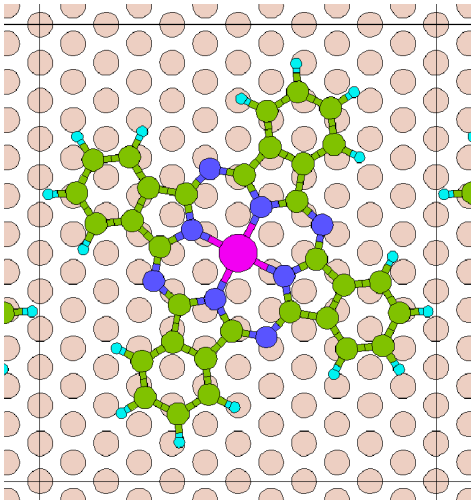

(d) experimental unit cell, 27° (experimental rotation angle)

Figure 19: Top view of all different unit cell geometries of the GaClPc molecule on Cu(111).

The geometry optimisations using GADGET [12] are not capable of turning over a flat-lying molecule, at least not when it is set close to the surface to keep computation time low. Therefore, the Cl up or Cl down configuration have to be chosen already for the input and the molecule has to be positioned accordingly. The Cl atoms were set to the hcp hollow position of the Cu(111) surface in most simulations, only in the tests

performed to check the influence of the starting position this was not the case. The starting configuration of the molecule was a planar geometry of all atoms excluding Cl, which was positioned in a vertical distance of 2.5 Å to the centring Ga. The molecule then was positioned above the surface with 2.5 Å distance between the Cl atom and the topmost Cu layer for the Cl down configuration and with 3.4 Å between the planar backbone and the topmost Cu layer for the Cl up configuration.

5.3.1 Simulations using VASP 5.3

Several variations of the GaClPc on Cu(111) system were simulated, starting with the Cl down geometry, as it was stated by Gerlach et al. First results in the Cl down configuration, using the big unit cell with parallel position of the molecule and soft PAW potentials showed a strong bending of the molecule after geometry optimisation as presented in Fig. 20 (a). This configuration does not seem to be very realistic, as the strong bending of the molecule should be energetically costly.
To investigate if the bending could be caused by the branches of neighbouring molecules lying to close and trying to avoid each other, several variations were tested. A significantly bigger unit cell (270 surface atoms) and different positions of the molecule within the cell were investigated (rotation angles of 45° and 27°). But the bending appeared independent of the relative orientation of the molecules.
To compare total energies, also the Cl up configuration was simulated. Numerous tests were performed, changing unit cell size, adsorption position, rotation angle of the molecule within the cell, adsorption position and input parameters. While the Cl up configuration always led to qualitatively similar results, the Cl down configuration showed two different outcomes: the already mentioned bent geometry and an umbrella-like geometry, with a slight tilting of the umbrella to one side (see Fig. 20 (b)).
Although the umbrella-like geometry looks similar to the results obtained in Ref. [104] at first glance, the bonding distances differ by up to about 1 Å for the C atoms (see Tab. 21).
The two different outcomes for Cl down appear to be two different local minima, but it could not be determined what causes the simulation to run into one or the other of these minima, as it seems to be caused by a complex interplay of the variable factors listed above. The bent geometry exhibits a lower total energy, which will be discussed in more detail later.
The obtained adsorption heights in the Cl down configuration are shown in Tab. 21, all of them resulted in the umbrella-like geometry, except one, where the adsorption heights are denoted as $h_{expUC,bent}$. The calculations were performed with *V5.3* and "new" PAW potentials. Different unit cells, starting angles and optimisation methods are compared. The Cl atom, which is always set in the hcp hollow position of the Cu(111) substrate, stays there and also the molecules do no significantly rotate away from the initially given angle.

The adsorption distance of the Cl atom matches the experiment quite well in all cases, its adsorption distance is always in the range of 1.7-1.9 Å above the Cu(111) surface. But the rest of the molecule adsorbs in totally different heights compared to the experimental outcome. While experiment predicts the Ga atom to lie below the average C height, in all simulations it lies above or on an equal level with the C atoms. The total disagreement in height between simulation and experiment amounts to more than 1 Å for the C atoms for the umbrella-like geometry and 0.8 Å for the bent geometry.
When optimised using GADGET, the molecule slightly tilts in all cases and the Ga-Cl bond is not perpendicular to the surface plane. When the optimisation is on the other hand performed with VASP, it stays perfectly upright (see Fig. 20 (c)). This arises from the cartesian coordinates used for the VASP optimisation, which are not suited to describe tilting, while GADGET uses internal coordinates and can, therefore, describe tilting easily. The upright geometry determined by VASP also proved to be energetically unfavourable by about 0.10 eV.
The bonding distance of Ga-Cl, which is 2.21 Å in the gas phase is enlarged according to experiment, as the height difference between Ga and Cl amounts to 2.33 Å. The simulations also predict an enlargement, the height differences amount to about 2.30 Å in most cases, which means an even higher bond length, as the bond is not parallel to the surface normal, except in case of the VASP optimisation.
The obtained adsorption heights in the Cl up configuration are shown in Tab. 22, tested with two different unit cells and rotation angles. The geometry optimization was performed with GADGET.
The deformation of the molecule was much smaller here, the backbone stayed flat, with the Ga atom slightly out of plane, and a straight Ga-Cl bond relative to the molecular backbone (see Fig. 18 (b)). The angle and lateral position of the molecule did not change significantly during both simulation. Also the obtained heights for both starting configurations are in good agreement. They differ by 0.05 Å at most. The flat geometry with the Ga bending away from the substrate as well as the adsorption heights of the molecular backbone indicate a bonding mostly due to vdW interactions. The Ga-Cl bond length amounts to 2.21 (2.20) Å and is therefore (almost) equal to the gas-phase value.

Table 21: Computed average adsorption heights of the GaClPc molecule on Cu(111) in Cl down configuration using *V5.3* with soft PAW potentials, compared with experimental XSW values (h_{XSW}) from Ref. [104]. Different unit cell sizes (big unit cell ($h_{bigUC,...}$), experimental unit cell ($h_{expUC,...}$), starting angles (parallel ($h_{...,parallel}$), 45° ($h_{...,45°}$), 27° ($h_{...,27°}$)) and geometry optimisation tools (all simulations performed using GADGET except $h_{expUC,27°,VASP}$ which was performed using the geometry optimisation of VASP 5.3) were applied. Furthermore one simulation which shows a "bent" geometry after optimisation ($h_{expUC,tilted}$, see Fig. 20 (a)) unlike all others were an "umbrealla"-like deformation is observed (see Fig. 20 (b) is shown.

Cl down	$h_{expUC,27°}$ [Å]	$h_{bigUC,45°}$ [Å]	$h_{bigUC,parallel}$ [Å]	$h_{expUC,27°,VASP}$ [Å]	$h_{expUC,bent}$ [Å]	h_{XSW}[Å]
Cl	1.74	1.69	1.70	1.78	1.89	1.88
Ga	3.91	3.99	4.01	4.12	3.63	4.21
C	3.31	3.25	3.30	3.45	3.63	4.44
N	3.86	3.85	3.90	4.06	3.79	4.71
H	2.85	2.78	2.82	2.93	3.53	-

Table 22: Computed average adsorption heights of the GaClPc molecule on Cu(111) in Cl up configuration using *V5.3* with soft PAW potentials. Different unit cell sizes (big unit cell ($h_{bigUC,...}$), experimental unit cell ($h_{expUC,...}$) and starting angles (45° ($h_{...,45°}$), 27° ($h_{...,27°}$)) were applied.

Cl up	$h_{expUC,27°}$ [Å]	$h_{bigUC,45°}$ [Å]
Cl	5.46	5.44
Ga	3.24	3.23
C	2.68	2.63
N	2.74	2.72
H	2.67	2.62

Adsorption positions
Up to this point, the Cl down simulation were carried out with the Cl atom of the molecule set to the hcp hollow position of the Cu(111) substrate, as suggested in Ref. [104]. To test the influence of the adsorption position several simulations were carried out, positioning the Cl differently. Tab. 23 lists the behaviour of the molecule during geometry optimisation and the total energies in the relaxed geometry. The tests were carried out using the experimental unit cell and the 27°-configuration.
The Cl atom obviously prefers to adsorb on the hollow site, when set to the bride or on-top position it moves to a hollow position. The fcc and hcp hollow sites are very close in energy, with hcp hollow being more favourable by 0.02 eV.

Table 23: Adsorption behaviour and total energies of the GaClPc molecule on Cu(111) due to different starting geometries. The Cl atom was set to fcc hollow, hcp hollow, on-top or bridge position as starting configuration. Soft PAW potentials were used.

	adsorption behavior	total energy [eV]
fcc hollow	stayed	-1000.83
hcp hollow	stayed	-1000.85
bridge	moved to hcp hollow	-
on top	moved to fcc hollow	-

Total energies and binding energies:
To find out if which one of the configurations (Cl up, Cl down with "umbrella" or "bent" shape) are more favourable, the total energies of these systems were compared, which is only possible for equal unit cells (size, number of atoms) and parameter settings (e. g. cutoff energies). Tab. 24 summarizes the total energies for different calculations using the experimental and big unit cell, respectively. Also the work function modifications $\Delta\phi$ are shown.
For both unit cells the Cl up configuration is energetically clearly more favourable, with the energy being about 2.00 eV lower compared to the Cl down configurations. This is in strong contrast to the results presented in [104].
The two possible deformations of the molecule with Cl pointing down are very close in energy, with the bent geometry being a little bit more favourable (by 0.16 eV).
Also the binding energies of the Cl up and Cl down configuration were compared, the results are shown in Tab. 25. The binding energy is calculated by subtracting the energy of slab and monolayer from the total system energy (see Eq. 23). The same calculation is performed for the vdW part of the total energy, which gives the vdW energy E_{vdW} in Tab. 25.
The binding energy is 0.85 eV (0.73 eV) bigger for Cl up than for Cl down in the umbrella (bent) geometry, respectively, which supports the previous statement of Cl up being the more favourable adsorption geometry. For all three different systems, the

vdW energy is slightly bigger than the binding energy. Therefore, bonding essentially is only due to vdW forces. This means that no adsorbing behaviour of the molecule can be observed when the vdW correction is switched off.

Table 24: Total energies E_{tot} and work function modification $\Delta\phi$ of different configurations of GaClPc on Cu(111) using the experimental unit cell (a) and the big unit cell (b). The molecule is adsorbed in Cl up and Cl down configuration and Cl down is shown with two different resulting geometries ("bent" and "umbrella") in case (a), while it adsorbed only in the umbrella-like form for Cl down in (b). *V5.3* with soft PAW potentials was applied.

a) experimenta UC	E_{tot} [eV]	$\Delta\phi$ [eV]
Cl down, exp UC, 27°, "umbrella"	-1000.80	-0.54
Cl down, exp UC, 27°, "bent"	-1000.96	-0.61
Cl up, exp UC, 27°	-1002.68	-0.22
b) big UC	E_{tot} [eV]	$\Delta\phi$ [eV]
Cl down, big UC, 45°, "umbrella"	-1097.17	-0.56
Cl up, big UC, 45°	-1099.15	-0.25

Table 25: Total energy (E_{Sys}), energy of the monolayer (E_{ML}), energy of the metallic slab (E_{Slab}), binding energy (E_B) and vdW binding energy (E_{vdW}) of GaClPc on Cu(111) for the Cl up compared to the Cl down configuration in the "umbrella" and "bent" geometry. The experimental unit cell with a 27° rotation of the molecules was used, and *V5.3* with soft PAW potentials was applied.

	E_{Sys} [eV]	E_{ML} [eV]	E_{Slab} [eV]	E_B [eV]	E_{vdW} [eV]
Cl down, exp UC, 27°, "umbrella"	-1000.80	-418.28	-579.53	-3.16	-3.61
Cl down, exp UC, 27°, "bent"	-1000.96	-418.15	-579.53	-3.28	-3.56
Cl up, exp UC, 27°	-1002.68	-419.11	-579.55	-4.01	-5.57

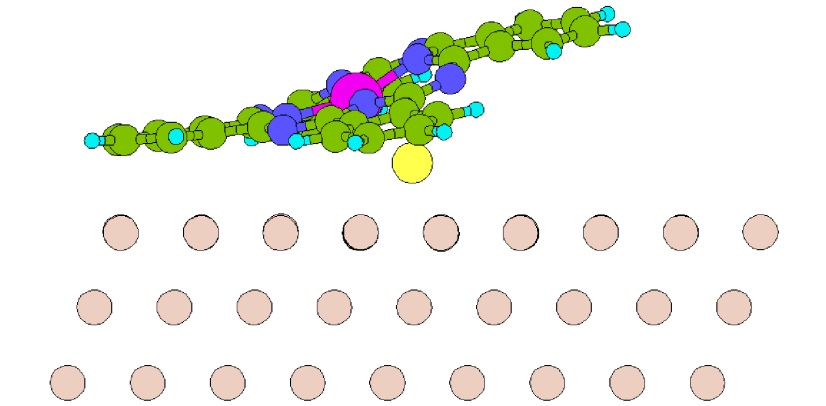

(a)

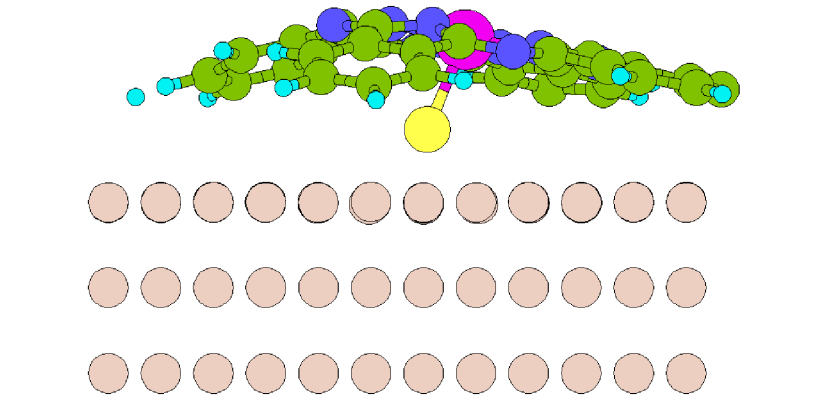

(b)

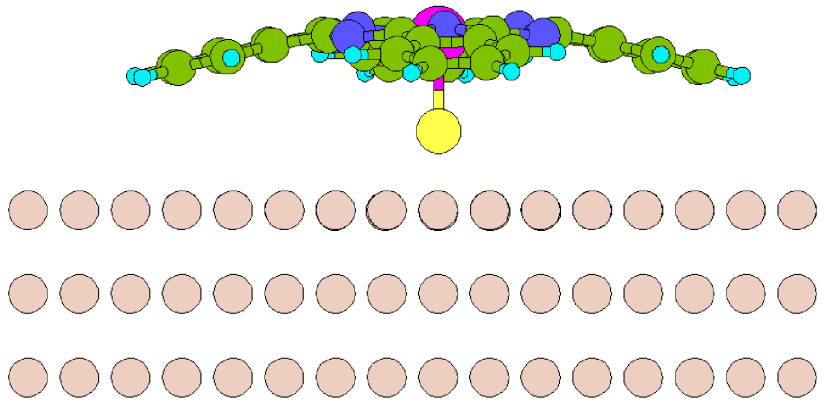

(c)

Figure 20: Adsorption geometries of the GaClPc molecule on Cu(111) in the Cl down configuration. GADGET optimisations with direct coordinates lead to geometries (a) and (b), depending on the starting configuration. VASP optimisation using cartesian coordinates leads to (c).

Further tests

The huge discrepancy between experiment and simulation for GaClPc on Cu(111), not only with totally different adsorption heights of the molecule but also the Cl up instead of the Cl down configuration being energetically more favourable is curious given the good agreement for most flat-lying systems. To rule out general errors of the simulation, further geometry optimisations with altered starting configurations were tested. Firstly, the electronic minimisation algorithm, which is determined by the *ALGO*-tag was set from the usual *ALGO* = *Fast* (a mixture of the blocked Davidson iteration scheme in the initial phase and later switching to RMM-DIIS) to *ALGO* = *Normal* [72]. Also the break condition for the self consistent loop *EDIFF*, giving the minimal energy change of one step [72] was set to $EDIFF = 10^{-6}$ instead of $EDIFF = 10^{-4}$. Normal and hard PAW potentials were used, while before only soft ones were applied for the GaClPC systems. Finally, the starting geometry for the Cl down configuration was modified. Because the Ga molecule is found underneath the carbon backbone in experiments, but lies above this level in the simulations, it was positioned 0.25 and 0.50 Å below the C level as a starting configuration. Furthermore, the umbrella-like geometry of the experiment was reconstructed manually, the molecule in the according shape was set to the usual starting position and a geometry optimisation was performed. Also a gas phase geometry of GaClPc, optimised in a *30x40x40* Å unit cell with GADGET was tested as a starting configuration.

None of the here mentioned testes lead to a qualitatively different outcome than the situations explained and analysed before. Only slight variations of energies and adsorption heights were obtained.

Another scenario was tested where the goal was to place the Cl atom inside the Cu(111) surface. Two variations were considered, with the Cl atom i) positioned on the hollow position of the substrate and ii) replacing a Cu surface atom.

i) The Cl atom was set on the hollow position, levelling with the top layer of Cu atoms. As a consequence the Cu surface layer deformed minimally during geometry optimisation, the Cl atom moved out of the substrate and the Cu surface relaxed into the usual position again.

ii) The simulation with the Cl atom replacing an atom of the Cu(111) surface led to huge problems in the simulation, with the forces between atomic fragments diverging and no convergence could be reached.

"Old" and "new" PAW potentials

The results presented so far were calculated using the "new" 5.3 set of PAW potentials (see Sec. 4.2). To check the influence of different potentials, some geometries were calculated with "old" and "new" PAW potentials and the results were compared. The differences in the obtained adsorption geometries amount up to 0.05 Å and the work functions differ 0.02 eV, which is not problematic. There is a bigger difference in total energies (2.75 eV), but this is not surprising for calculations performed with different PAW potentials, as comparisons of total energies are only possible for similar systems calculated with equal PAW potentials.

Table 26: Average adsorption distances, total energies E_{tot} and work function modification $\Delta\phi$ of GaClPc on Cu(111) using the big unit cell with the 45° rotated position of the molecule and Cl up. The calculation was performed twice, using "old" and "new" soft PAW potentials.

Cl up, big UC, 45°	h_{Cl} [Å]	h_{Ga} [Å]	h_C [Å]	h_N[Å]	h_H [Å]	E_{tot} [eV]	$\Delta\phi$ [eV]
"old" pseudopot.	5.48	3.27	2.66	2.76	2.64	-1101.90	-0.23
"new" pseudopot.	5.44	3.23	2.63	2.72	2.62	-1099.15	-0.25

5.3.2 Simulations using VASP 5.3.3

After switching to the new VASP 5.3.3, the tests on GaClPc on Cu(111) were pursued. Several theories on what could lead to the different outcomes were considered.
The first possibility, which would be quite unsatisfactory but still has to be debated is that $PBE{+}vdW^{surf}$ might not be suited for the calculation of non-planar systems. It has already been successfully applied to multi-layered systems as CuPc on PTCDA on Ag(111) [10], so this is an unlikely possibility.
Secondly, the comparability problems of the simulation performed in this work and the experimental (and computational) outcome of Ref. [104] raises the question if the experimental data could be also be interpreted differently. This would explain why the experimental outcome is the least likely scenario according to simulations.
One possibility is that there could be a mixed phase of Cl up and Cl down molecules on the surface. But it should be possible to distinctively distinguish this situation from a one-directional ordering of all molecules in either Cl up or Cl down configuration from the coherent fraction of the XSW results [107], so this is very unlikely.
The determination of adsorption heights from XSW results when measuring adsorbates on a surface is only possible in multiples of the substrate lattice spacing. Therefore, the molecular atoms could be positioned one (or several) Cu(111) layer spacings above or below the position given in [104]. The experimental Cu(111) layer spacing amounts to 2.08 Å [81]. If the whole molecule is moved one Cu(111) layer spacing closer to the substrate, the Cl atom would be positioned inside the substrate, which has been tested and is unrealistic. What could, however happen in this case is a dissociation of the molecule. While the molecular Pc stays stable, the Cl atom could be removed from the Ga atom and adsorb to the Cu surface somewhere else. This is no unlikely scenario, as the Cl atoms tends to form one chemical bond, which could connect it to the Ga atom of the molecule or to a Cu atom of the substrate.
This possibility has been tested in two different scenarios: First, the Cl atoms was removed from the GaPc molecule and set to the surface in a different adsorption site, with 4.1 Å vertical distance to the closest H atoms of the molecule for the experimental unit cell. The Cl atom was set to an edge of the unit cell, 2.2 Å above the topmost Cu layer, while the GaPc molecule remained in the same positions as shown for earlier simulations, but at a starting height of 3.0 Å above the Cu surface. The adsorption heights for this situation will be denoted as $Cl, 1$ in the following and a side-view is shown in Fig. 21 (a).
The second scenario simulates only the GaPc molecule (also 3.0 Å above the surface as starting configuration), with Cl totally removed from the system, which will be denoted as $Cl, 2$.
These scenarios demand, due to the odd number of electrons in the GaPc molecule and the Cl atom, spin-polarised treatment, which makes the simulations more complicated and computationally more costly.
Tab. 27 lists the adsorption heights obtained when comparing the different investigated configurations using *V5.3.3* and *sVDW*. $h_{Cl,1}$ and $h_{Cl,2}$ give the adsorption heights for

Cl removed from the atom and Cl totally removed from the unit cell, respectively. To be able to compare total energies, also the standard Cl up and Cl down geometries were simulated with *sVDW*. Cl down adsorbed in the bent geometry. For comparison, the experimental adsorption heights h_{XSW} are listed [104]. To test the above mentioned hypothesis of the molecule being one Cu(111) layer spacing closer to the substrate, $h_{XSW,corr}$ show corrected experimental values, with the adsorption heights of Ga, C and N reduced by 2.08 Å.
In the following, only the *sVDW* results are going to be discussed, as *sVDW* is supposedly the best method on hand and the *V5.3.3* calculations were mainly performed for testing reasons.
The outcome of the simulation with Cl adsorbed separately is very interesting, as much better agreement between calculation and experiment than in all earlier GaClPc simulations is found. The simulated adsorption heights of Ga, Cl an N match the corrected experimental values with a maximal difference of 0.10 Å, only the adsorption heights of C differ by 0.28 Å. But in contrast to all earlier Cl down calculations, when the Cl is removed, finally the situation with the Ga molecule below the C backbone of the molecule is obtained. The simulated adsorption geometries with Cl removed from the molecule (a) and Cl remove fully (b) are shown in Fig. 21, as obtained with *V5.3.3*. The reason why no results for the situation with Cl totally removed simulated with *sVDW* are shown here is that a yet not determined problem with this simulation appeared and no convergence could be reached.
The comparison of total energies for the *sVDW* calculations, shown in Tab. 28 gives very interesting insights. The situation with Cl down (bent geometry) is energetically unfavourable compared to Cl up and Cl removed from the molecule. Cl up is by 1.94 eV more favourable than Cl down. The situation with Cl removed (Cl,1) is very close in energy to Cl up, it is more favourable by 0.34 eV.

Table 27: Experimental unit cell: Computed average adsorption heights of the GaClPc molecule on Cu(111) with different molecular configurations: h_{Cldown} stems from a standard Cl down simulation (optimisation gives a bent geometry), $h_{Cl,1}$ from a simulation where the Cl atom is removed from the molecule and set on the surface at the edge of the unit cell while for $h_{Cl,2}$ the Cl atom was removed totally from the unit cell. The third table gives the adsorption heights for the Cl up configuration (h_{Cl_up}). The experimental unit cell with a 27° rotation of the molecules and *V5.3.3* (*sVDW* in the second and third table) with soft PAW potentials was used. For comparison, experimental XSW values (h_{XSW}) from Ref. [104] are shown. $h_{XSW,corr}$ shows the experimental XSW values minus one experimental Cu(111) layer spacing (2.08 Å) for Ga, C and N.

V5.3.3	$h_{Cl,1}$ [Å]	$h_{Cl,2}$ [Å]	h_{XSW} [Å]	$h_{XSW,corr}$ [Å]
Cl	1.94	-	1.88	1.88
Ga	2.27	2.27	4.21	2.13
C	2.80	2.79	4.44	2.36
N	2.87	2.86	4.71	2.63
H	2.75	2.74	-	-

sVDW	h_{Cldown} [Å]	$h_{Cl,1}$ [Å]	h_{XSW} [Å]	$h_{XSW,corr}$ [Å]
Cl	1.79	1.84	1.88	1.88
Ga	3.61	2.20	4.21	2.13
C	3.68	2.64	4.44	2.36
N	3.78	2.73	4.71	2.63
H	3.63	2.63	-	-

sVDW	h_{Clup}
Cl	5.33
Ga	3.12
C	2.57
N	2.60
H	2.61

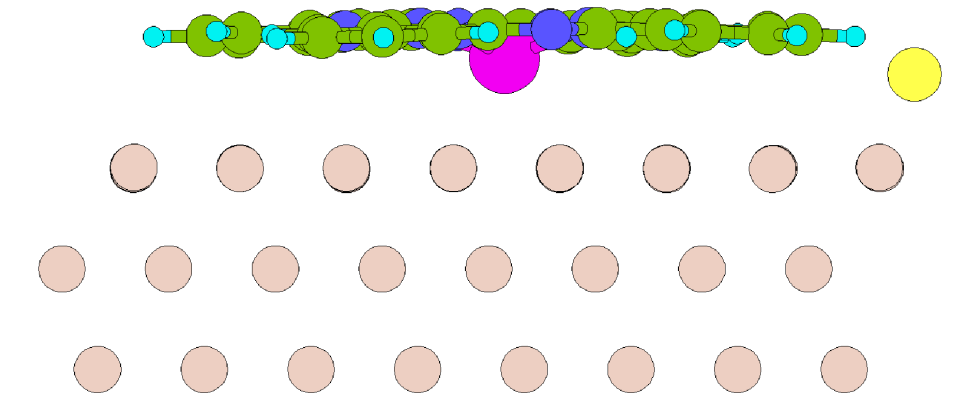

(a)

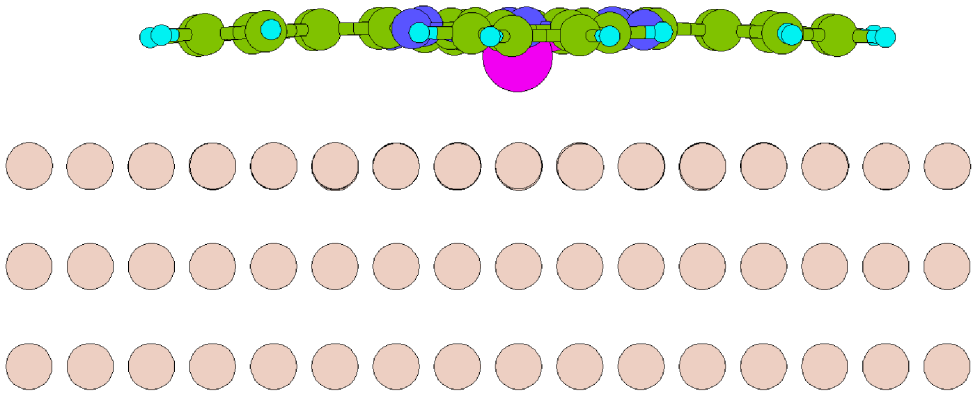

(b)

Figure 21: Adsorption geometries of the GaClPc molecule on Cu(111) with Cl removed from the GaPc molecule. (a) shows a configuration with Cl adsorbed to the Cu substrate aside from the molecule (*Cl,1*), while in (b) Cl is fully removed form the unit cell (*Cl,2*). Both simulations were done using *V5.3.3*, soft PAW potentials and the experimental unit cell.

Table 28: Total energies E_{tot} and work function modification $\Delta\phi$ of different configurations of GaClPc on Cu(111) using the experimental unit cell. Soft PAW potentials were used. The molecule is adsorbed in Cl up and Cl down configuration, *Cl,1* stands for the configuration with the Cl removed from the GaPc and adsorbed to the Cu substrate aside the molecule. The experimental work function modification is reported in Ref. [104].

experimenta UC, sVDW	E_{tot} [eV]	$\Delta\phi$ [eV]
Cl removed from molecule (Cl, 1)	-917.87	-0.57
Cl down	-915.59	-0.61
Cl up	-917.53	-0.27
experimental	-	-0.60

Table 29: Big unit cell: Computed average adsorption heights of the GaClPc molecule on Cu(111) with the Cl atom removed from the molecule and set on the surface at an edge of the unit cell. The big unit cell with a 27° rotation of the molecules and *V5.3.3* with *sVDW* and soft PAW potentials was used. For comparison, experimental XSW values (h_{XSW}) from Ref. [104] are shown. $h_{XSW,corr}$ shows the experimental XSW values minus one experimental Cu lattice spacing for Ga, C and N.

sVDW	$h_{Cl,1}$ [Å]	h_{XSW} [Å]	$h_{XSW,corr}$ [Å]
Cl	1.83	1.88	1.88
Ga	2.16	4.21	2.13
C	2.56	4.44	2.36
N	2.68	4.71	2.63
H	2.57	-	-

As the adsorption heights of molecules can strongly be influenced by the packing density and the remote adsorption of the Cl atom should increase the space requirement of the Cl-GaPc system, the simulation was repeated with the big unit cell, the Cl atom again remove from the molecule and set to an edge of the cell. This results again in a vertical distance of 4.1 Å between Cl and the closest molecular H atom, but larger spacing between the GaPc molecules. As in previous simulations, the initial heights were 3.0 Å and 2.2 Å for the molecule and the Cl atom, respectively.
The results of this simulations, again compared to original and corrected XSW values are presented in Tab. 29. The calculated values for Cl, Ga and N are within 0.05 Å of the corrected XSW values, while the average C height is 0.2 Å larger in the simulation than in experiment.
These difference between adsorption and experiment are within a range that is considered a good agreement. Further tests of the Cl-GaPc system in the big unit cell, mainly to compare the total energies of Cl up, Cl down and Cl removed are currently in progress. Also the problems when using *sVDW* to calculate GaPc on Cu(111) can hopefully be solved soon and the influence of totally removing the Cl atom on the adsorption heights should then be checked.
According to all results on GaClPc obtained so far, the most likely scenario seems to be a situation where Cl is removed from the GaPc molecule. The obtained adsorption heights as well as the calculated total energies support this hypothesis, and further tests will be done. This is not in contrast to the experimental results obtained by Gerlach et al. [104], as the only difference to the experimental results is a deviation in the adsorption heights of the molecular backbone of one Cu(111) layer spacing.
From the perspective simulations provide it might be difficult to determine what happens to the the dissociated Cl atom. As it is still present in the XSW measurements at a height which is typical for Cl adsorption on a Cu substrate [108] the situation with Cl adsorbed aside the GaPc molecule seems to be the most promising approach at this point.

Work function modification

Tab. 28 lists the work function modifications $\Delta\phi$ of the different configurations, Cl up, Cl down in the bent geometry and Cl removed and adsorbed aside the molecule. Cl up and Cl down exhibit strongly differing work function modifications (-0.27 eV and -0.61 eV, respectively). But curiously, $\Delta\phi$ only differs 0.04 eV between Cl down (-0.61 eV) and with Cl removed from the molecule (-0.57 eV), although the molecular dipoles of these two systems should differ significantly. When looking at the the shifts of the electrostatic potential induced by the free standing monolayers of the geometry optimised systems, the shift induced by the bent Cl down GaClPc monolayer amounts to -0.43 eV, while it amounts to -0.20 eV for the monolayer of the GaPc molecule with the Cl atoms placed somewhere else on the surface. But surprisingly, for both scenarios the value of $\Delta\phi$ is in good agreement with experiment which states a $\Delta\phi$ of 0.60 eV [104].

To explain this behaviour it is helpful to look at the DOS of the Cl up, Cl down and Cl removed systems (see Fig. 22). All configurations seem to exhibit Fermi level pinning. As shown in Ref. [21] the influence of the molecular dipole on $\Delta\phi$ in the Fermi-level pinning regime depends on the position of the molecular dipole relative to the immediate metal-molecule interface. Hofmann et al. investigates this by bending the CN-groups of a F4TCNQ molecule in different angles above and below the molecular backbone. The work function modification is strongly influenced by the molecular dipole as long as the CN-groups (and therefore the molecular dipole) are positioned above the molecular backbone, while this influence is very weak with CN-groups (and dipoles) below the backbone. So the determining factor for $\Delta\phi$ is the position of the molecular dipole relative to the region of charge rearrangements between molecule and substrate, because dipoles within this region are compensated by a change in the charge rearrangements.

The same situation seems to appear in the case of GaClPc and Cl-GaPc on Cu(111). While the molecular dipole influences $\Delta\phi$ in case of the Cl up configuration, where it lies outside the charge rearrangement region, it does not influence $\Delta\phi$ in all other cases, because there are no dipoles outside this region for Cl down as well as for Cl removed from the molecule. This results in very similar work function modifications in the two latter cases.

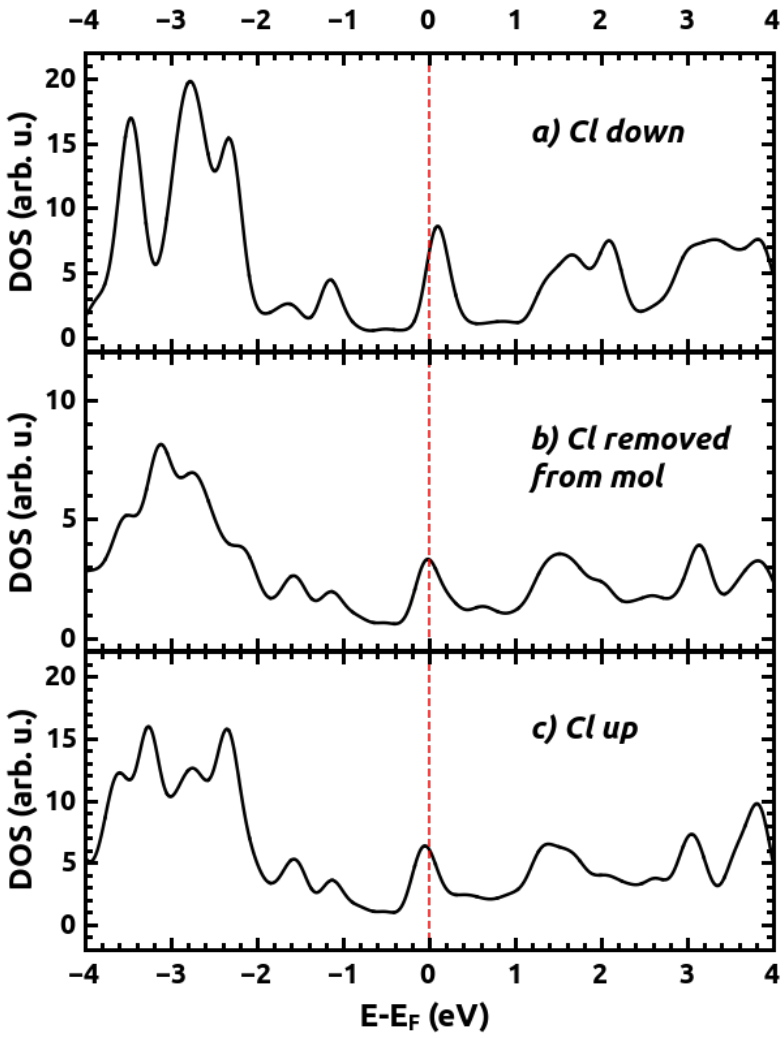

Figure 22: Molecular density of states of the GaClPc molecule on Cu(111) in the Cl down (a), Cl removed from the molecule and adsorbed aside the surface (b) and Cl up (c) configuration, calculated using the experimental unit cell with the molecule rotated 27°. *sVDW* and soft PAW potentials were applied.

6 Electronic properties of CuPc and ZnPc on Au(111) and Ag(111)

It has already been discussed that standard (semi-) local DFT calculations might not be suitable to describe the electronic properties of organic molecules (see Sec. 2.3.7). Especially in the case of metal phthalocyanines, hybrid functionals have been shown to be a more reasonable choice (e. g. CuPc, NiPc, CoPc, MnPc and FePc in the gas phase, see Ref. [36, 39, 40]).
The huge computational effort of hybrid functional calculations, even for the comparably "cheap", range-separated *HSE* functional, prohibit to perform the geometry optimisations of the investigated systems using *HSE*. For example, the performed single point calculations of CuPc on Au(111) took nearly 100 times longer with *HSE* than the equivalent *PBE* calculation. It has also been shown that hybrid functionals normally do not provide much better outcomes than *GGA* functionals when investigating geometries, as the one-electron self interaction error, which is minimized by the use of hybrid functionals, does not really affect total energies [38, 44]. For the example of metal phthalocyanine dimers it has been shown that performing vdW-corrected *PBE* geometry relaxation followed by a hybrid functional calculation of the relaxed system to investigate the electronic properties is a useful course of action [44]. This approach was adopted in this work to investigate the CuPc and ZnPc on Au(111) and Ag(111). All *HSE* calculations described in the following were carried out using the optimised geometries of these systems as described in the previous chapter.
Most of the results and discussions in this chapter are also presented in Ref. [14], with Yu Li Huang and the author of this work contributing as first authors. As mentioned earlier, all simulations of CuPc and ZnPc systems presented in this work are based on the experimental and theoretical work done by Yu Li Huang, who also did some investigations on the occurring charge rearrangements.
All *HSE* calculations were performed using VASP 5.3.3, applying *HSE06*. The time-parameter (*TIME*, see Ref. [72]) was set to 0.2 for all calculations presented in the following, which proved to be a reasonable choice for all systems investigated here, although the calculations of the metal substrates alone would have been doable and might have converged faster with a higher time-parameter.
Due to the necessity of performing spin-polarized calculations for CuPc, systems containing this molecule were much more complicated to simulate than the ones containing ZnPc. To speed up convergence a single point *PBE* calculation was performed for every system and the *WAVECAR* (and in some chases also the *CHGCAR*) file was read in for the *HSE* calculation. Some tests concerning the speed of *HSE* calculations dependent on the input were performed. Also the influence on the starting point on the final outcome of *HSE* simulations was tested. These results will be discussed in Sec. 6.2.

6.1 Results

6.1.1 Work function modification $\Delta\phi$

The work function modifications, $\Delta\phi$, of CuPc and ZnPc on Au(111) and Ag(111) systems have already been discussed in the previous chapter, determined using *PBE* functionals. When the *HSE* calculations were performed, $\Delta\phi$ was determined again. Tab. 30 (see also Ref. [14]) lists $\Delta\phi$ for both *PBE* and *HSE* calculations. Excellent agreement between experiment (determined from the secondary cutoff of UPS spectra [14]) and simulation is found. Also the agreement between generalized gradient (*PBE*) and hybrid functionals is very good, the maximal difference amounts to 0.06 eV for CuPc on Ag(111). A similar agreement of $\Delta\phi$ values between *GGA* and hybrid functionals has been reported by Hofmann et al. for molecular acceptors (PTCDA, F4TCNQ, PYTON) on Ag(111) [38].

Table 30: Work function modifications $\Delta\phi$ for CuPc and ZnPc on Au(111) and Ag(111) calculated with *PBE* ($\Delta\phi_{PBE}$) and *HSE06* ($\Delta\phi_{HSE}$), compared to experimental UPS values ($\Delta\phi_{UPS}$), measured at room temperature. Soft PAW potentials were used. The metal work functions, determined from the difference of the vacuum energy of the the uncovered side and the Fermi level of the metal slab, amount to 5.20 eV (*PBE*) / 5.16 eV (*HSE06*) for Au(111) and 4.48 eV (*PBE*) / 4.41 eV (*HSE06*) for Ag(111).

	CuPc			**ZnPc**		
	$\Delta\phi_{UPS}$ [eV]	$\Delta\phi_{PBE}$ [eV]	$\Delta\phi_{HSE}$ [eV]	$\Delta\phi_{UPS}$ [eV]	$\Delta\phi_{PBE}$ [eV]	$\Delta\phi_{HSE}$ [eV]
Au(111)	-0.69	-0.69	-0.65	-0.66	-0.61	-0.58
Ag(111)	-0.44	-0.44	-0.38	-0.43	-0.41	-0.38

The formation of $\Delta\phi$ due to the adsorption of a molecular monolayer on a metal is described by Eq. 4. It is caused i) by the molecular dipole (ΔE_{mol}) and ii) the charge rearrangements arising from the electronic interactions of molecule and substrate (ΔE_{bond}) [21]. In the case of CuPc and ZnPc on Au(111) and Ag(111) the first part contributes only minimally, as the molecules adsorb in a close-to-planar geometry (see Tab. 10). The shift in electrostatic potential induced by the free-standing monolayers in its final geometry (which are hypothetical, of course, but can easily be calculated) is below 0.07 eV for CuPc and below 0.10 eV for ZnPc. Therefore, $\Delta\phi$ has to be mostly caused by charge rearrangements due to the adsorption.
A part of the interface charge rearrangements is due to Pauli pushback, which has a strong effect on all metal-organic interfaces and causes a reduction of the work function [109]. The Pauli pushback is expected to have a larger influence on the Ag(111) than on the Au(111) systems, as it is stronger in case of smaller adsorption distances, which is the case for CuPc and ZnPc on Ag(111). But as the work function reduction is larger by about 0.2 eV for Au(111) than for Ag(111) in all cases, there must be

additional charge rearrangement effects, which differ for Au and Ag. These effects will be discussed in the following chapters.

6.1.2 Charge rearrangements due to molecular adsorption

The charge rearrangements at the metal-organic interface can be calculated from the VASP output. It is, therefore, necessary to separately calculate the system, the free-standing monolayer and the metallic slab. The charge rearrangements are calculated by subtracting the charge density of the system parts from the charge density of the whole system. There are different ways to present the results (see Sec. 2). A two-dimensional representations is possible via plane averaging or plane integration of the charge density at every z plane. The 2D charge rearrangements $\Delta\rho(z)$ of the CuPc on Au(111) and Ag(111) systems, determined by plane-integration of the charge rearrangements (Eq. 5) are shown in Fig. 23. The lower panels show the cumulative charge rearrangements (net charge transfer) $Q(z)$, which is derived by integrating $\Delta\rho(z)$ and gives the total amount of charge that is shifted from the left of the z plane to the right of that plane (see Sec. 2.2.4, Eq. 6) [23, 25, 26]).

Another possible depiction shows the charge rearrangements in a three-dimensional manner. For this purpose an isodensity representation is plotted, showing all surface areas with similar values of charge density difference. The plotted charge density is the difference in electron density of the whole system and the system parts, which means positive regions indicate electron accumulation while negative regions indicate electron depletion due to the adsorption process.
The 3D charge rearrangements for CuPc on Au(111) and Ag(111), as presented in Ref. [14], are shown in Fig. 24.

CuPc on Au(111)
The charge rearrangements of CuPc on Au(111) which are presented in Fig. 23 (a) show charge shifting from below the organic adsorbate towards the metal substrate. Pronounced electron depletion right underneath the molecule is clearly visible, as well as accumulation right above and partly inside the Au substrate. When looking at the net charge transfer (b) the electron transport from the right to the left (monolayer to substrate) amounts to about 0.45 electrons per molecule. For other metal-organic systems, like the well investigated PTCDA on Au(111) interface similar charge rearrangements due to adsorption are reported [69]. This form of the 2D charge transfer appears to be prototypical for the modification of the charge density caused by Pauli pushback. From the two visible minima of $\Delta\rho(z)$, one lies above and one below the organic monolayer, with respect to the substrate. The region of electron depletion on

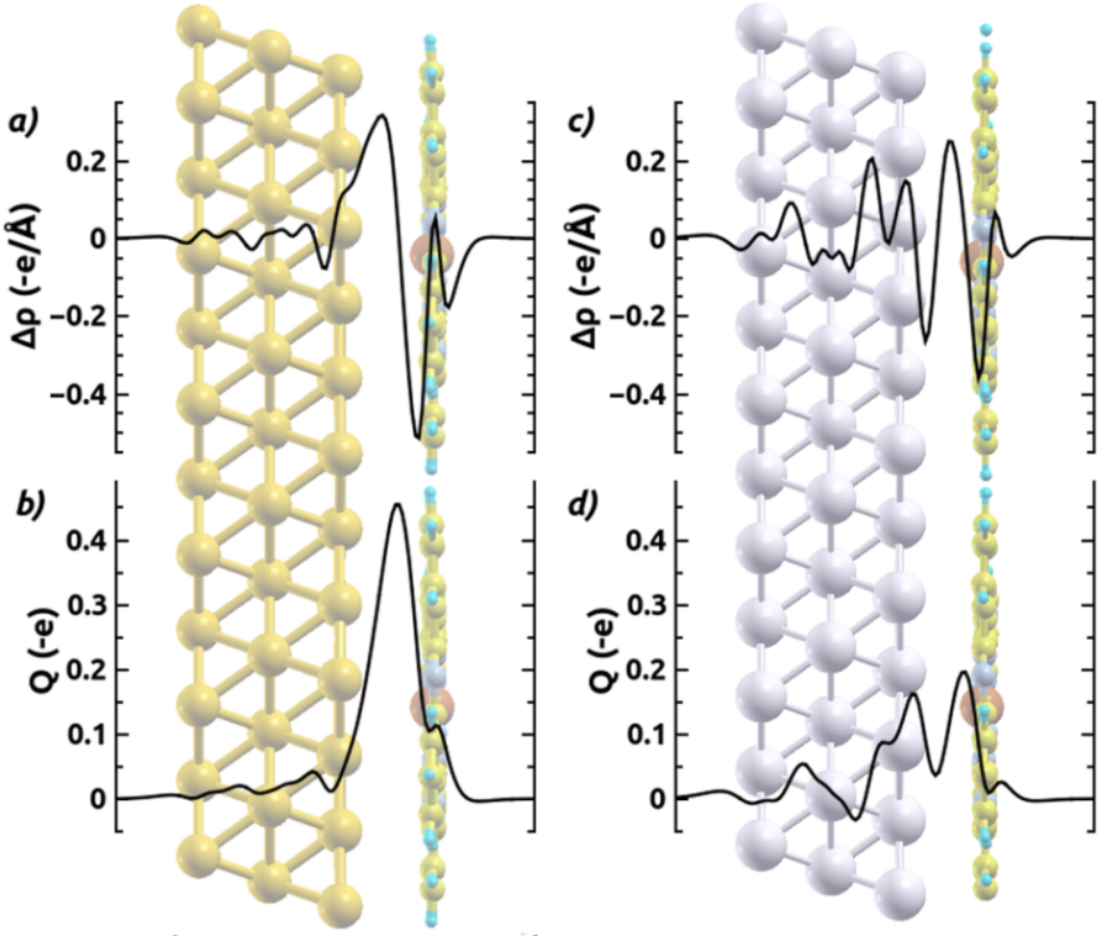

Figure 23: Plane-integrated charge rearrangements $\Delta\rho(z)$ and cumulative charge transfer $Q(z)$ caused by the adsorption of CuPc on Au(111) (left plots (a) and (b)) and on Ag(111) (right plots (c) and (d)). The upper plots show $\Delta\rho(z)$ in -e per Å (with -e denoting the negative elementary charge, the charge of one electron), where positive values correspond to an accumulation of electron density, while negative values correspond to electron depletion. The lower plots show $Q(z)$ in -e, which gives the number of electrons that have been transferred from the left to the right of the plane at position z. The results have been obtained using *HSE06*. Soft PAW potentials were used. This graph is taken from [14].

the substrate side of the monolayer is much "deeper" than the other one, which also supports the theory of this charge rearrangement being due to Pauli pushback, as the electron density "leaking" out of the metal decreases with the distance from the surface and, therefore, is higher below the monolayer [14].
The 3D charge rearrangements confirm the conclusions already made from the 2D picture. The electron depletion (blue) around the molecule is clearly visible in the region of the organic π system, while a small amount of electron accumulation around the

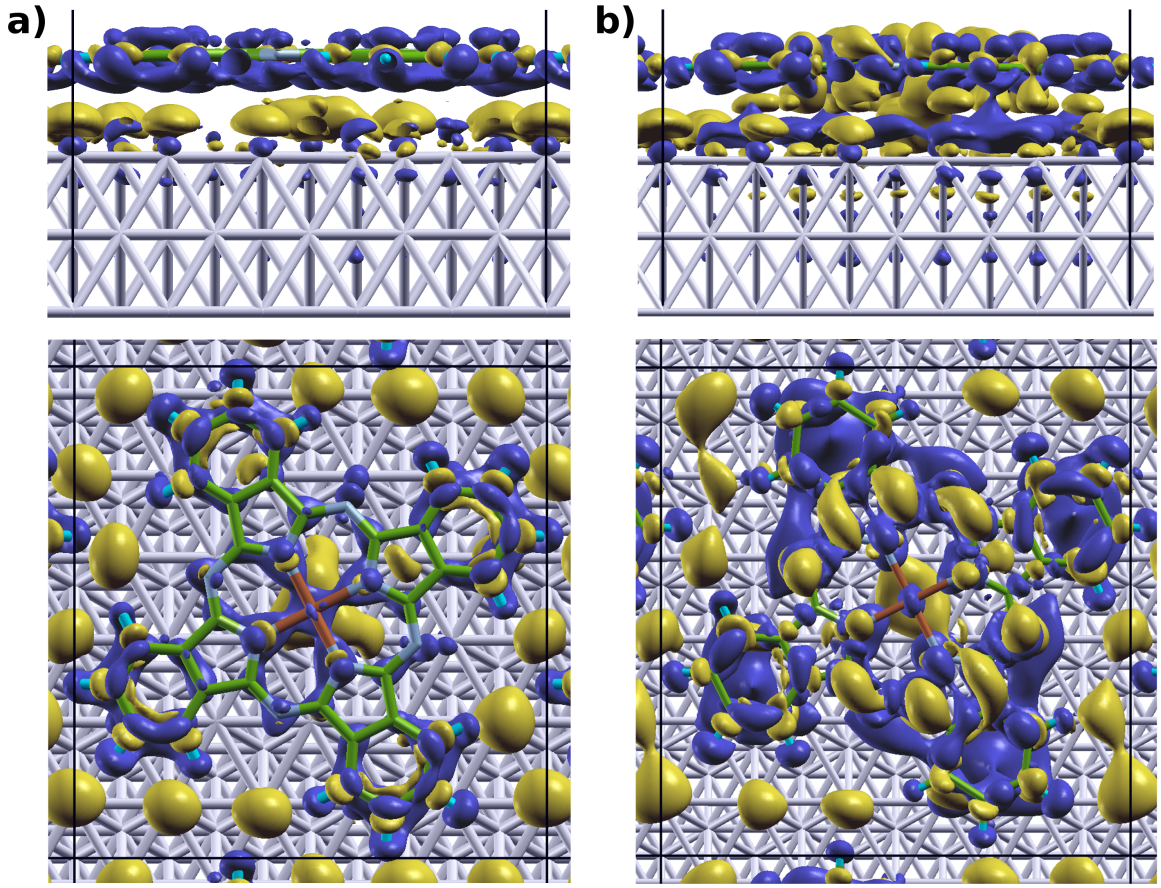

Figure 24: Isodensity plots of the charge rearrangements due to the adsorption of CuPc on Au(111) (a) and on Ag(111) (b). Blue regions show negative values of the electron density difference and therefore indicate electron depletion, while yellow regions show positive values and therefore electron accumulation. The results have been obtained using *HSE06* and the isovalue was set to 0.00315 e/Å. Soft PAW potentials were used. This graph is taken from [14].

molecules σ bonds also becomes apparent. The electron accumulation closer to the surface can be divided into two main regions. First, the region underneath the central Cu atom of the molecule and second the region around the molecule, in the uncovered areas of the Au(111) substrate. Interestingly, there is no pronounced accumulation underneath the outer organic rings.

CuPc on Ag(111)

In contrast to the situation on Au(111), where the charge rearrangements are dominated by the Pauli pushback effect which transfers electrons from the region below the monolayer toward the substrate, on Ag(111) there is an additional counteracting effect, transporting electrons in the opposite direction. The 3D charge arrangements

plot shows electron accumulation around the center of the molecule, in the inner part of the π systems and underneath the Cu atom. The corresponding electron depletion is visible right above the Ag(111) substrate, in the regions underneath the CuPc molecule. This indicates charge transfer from the substrate to the inner π orbitals of the molecule, caused by the bonding of molecule and substrate. The effects caused by Pauli pushback, being electron depletion around the π orbitals (more clearly visible around the outer ones in this case) and electron accumulation right above the Ag(111) surface in the uncovered regions are also visible.
In the 2D representation of the charge rearrangements it becomes visible that the net electron depletion at the level of the organic monolayer is weaker than on Au(111). Also the additional regions of depletion right above the Ag(111) substrate and the accumulation directly below the CuPc monolayer can be seen as an extra maximum and minimum in the plane-integrated charge density $\Delta\rho(z)$. As a result the net charge transfer $Q(z)$ exhibits a local minimum. In case of CuPc on Ag(111) the usefulness of the 3D charge rearrangement plot becomes obvious, as the plane integrated charge density $\Delta\rho(z)$ and the net charge transfer $Q(z)$ can here serve as additional visual aids and be used to look at total values of electron transfer as it gives more information on the quantities, but it does clearly not depict the whole complexity of the situation.
Obviously, the electron transfer to the molecule due to bonding is counteracting Pauli pushback, which is responsible for charge transfers from the region below the adsorbate toward the substrate. The resulting work function modification is still negative, which indicates that Pauli pushback is not totally compensated by the bonding [14].
It was shown for other systems that in contrast to the situation of CuPc on Ag(111), the bonding induced effect can be stronger than pushback for strong acceptor molecules like PTCDA or F4TCNQ and can cause a positive work function modification due to adsorption [27, 69].

6.1.3 Density of states obtained with *PBE* and *HSE* functionals

In addition to the charge rearrangements, the density of states obtained from the Kohn-Sham eigenvalue spectrum of the DFT calculation can be analysed.
The DOS for CuPc and ZnPc on Au(111) and Ag(111), calculated both with *PBE* and *HSE* functionals is shown in Fig. 25. Only the DOS projected on the adsorbate layer is shown. The *HSE* plot of CuPc on Au(111) does not clearly visualize the singly occupied state in the filled region, as it is superimposed with another state. To show its presence and position in more detail the difference between spin up and spin down DOS is plotted in Fig. 26.

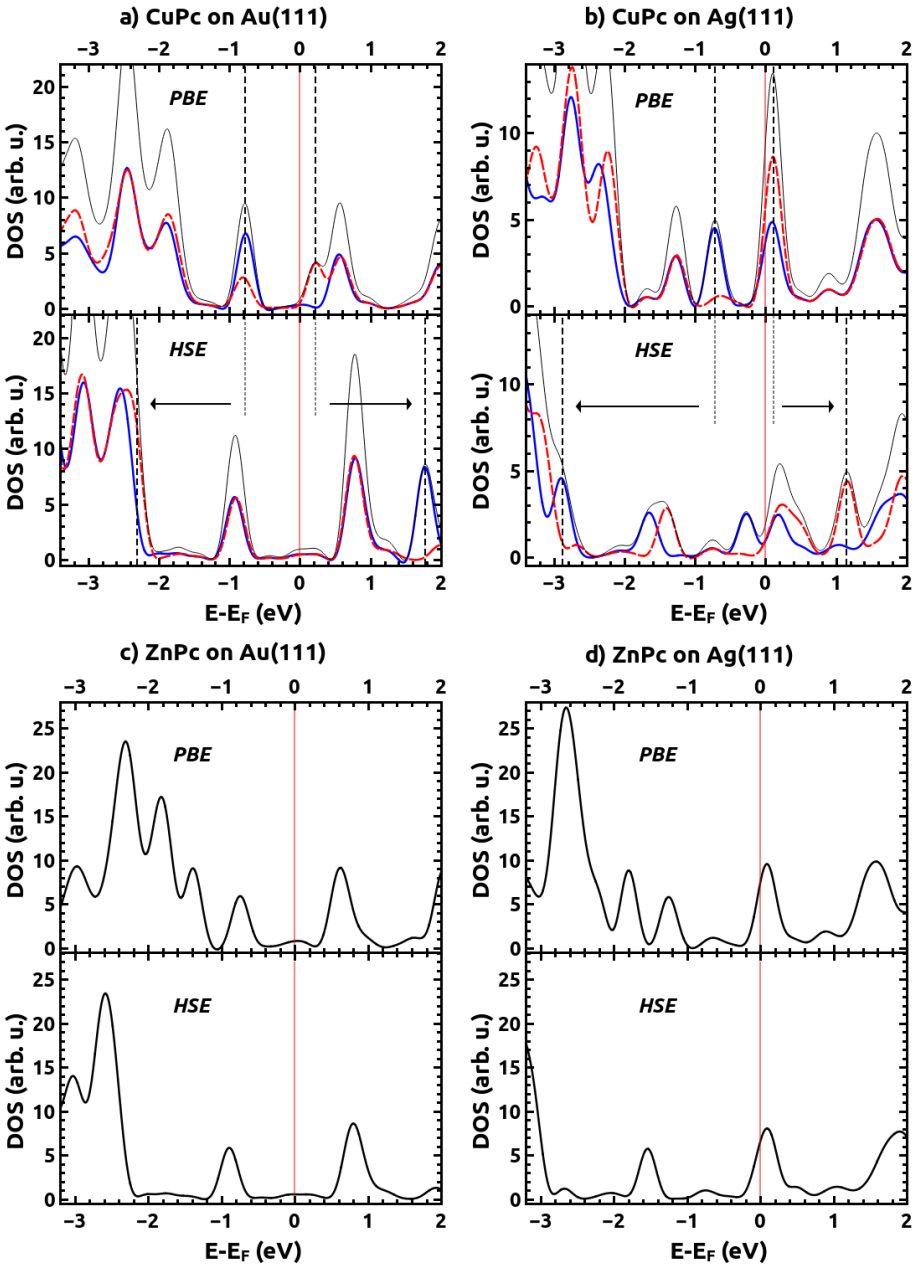

Figure 25: Computed density of states of CuPc on Au(111) (a) and Ag(111) (b) and ZnPc on Au(111) (c) and Ag(111) (d), showing the projected DOS of the molecular layer. Results obtained using *PBE* and *HSE06* functionals are shown. Soft PAW potentials were used. The total density of states for all systems is represented by a solid black line. For CuPc, due to its odd number of electrons, spin up and spin down densities have to be calculated separately and are drawn with solid blue for spin up and dashed red for spin down densities. To highlight the singly occupied orbitals they are marked with dashed vertical lines. For the *HSE* calculations the shift of these orbitals when going from *PBE* to *HSE* due to the inclusion of exact exchange is indicated by arrows. The vertical red line marks the Fermi energy. This graph is taken from [14].

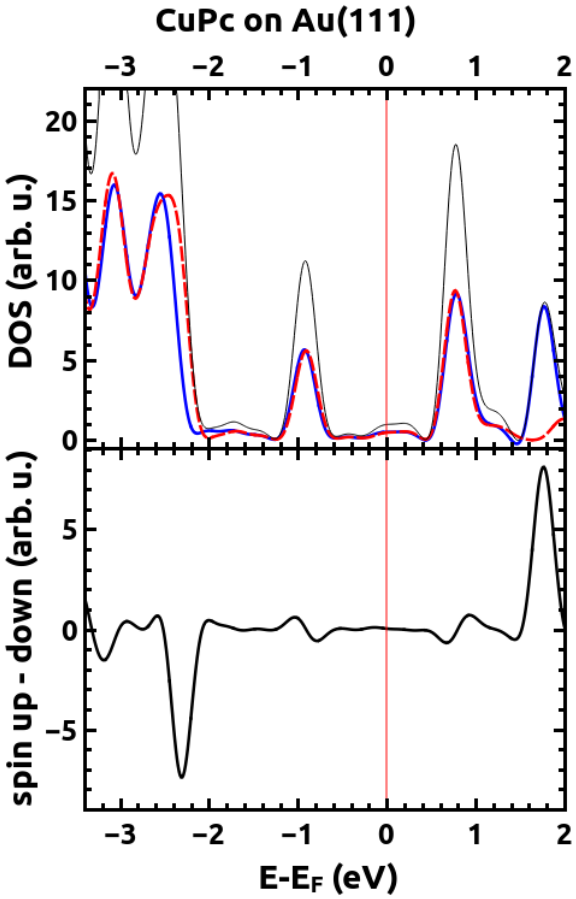

Figure 26: Computed density of states of the CuPc on Au(111) showing the projected DOS of the molecular layer. Results obtained using *PBE* and *HSE06* functionals are shown. Soft PAW potentials were used. In the upper panel, the total density of states is represented by a solid black line, the spin up density by a solid blue and spin down by dashed red line. To show the position of the singly occupied states more clearly the lower panel shows the spin up minus the spin down density. This graph is taken from [14].

So far, the adsorption heights of CuPc and ZnPc on Au(111) and Ag(111) as well as the charge rearrangements have indicated a stronger interaction of the molecule on Ag(111) than on Au(111) as a consequence of the higher work function of the latter. Further evidence becomes available with the DOS of these systems, where for the adsorption on Au(111) the Fermi energy lies within a gap, while for Ag(111) a partial filling of the former LUMO can be observed. The density of states of these systems was also measured with UPS and the results are presented in Ref. [14]. The peak positions of the UPS spectra and the DFT calculations associated with the HOMO are listed in Tab. 31. The UPS spectra determined by Yu Li Huang at Chiba University, Japan, are shown in Fig. 27. When comparing the HOMO positions for both calculation methods with the experimental results, surprisingly good agreement is found. Even more surprising is the better agreement of the *PBE* results with experiment, compared to the *HSE* results.

The direct comparison of Kohn-Sham eigenvalue spectra to experimental results is a problematic matter, as the KS eigenvalues can not always be directly considered as an approximation to ionization energies [8]. This problem of DFT is further complicated by the fact that the eigenvalue spectra can vary significantly for different exchange-correlation functionals [110].

Standard *GGA* functionals as well as hybrid functionals fail to predict the gap between the highest occupied and the lowest unoccupied molecular orbital correctly [35, 8]. This is due to different reasons. First, the used exchange-correlation potentials do not account for the derivative discontinuity of the chemical potential, and secondly the semi-local functionals fail to describe the $\frac{1}{r}$ asymptotic decay of the potential [35, 111]. The artificial narrowing of the gap is counteracted by another spurious effect, which shifts the HOMO in the opposite direction and enlarges the gap. This effect is due to the fact that semi-local functionals are not able to describe non-local correlations which would be necessary to account for screening effects of the metal electrons which modify the ionisation energies [112].

So it is assumed that the good agreement between experiment an calculation is due to the errors in DFT, which cause a narrowing of the gap, being counteracted by the effects widening the gap. A cancellation of these errors then leads to an accidentally good agreement of the calculated HOMO positions with the experimental ionisation energies [14].

Table 31: Energies of the peaks associated with the highest occupied molecular orbital E_H determined from UPS spectra [14] and the density of states calculated with *PBE* and *HSE*. Soft PAW potentials were used.

	CuPc			**ZnPc**		
	$E_{H,UPS}$ [eV]	$E_{H,PBE}$ [eV]	$E_{H,HSE}$ [eV]	$E_{H,UPS}$ [eV]	$E_{H,PBE}$ [eV]	$E_{H,HSE}$ [eV]
Au(111)	-0.81	-0.78	-0.91	-0.78	-0.74	-0.91
Ag(111)	-1.23	-1.28	-1.41 / -1.67	-1.20	-1.26	-1.54

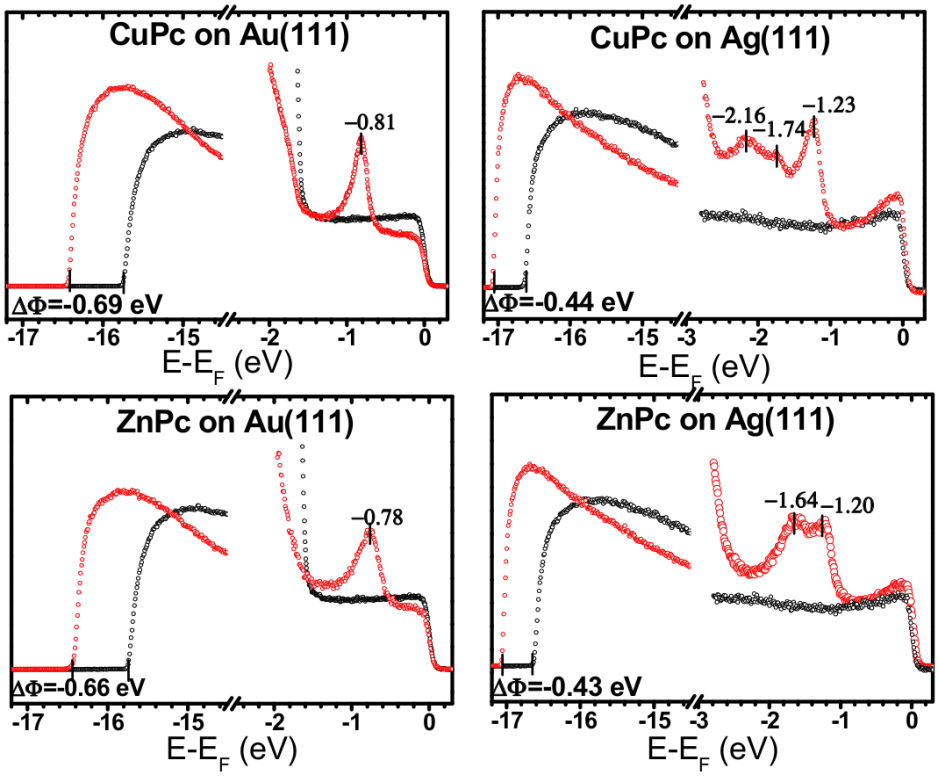

Figure 27: UPS spectra of CuPc on Au(111) (upper left) and CuPc on Ag(111) (upper right) ZnPc on Au(111) (lower left) and ZnPc on Ag(111) (lower right) monolayers. The black curve corresponds to the clean substrate, while the red curve represents the monolayer, annealed at 250°. For every situation, the secondary cutoff (left) as well as the valence region (right) is shown. These results were obtained by Yu Li Huang at Chiba University, Japan and is taken from Ref. [14].

The next interesting matter to discuss is the difference in the DOS of *PBE* and the *HSE06* calculations. The self interaction error (SIE) has already been discussed in Sec. 2.3.7. As mentioned there, its impact is different for differently localized orbitals; stronger localization means a higher SIE. Marom et al. [36] investigated gas-phase CuPc and found severe consequences of the SIE for this molecule (and other MPc systems [40, 39]). Especially the metal-centred orbitals are strongly influenced, and due to the odd number of electrons in the molecule, a spin-splitting of one of these orbitals into an occupied α-spin state and an unoccupied β-spin state occurs.
Looking at the upper (*PBE*) panels of Fig. 25, these singly occupied states can be easily identified. For CuPc on Au(111), there is an overlap of the singly occupied state with the molecular HOMO, which makes it difficult to compare the results to the non-spin-sensitive UPS data from Ref. [14]. For CuPc on Ag(111) the situation is more clear, as the singly occupied state is found at -0.68 eV, which is in the gap region according to UPS (see Tab. 31.)
The SIE can be mitigated by using *HSE* calculations, which should, therefore, be a vast improvement over *PBE* in case of the MPc systems. This was already shown for gas-phase molecules by Marom et al. [36, 40, 40]. Although the SIE can most likely not be extinguished completely just by using *HSE* [38], the orbital ordering should be improved, especially as the MPc systems exhibit strongly localized metal-centred orbitals and delocalized orbitals of the ligands lying close in energy.
The simulated DOSs obtained using the *HSE06* functionals are shown in the lower panels of Fig. 25. The shifting of states due to the change of functional is clearly visible for both CuPc systems. On Au(111), the singly occupied α-spin state is shifted from -0.93 eV in the *PBE* DOS to -2.31 eV in the *HSE* DOS. The unoccupied β-spin state is moved in the opposite direction, from 0.21 eV with *PBE* to 1.25 eV with *HSE*. For CuPc on Ag(111) the α-spin state shifts from -0.71 eV (*PBE*) to -2.89 eV (*HSE*) while the β-spin state shifts from 0.11 eV (*PBE*) to 1.34 eV (*HSE*). These shifts are indicated by the arrows in the *HSE*-DOS plots of CuPc (Fig. 25).
As there are no singly occupied states for the ZnPc molecules, the orbital shifts of the singly occupied states can not be identified so clearly just by analysing the DOS. But when looking at the energy window of -0.5 eV to -1.5 eV on Au(111), *PBE* predicts two peaks while in the *HSE* calculation only one peak is visible. The same thing happens for ZnPc on Ag(111). The energy window between -1.0 and -2.0 eV exhibits two peaks in *PBE* and only one peak in *HSE* calculations. To identify the orbitals associated with these peaks, the local density of states of the two highest peaks below the Fermi enery for *PBE* and of the highest peak below the Fermi energy for *HSE* was plotted, using the ZnPc on Ag(111) system. The results are shown in Fig. 28.
Local density of states plots are obtained by integrating the density of states over a certain energy window (0.1 eV in this work) and the local DOS is represented 3-dimensionally to see the localisation of the states in this specific energy window.
For ZnPc on Au(111), the LDOS was plotted for *PBE* at -0.74 eV and -1.39 eV. Fig. 28 shows that the state at -1.39 eV (a) is localized around the centring Zn atom, while the state at -0.74 eV (b) lies on the ligands. So the peak associated with the metal-centred

state at -1.39 eV should be shifted much more strongly when changing from the *PBE* to a *HSE* functional, as it is affected stronger by the self interaction error.
The *HSE* state at -0.90 eV (Fig. 28 (c)) is clearly a ligand state and can be associated with the ligand state of the *PBE* calculation. Therefore, the state is no longer visible at low energies in the *HSE* DOS, it has apparently been shifted to a much lower energy [14].

While the DOSs for both spin up and spin down states are more or less energetically aligned (with the exception of the spin-split states) for CuPc on Au(111), a misalignment of the is visible for CuPc on Ag(111) when *HSE* is used (see Fig. 25 (b)). Due to the stronger bonding of CuPc on Ag(111) there appears to be a charge transfer to the molecule, partly filling the LUMO band and occupying only one spin-channel, which causes the observed misalignment of the spin up and spin down DOSs [14]. The magnetic moment of the CuPc/Ag(111) system, which is about 1.00 μ_B for the isolated molecule increases to 1.96 μ_B upon adsorption on Ag(111). So the spin polarisation of the molecular monolayer is increased by charge transfer to the molecule.
After performing several different *HSE* simulations the value of the magnetic moment for this specific metal-organic interface turned out to depend on the the simulation parameters. This effect will be discussed in the following chapter (Sec. 6.2).
To analyse the charge transfer to the molecule in more detail the local density of states for a region of -0.3 eV up to the Fermi energy of the *HSE* calculation was plotted. This should help to identify the region to which charge is transferred when the filling of one spin-channel takes place. Fig. 29 shows the resulting LDOS plot. The inner part of the CuPc molecule is affected by the charge transfer, like it has already be seen when the 3D charge rearrangements of CuPc on Ag(111) were discussed. Only the electron density on the centring Cu atom itself is hardly affected by the charge transfer [14].
Experimental UPS results of the CuPc adsorption on Ag(111) also show two low intensity peaks at about -1.7 and -2.2 eV [14, 91], which can not be identified in the *HSE* DOS presented in this work. As these states are also not present in the gas-phase, as indicated by molecular calculations [36] and gas-phase UPS spectra [113], they are associated with the strong bonding of CuPc on Ag(111) [91]. Possibly the strong spin-misalignment of the *HSE* calculation of this system can be associated with these experimental features [14].

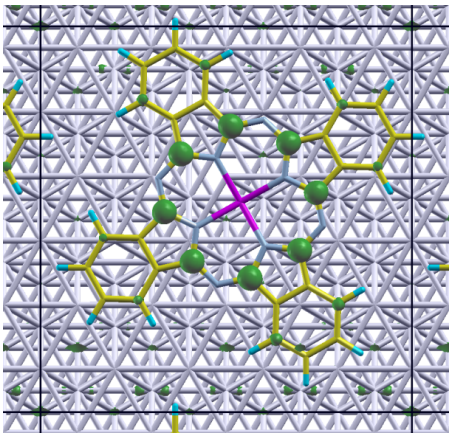

(a) *PBE*, E = -0.74 eV

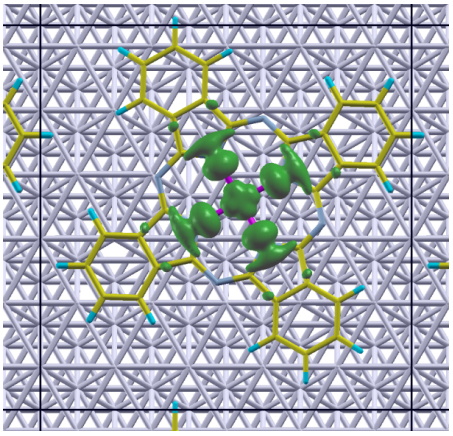

(b) *PBE*, E = -1.39 eV

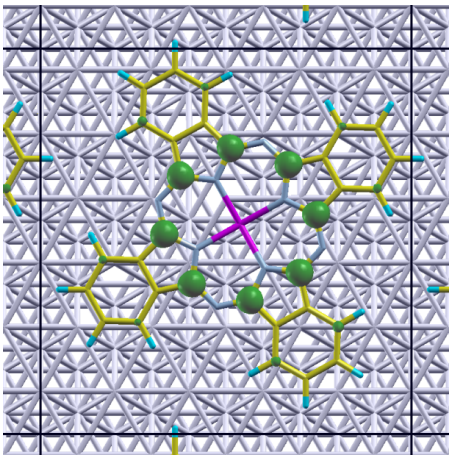

(c) *HSE*, E = -0.90 eV

Figure 28: Local density of states for ZnPc on Au(111) calculated from the *PBE* DOS (a), (b) and the *HSE* DOS (c). The DOS has been integrated over an energy window of 0.1 eV for the indicated energy values. Soft PAW potentials were used. This graph is taken from [14].

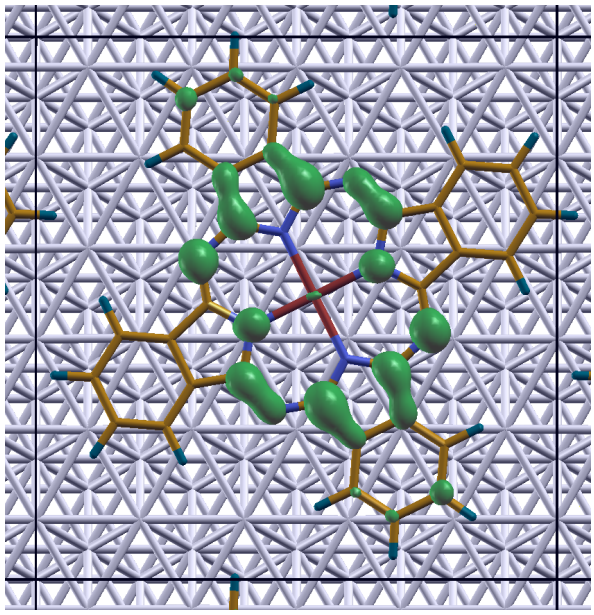

Figure 29: Local density of states of the CuPc molecule on Ag(111), calculated with *HSE* for an energy window from -0.3 eV up to the Fermi energy. The *HSE06* functional and soft PAW potentials were used. This graph is taken from [14].

6.2 General remarks and further tests using *HSE*

6.2.1 Computing time of *HSE* calculations

It has already been mentioned that *HSE* calculations are computationally much more costly than standard *GGA* calculations. Therefore, one is, of course, determined to perform these simulations in the computationally cheapest way possible.
First, all *HSE06* simulations presented so far were performed based on the input of the wave function file *WAVECAR* of a *PBE* simulation of the system to speed up convergence. It also turned out to decrease the calculation time, when the charge density file *CHGCAR* was read in. Curiously, the use of different sets of input parameters for the preliminary *PBE* calculations massively influenced the speed of the *HSE06* simulation. Tab. 32 lists three different *HSE06* simulations of CuPc on Ag(111). SIM1 gets the *WAVECAR* and *CHGCAR* from a *PBE* calculation where the *NUPDOWN* parameter (fixing the magnetic moment of the unit cell over the whole simulation) was set to *NUPDOWN=1.0*μ_B. SIM2 and SIM3 on the other hand get the *PBE* input files from a simulation without this predefinition. Both *PBE* calculations were performed spin-polarized. In the *HSE06* calculation itself, *NUPDOWN=1.0*μ_B was set for SIM1 and SIM2, but not for SIM3. Reading in the files from the *PBE* simulation without the *NUPDOWN* parameter speeded up the calculation significantly (66 instead of 208 CPU hours). On the other hand, not using *NUPDOWN* in the *HSE* calculation itself again decreased the computation speed (106 CPU hours).
The results of all these calculations were qualitatively and quantitatively similar, with the only exception being the magnetic moment, which was $\mu = 1.00\mu_B$ for SIM1 and SIM2, where *NUPDOWN* was set, and slightly differing for SIM3 ($\mu = 1.01\mu_B$), where this parameter was not set.

Table 32: Comparison of different sets of input parameters for the *HSE06* calculation of CuPc on Au(111). The line denoted *PBE* specifies the preliminary *PBE* calculation from which the *WAVECAR* and *CHGCAR* file were read in. The *NUPDOWN* parameter was either set to 1 or not set. The number of ionic steps is also given, as well as the total amount of CPU hours. Soft PAW potentials were used.

	SIM1	SIM2	SIM3
PBE	*NUPDOWN=1*	-	-
NUPDOWN	1	1	-
ionic steps	81	17	31
total CPU hours	208	66	106

To investigate the charge rearrangements it was also necessary to calculated the metal substrate and the free-standing monolayer separately. As it has already been mentioned, the *time* parameter of all presented *HSE06* calculations was set to *time = 0.2*. This is not the most suitable choice for metals, according to [72]. Therefore some test simulation the uncovered metal substrate with different *time* parameters (*time = 0.3* and *time = 0.4* as recommended in [72]) were performed. It turned out that increasing this parameter up to 0.4 speeds up the simulations and leads to no significant difference in the resulting total energy.

6.2.2 Convergence tests for the CuPc on Ag(111) system

The *HSE* simulation of CuPc on Ag(111) turned out to be cumbersome and time-consuming due to its spin-polarized nature and the strong coupling between adsorbate and substrate. Also the increased magnetic moment per unit cell was surprising at first, as the CuPc molecule holds only one unpaired electron, but a magnetic moment of 1.96 μ_B was found for the coupled system.
Therefore, it seemed useful to perform several simulations of CuPc on Ag(111), trying out different simulation inputs to i) find out the best possible input for quick convergence and ii) investigate the curious spin splitting and according increase in magnetic moment to make sure that it is not an artefact of a defective convergence process. The following results are presented in the supporting information of Ref. [14].
The CuPc on Ag(111) system was originally treated with a larger unit cell (as described in Sec. 5) containing 108 instead of 90 surface atoms. The tests presented in the following were performed using this unit cell, which explains the smaller magnetic moments of about 1.6 μ_B compared to about 1.9 μ_B in the previous chapter. The z-components of the magnetic moments μ_z and the total energies of the simulations are listed. The corresponding DOS plots are shown in Fig. 30.
The *HSE* calculation of the CuPc on Ag(111) system described in the previous chapter was performed with a similar starting configuration as the one denoted as 2^{nd} test here.

1^{st} test: A spin polarized *PBE* calculation of the system was performed. The resulting *WAVECAR* and *CHGCAR* were read in for the *HSE06* simulation.

- E_{tot}: -763.393 eV
- μ_z: 1.56 μ_B

2^{nd} test: A spin polarized *PBE* calculation of the system was performed. The resulting *WAVECAR* was read in for the *HSE06* simulation and the *MAGMOM*-tag was set. *MAGMOM* is used to set a starting configuration of the spin, so the initial magnetic moment of every atom of the system is predefine. In this case one unpaired spin was set onto the centring Cu atom.

- E_{tot}: -763.394 eV
- μ_z: 1.57 μ_B

3^{rd} test: A spin polarized *PBE* calculation of the system was performed. The resulting *WAVECAR* and *CHGCAR* were read in for the *HSE06* simulation, and the *NUPDOWN*-tag was set to fix the total magnetic moment to 1 μ_B during the whole simulation. As for all other simulations a magnetic moment deviating significantly from 1 was found this confinement might be problematic in the case of CuPc on Ag(111), while it should not cause and trouble for CuPc on Au(111), where the total magnetic moment is close to 1 μ_B anyway.

- E_{tot}: -763.390 eV
- μ_z: 1.00 μ_B

The orbital ordering obtained by *PBE* simulations is qualitatively different than the one obtained using *HSE*. Therefore, it is somehow problematic to read in *PBE* wave functions and charge densities for the *HSE* calculations as a starting point. This initial error might lead to slowed convergence or even the wrong outcome. To check whether such a problem arises, the following two test were performed without reading in wave functions and charge densities from previous *PBE* simulations.

4^{th} test: The *HSE* simulation was started without reading in files from previous *PBE* calculations. The *MAGMOM*-tag was set to put one unpaired spin upon the Cu atom.

- E_{tot}: -763.394 eV
- μ_z: 1.58 μ_B

5^{th} test: To accelerate convergence compared to the 4^{th} test, where no initialisation files were read in, a *CHGCAR* file was constructed. To avoid the incorrect orbital ordering of *PBE* simulations it was assembled of the charge density file of a *HSE* calculation of the free standing monolayer and a *PBE* calculation of the Ag substrate. In principle it would be possible to perform a VASP calculation to construct a wave function file from the charge density file [72] and read in those two files, but convergence turned

out to be faster without performing this extra calculation.

- E_{tot}: -763.393 eV
- μ_z: 1.57 μ_B

The comparison of the energies, magnetic moments and DOS plots of these tests show no qualitative differences, neither for orbital ordering nor for the total energies and the magnetic moments. Also the 3^{rd} test, where the magnetic moment was fixed to 1 μ_B exhibits similar results.
Also it becomes obvious that the input of *PBE* wave functions and charge density files does not jeopardize the outcome, but causes faster convergence of the *HSE* simulation. The fastest convergence was obtained by only reading in the wave functions and setting the *MAGMOM*-tag (2^{nd} test).
To make sure the observed spin splitting in the *HSE* simulations of CuPc on Ag(111) is not an artefact of the DFT calculations, the influence of different smearing parameters was investigated. The artificial broadening of the states was done using Methfessel-Paxton first order smearing, as explained in Sec. 3 [70]. The width of the smearing is defined in eV, using the *SIGMA* parameter. The CuPc on Ag(111) system with the smaller unit cell containing 90 substrate atom was calculated three times, with *SIMGA = 0.20*, *SIMGA = 0.10* and *SIMGA = 0.05*.
The resulting DOS plots are shown in Fig. 31. Decreasing the smearing width obviously leads to narrower, and higher peaks. Still there is no qualitative change in the obtained DOSs due to the decreased smearing. The asymmetric filling of the spin channels which leads to the shift between spin up and spin down DOS is clearly visible in all cases. Surprisingly however, the z-component of the magnetic moments per unit cell μ_z varies for different values of *SIMGA*. While μ_z amounts to 1.96 μ_B for *SIGMA = 0.20 eV*, it decreases to μ_z = 1.84 μ_B for *SIGMA = 0.10 eV* and to μ_z = 0.99 μ_B for *SIGMA = 0.05 eV*. The latter is especially surprising due to the fact that the asymmetric occupation is still clearly visible for *SIGMA = 0.05 eV*.
A closer analyse of the distribution of the magnetic moment on the atoms of the unit cell shows that the magnetisation of the adsorbate layer stays more or less constant for all different values of *SIGMA*. The sum of magnetic moments for all molecular atoms amounts to 1.70 μ_B for *SIGMA = 0.20 eV*, 1.69 μ_B for *SIGMA = 0.10 eV* and 1.68 μ_B for *SIGMA = 0.05 eV*. The decrease of the net μ_z is due to the appearance of small magnetic moments of the substrate Ag atoms at low values of *SIGMA*. This substrate magnetisation counteracts the the magnetic moment of the adsorbate layer.
It is not obvious what causes this effect and different explanations have been considered [14].
The substrate magnetization could be a spurious consequence of not increasing the k-point density when decreasing the smearing. This would in principle be necessary, but was omitted due to the computational effort being huge anyway. Increasing the k-point density would have made the calculations prohibitively costly, due to the large

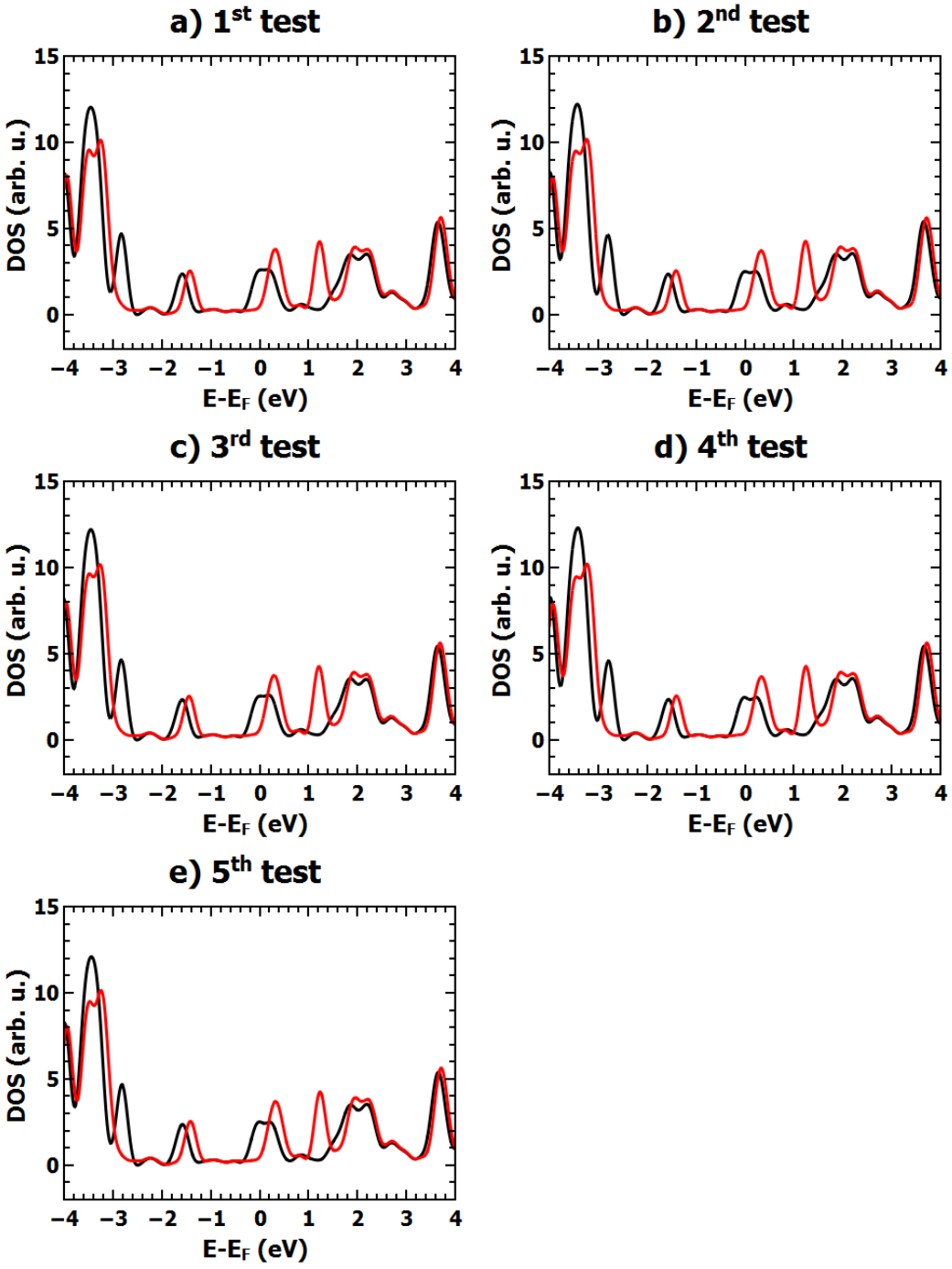

Figure 30: Density of states of CuPc on Ag(111), calculated with *HSE* and different starting configurations. Soft PAW potentials were used. Black and red lines represent spin up and spin down densities, respectively. This graph is taken from [14]

unit cells, the low smearing parameter and the use of *HSE* functions.
Another possible explanation would be that the magnetisation of the substrate is not a computational artefact but an actual effect that can not be described when the smearing parameter is too high. A similar effect has been seen for Au_{13} clusters, where a non-zero spin of the whole cluster could only be seen for energetically sharp states, obtained at low smearings [114].
The deeper investigation of the surface magnetisation effect goes beyond the scope of this work, as the important result in the context of the CuPc adsorption on Ag(111) is the charge transfer to the molecule with occupation of only one spin-channel, which has been proven to be independent of the choice of *SIGMA*.

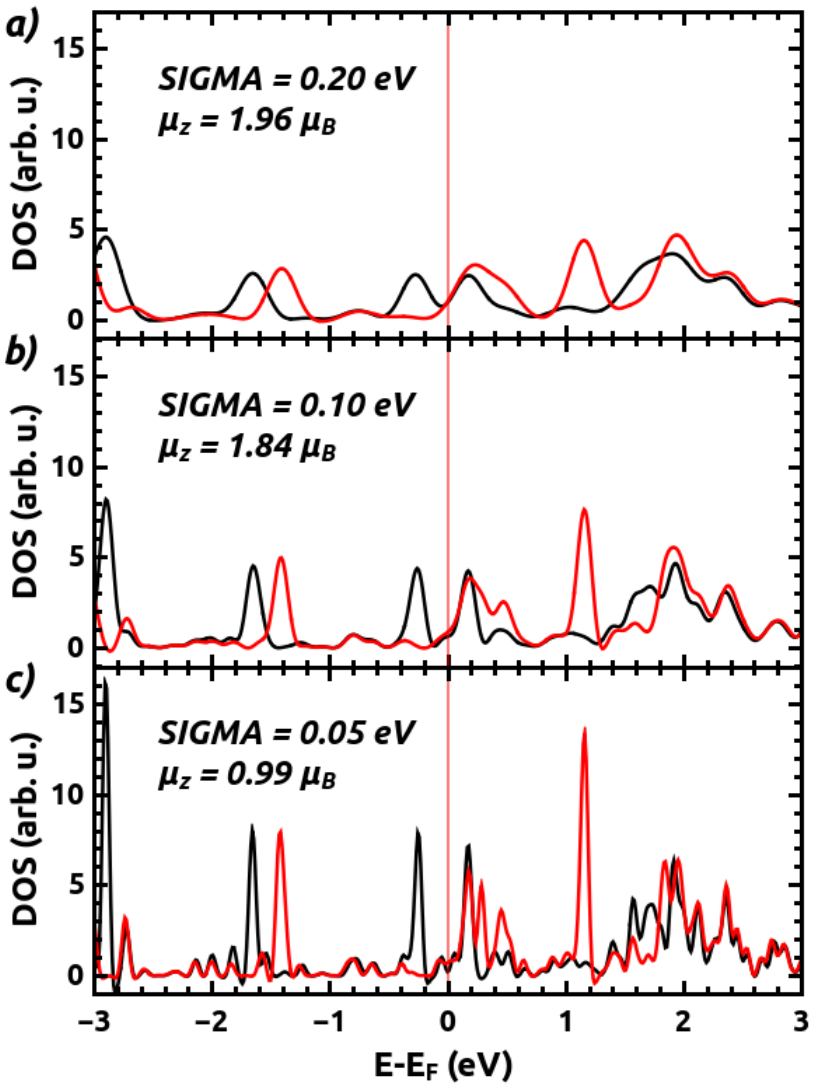

Figure 31: Density of states of CuPc on Ag(111), calculated with *HSE* and different smearing parameters *SIGMA*. Soft PAW potentials were used. Black and red lines represent spin up and spin down densities, respectively. The resulting z-components of the magnetic moments are listed for every simulation. This graph is taken from [14].

7 Conclusions and outlook

The vdW^{surf} approach proves to be a very useful and promising extension to standard semi-local DFT functionals like *PBE*. Not only does it allow the simulation of systems with physisorptive interactions, which is impossible in most cases without a vdW correction as the molecules just do not adsorb, it also provides adsorption heights in good agreement with experiments in most cases. Looking at the energies of different simulated systems, pure vdW binding energies of several eV for molecules of about 50 atoms were found, which is in contrast to the usually used notion describing vdW bonding as a "weak" interaction. Especially for metal-organic system, the use of this term should be questioned.

A weakness of the simulations as performed here is the necessity to know the surface unit cell of an investigated system. This is necessary, as it is not possible to optimize unit cell sizes and forms with reasonable computational effort. When the unit cells are not known, reaching good agreement between simulation and experimental results is massively complicated. This is due to the fact that the intermolecular interactions influence the adsorption heights, which can also be seen from simulation results obtained in this work. Wrong unit cell sizes, therefore, lead to inappropriate adsorption behaviour.

For some systems, different types of adsorption are possible. One example is the P2O molecule on Ag(111) where both "weak" and "strong" interaction can be observed in the simulations, depending on the starting configuration. As the systems might exhibit both possible outcomes, the input parameters have to be chosen very carefully and the outcomes need to be analysed deliberately, as minimal changes in the input can obviously cause different outcomes. The P2O / Ag(111) system, which will be investigated more closely in the future, appears to be a good example to demonstrate the discontinuous "switching" behaviour of a system between "weak" physisorptive and "strong" chemisorptive interactions.

The investigation of adsorption distances and total energies of the more complicated, non-planer GaClPc on Cu(111) system leads to a questioning of the interpretations of experimental results, presented in Ref. [104]. The simulations indicate a dissociation of the molecule to be the most favourable situation, as well as giving the best quantitative agreement with experimental data, in contrast to the original interpretation, with intact molecules adsorbing in a Cl down configuration. Further calculations will hopefully lead to a conclusive explanation of the complicated bonding process in this system.

After successfully determining adsorption geometries, DFT also provides the possibility of investigating the electronic properties of a system in more detail. At first, the work function modifications for the investigated systems were determined and good agreement with experimental results in virtually all cases was found.

A more detailed analysis of the interface electronic properties is presented for the CuPc and ZnPc on Au(111) and Ag(111) systems in Sec. 6. Hybrid-functional simu-

lations were performed to get a better picture of the molecular orbital ordering after adsorption. As it turns out, the density of states obtained by *PBE* and *HSE06* differ significantly. By comparing the positions of the HOMO to experimental UPS results, one finds that the hybrid functionals are better suited to describe the orbital ordering. This can most likely be attributed to the self-interaction error, which causes spurious orbital shifting in *PBE* calculations, but is mitigated in *HSE* calculations due to the added portion of exact exchange to the standard *PBE* functional. The orbital shift between *PBE* and *HSE*, which is stronger for strongly localized orbitals, can be shown explicitly by looking at the orbitals around the Fermi energy.
For the CuPc and ZnPc systems also the charge rearrangements due to molecular adsorption were analysed. As it turns out, the bonding of CuPc and ZnPc on Au(111) is weaker, with larger bonding distances and less charge transfer. For CuPc on Au(111), the observed charge transfer is mainly due to Pauli pushback, which means electrons are transported toward the surface. CuPc on Ag(111), on the other hand, also exhibits a counteracting effect of electrons being pulled toward the molecule as a consequence of the bonding effect.
Although *HSE* calculations turned out to be cumbersome and time-consuming, they are obviously a powerful tool to gain more insight into the bonding processes at the interface.

1 Appendix: van der Waals coefficients

Table 33: Molecular vdW coefficients C_6 $[\frac{J*nm^6}{mol}]$, α $[Bohr^3]$ and R_0 [Å].

Element	C_6 $[\frac{J*nm^6}{mol}]$	α $[Bohr^3]$	R_0 [Å]
H	0.375	4.5	1.64
Be	12.338	38	2.21
Mg	36.148	71	2.26
Ca	128.047	160	2.46
Sr	182.759	199	2.4
Ba	330.177	275	2.52
He	0.084	1.38	1.4
Ne	0.368	2.67	1.54
Ar	3.707	11.1	1.88
Kr	7.472	16.8	2.02
Xe	16.483	27.3	2.16
Rn	22.521	33.54	2.24
Li	79.964	164.2	2.2
Na	89.708	162.7	1.97
K	224.672	292.9	1.96
Rb	270.449	319.2	1.97
Cs	379.474	427.12	2
B	5.736	21	2.06
Al	30.441	60	2.29
Ga	28.711	60	2.22
In	40.763	70.22	2.24
Tl	41.362	69.92	2.07
C	2.687	12	1.9
Si	17.584	37	2.22
Ge	20.409	41	2.22
Sn	33.866	55.95	2.28
Pb	40.184	61.8	2.28
N	1.395	7.4	1.77
P	10.666	25	2.12
As	14.183	29	2.17
Sb	26.481	43.67	2.26
Bi	32.92	49.02	2.29
O	0.899	5.4	1.69
S	7.725	19.6	2.04
Se	12.107	25	2.14
Te	22.83	37.65	2.23
Po	30.609	45.013	2.17
F	0.549	3.8	1.61
Cl	5.454	15	1.96
Br	9.34	20	2.08

I	22.196	35	2.21
At	26.378	38.93	2.15
Sc	79.734	120	2.43
Ti	60.189	98	2.39
V	47.967	84	2.35
Cr	34.707	78	2.11
Mn	31.824	63	2.1
Fe	27.789	56	2.24
Co	23.522	50	2.21
Ni	21.504	48	2.02
Cu	14.586	42	1.99
Zn	16.373	40	2.13
Y	113.494	126.737	2.55
Zr	96.736	119.97	2.4
Nb	72.85	101.603	2.24
Mo	59.309	88.42	2.17
Tc	80.187	80.08	2.16
Ru	35.154	65.9	2.11
Rh	27.039	56.1	2.09
Pd	9.08	23.68	1.94
Ag	19.544	50.6	2.02
Cd	26.059	39.7	2.11
Hf	73.496	99.52	2.23
Ta	58.801	82.53	2.2
W	48.885	71.041	2.16
Re	40.945	63.04	2.13
Os	34.4	55.055	2.03
Ir	20.703	42.51	2.12
Pt	20.011	39.68	2.07
Au	17.18	36.5	2.04
Hg	22.6	33.9	2.11

Table 34: Substrate vdW coefficients C_6 $[\frac{J*nm^6}{mol}]$, α $[Bohr^3]$ and R_0 [Å].

Element	C_6 $[\frac{J*nm^6}{mol}]$	α $[Bohr^3]$	R_0 [Å]
Cu	3.397	10.88	1.27
Pd	5.881	13.9	1.619
Ag	7.034	15.4	1.36
Pt	6.918	14.5	1.481
Au	7.725	15.6	1.539

Bibliography

[1] J. P. Perdew, M. Ernzerhof, and K. Burke. Rationale for mixing exact exchange with density functional approximations. *The Journal of Chemical Physics*, 105:9982, 1996.

[2] J. Heyd, G. E. Scuseria, and M. Ernzerhof. Hybrid functionals based on a screened Coulomb potential. *The Journal of Chemical Physics*, 118:8207, 2003.

[3] A. Tkatchenko and M. Scheffler. Accurate Molecular Van Der Waals Interactions from Ground-State Electron Density and Free-Atom Reference Data. *Physical Review Letters*, 102:073005, 2009.

[4] V. G. Ruiz, W. Liu, E. Zojer, M. Scheffler, , and A. Tkatchenko. Density-Functional Theory with Screened van der Waals Interactions for the Modeling of Hybrid Inorganic-Organic Systems. *Physical Review Letters*, 108:146103, 2012.

[5] W. A. Saidi, V. K. Voorad, and K. D. Jordan. An Assessment of the vdW-TS Method for Extended Systems. *Journal of Chemical Theory and Computation*, 8:1503–1513, 2012.

[6] G. Hadziioannou and P.F. van Hutten, editors. *Front Matter, in Semiconducting Polymers: Chemistry, Physics and Engineering.* Wiley-VCH Verlag GmbH und Co. KGaA, 2005.

[7] H. Klauk, editor. *Front Matter, in Organic Electronics: Materials, Manufacturing and Applications.* Wiley-VCH Verlag GmbH und Co. KGaA, 2006.

[8] Richard M. Martin. *Electronic Structure: Basic Theory and Practical Methods.* Cambridge University Press, 2004.

[9] J. Klimed and A. Michaelides. Perspective: Advances and challenges in treating van der Waals dispersion forces in density functional theory. *The Journal of Chemical Physics*, 137:120901, 2012.

[10] D. A. Egger, V. G. Ruiz, W. A. Saidi, T. Bucko, A. Tkatchenko, and E. Zojer. Understanding Structure and Bonding of Multilayered Metal-Organic Nanostructures. *The Journal of Physical Chemistry C*, 117:3055–3061, 2013.

[11] G. Kresse and J. Furthmüller. Eficient iterative schemes for ab initio total-energy calculations using a plane-wave basis set. *Physical Review B*, 54:11169, 1996.

[12] T. Bucko, J. Hafner, and J. G. Angyan. Geometry optimization of periodic systems using internal coordinates. *The Journal of Chemical Physics*, 122:124508, 2005.

[13] S.K.M. Henzea, O. Bauerb, T.-L. Leec, M. Sokolowskib, and F.S. Tautz. Vertical bonding distances of PTCDA on Au(1 1 1) and Ag(1 1 1): Relation to the bonding type. *Surfacer Science*, 601:1566–1573, 2007.

[14] Yu Li Huang, Elisabeth Wruss, David A. Egger, Satoshi Kera, Nobuo Ueno, Wissam A. Saidi, Tomas Bucko, Andrew T. S. Wee, , and Egbert Zojer and. Understanding the adsorption of CuPc and ZnPc on noble metal surfaces by combining quantum-mechanical modelling and photoelectron spectroscopy. *Molecules*, 19(3):2969–2992, 2014.

[15] V. A. Parsegian. *Van Der Waals Forces: A Handbook for Biologists, Chemists, Engineers, and Physicists.* Cambridge University Press, first edition edition, 2006.

[16] H. Lueth. *Solid Surfaces, Interfaces and Thin Films.* Springer-Verlag, 4 edition, 2001.

[17] R. Gross and A. Marx. *Festkörperphysik.* Oldenbourg Verlag, first edition edition, 2012.

[18] N. Koch, N. Ueno, and A.T.S. Wee. *The Molecule-Metal Interface.* Wiley-Vch Verlag GmbH und Co. KGaA, first edition edition, 2013.

[19] S. Braun, W. R. Salaneck, and M. Fahlman. Energy-Level Alignment at Organic/Metal and Organic/Organic Interfaces. *Advanced Materials*, 21:1450–1472, 2009.

[20] E. Zaremba and W. Kohn. Van der Waals interaction between an atom and a solid surface. *Physical Review B*, 13:2270, 1976.

[21] O. T. Hofmann, D. A. Egger, and E. Zojer. Work-Function Modification beyond Pinning: When Do Molecular Dipoles Count? *Nano Letters*, 10:4369–4374, 2010.

[22] H. Vazquez, Y. J. Dappe, J. Ortega, and F. Flores. Energy level alignment at metal/organic semiconductor interfaces: "Pillow" effect, induced density of interface states, and charge neutrality level. *The Journal of Chemical Physic*, 126:144703, 2007.

[23] L. Romaner, D. Nabok, P. Puschnig, E. Zojer, and C. Ambrosch-Draxl. Theoretical study of PTCDA adsorbed on the coinage metal surfaces, Ag(111), Au(111) and Cu(111). *New Journal of Physics*, 11:053010, 2009.

[24] H. Ishii, K. Sugiyama, E. Ito, and K. Seki. Energy Level Alignment and Interfacial Electronic Structures at Organic/Metal and Organic/Organic Interfaces. *Advanced Materials*, 11:605–625, 1999.

[25] L. Romaner, G. Heimel, and E. Zojer. Electronic structure of thiol-bonded self-assembled monolayers: Impact of coverage. *Physical Review B*, 77:045113, 2008.

[26] R. Stadler and K. W. Jacobsen. Fermi level alignment in molecular nanojunctions and its relation to charge transfer. *Physical Review B*, 74:161405, 2006.

[27] G. Rangger, O. Hofmann, L. Romaner, G. Heimel, B. Bröker, R. Johnson R.-P. Blum, N. Koch, and E. Zojer. F4TCNQ on Cu, Ag, and Au as prototypical example for a strong organic acceptor on coinage metals. *Physical Review B*, 79:165306, 2009.

[28] P. Hohenberg and W. Kohn. Inhomogeneous Electron Gas. *Physical Review*, 136:864, 1964.

[29] W. Kohn and L. J. Sham. Self-Consistent Equations Including Exchange and Correlation Effects. *Physical Review*, 140:A1133, 1965.

[30] M. Levy, J. P. Perdew, and V. Sahni. Exact differential equation for the density and ionization energy of a many-particle system. *Physical Review A*, 30:2745, 1984.

[31] Frank Jensen. *Introduction to Computational Chemistry.* John Wiley and Sons Ltd., second edition edition, 2007.

[32] P. E. Blöchl. Projector augmented-wave method. *Physical Review B*, 50:17953, 1994.

[33] K. Burke. Perspektive on density functional theory. *The Jounal of Chemical Physics*, 136:150901, 2012.

[34] A. J. Cohen, P. Mori-Sanchez, and W. Yang. Insights into Current Limitations of Density Functional Theory. *Science*, 321:792–794, 2008.

[35] S. Kümmel and L. Kronik. Orbital-dependent density functionals: Theory and applications. *Reviews of Modern Physics*, 80:3–60, 2008.

[36] N. Marom, O. Hod, G. E. Scuseria, and L. Kronik. Electronic structure of copper phthalocyanine: A comparative density functional theory study. *The Journal of Chemical Physics*, 128:164107, 2008.

[37] J. P. Perdew, G. Parr, M. Levy, and J. L. Balduz. Density-Functional Theory for Fractional Particle Number: Derivative Discontinuities of the Energy. *Physical Review letters*, 49:1691, 1982.

[38] O. T. Hofmann, V. Atalla, N. Moll, P. Rinke, and M. Scheffler. Interface dipoles of organic molecules on Ag(111) in hybrid density-functional theory. *New Journal of Physics*, 15:123028, 2013.

[39] N. Marom and L. Kronik. Density functional theory of transition metal phthalocyanines, II: electronic structure of MnPc and FePc-symmetry and symmetry breaking. *Applied Physics A*, 95:165–172, 2009.

[40] N. Marom and L. Kronik. Density functional theory of transition metal phthalocyanines, I: electronic structure of NiPc and CoPc-self-interaction effects. *Applied Physics A*, 95:159–163, 2009.

[41] N. Marom, X. Ren, J. E. Moussa, J. R. Chelikowsky, and L. Kronik. Electronic structure of copper phthalocyanine from G 0 W0 calculation. *Physical Review B*, 84:195143, 2011.

[42] M. Ernzerhof and G. E. Scuseria. Assessment of the Perdew-Burke-Ernzerhof exchange-correlation functional. *The Journal of Chemical Physics*, 110:5029, 1999.

[43] A.D. Becke. Density-functional thermochemistry. III. The role of exact exchange. *The Journal of Chemical Physics*, 98:5648–5652, 1993.

[44] Noa Marom, Alexandre Tkatchenko, Matthias Scheffler, and Leeor Kronik. Describing Both Dispersion Interactions and Electronic Structure Using Density Functional Theory: The Case of Metal-Phthalocyanine Dimers. *Journal of Chemical Theory and Computation*, 6:81–90, 2010.

[45] G. Heimel, S. Duhm, I. Salzmann, A. Gerlach, A. Strozecka, J. Niederhausen, C. Bürker, T. Hosokai, I. Fernandez-Torrente, G. Schulze, S. Winkler, A. Wilke, R. Schlesinger, J. Frisch, B. Bröker, A. Vollmer, B. Detlefs, J. Pflaum, S. Kera, K. J. Franke, N. Ueno, J. I. Pascual, F. Schreiber, and N. Koch. Charged and metallic molecular monolayers through surface-induced aromatic stabilization. *Nature Chemistry*, 5:187–194, 2013.

[46] M.-T. Nguyen, C. A. Pignedoli, M. Treier, R. Fasel, and D. Passerone. The role of van der Waals interactions in surface-supported supramolecular networks. *Physical Chemistry Chemical Physics*, 12:992–999, 2010.

[47] M. Rohlfing, R. Temirov, and F. S. Tautz. Adsorption structure and scanning tunneling data of a prototype organic-inorganic interface: PTCDA on Ag(111). *Physical Review B*, 76:115421, 2007.

[48] A. Tkatchenko, L. Romaner, O. T. Hofmann, E. Zojer, C. Ambrosch-Draxl, and M. Scheffler. Van der Waals Interactions Between Organic Adsorbates and at Organic/Inorganic Interfaces. *MRS Bulletin*, 35:435–442, 2010.

[49] Q. Wu and W. Yang. Empirical correction to density functional theory for van der Waals interactions. *The Journal of Chemical Physics*, 116:515, 2002.

[50] S. Grimme. Accurate description of van der Waals complexes by density functional theory including empirical corrections. *Journal of Computational Chemistry*, 25:1463–1473, 2004.

[51] S. Grimme. Semiempirical GGA-type density functional constructed with a long-range dispersion correction. *Journal of Computational Chemistry*, 27:1787–1799, 2006.

[52] S. Grimme, J. Antony, S. Ehrlich, and H. Krieg. A consistent and accurate ab initio parametrization of density functional dispersion correction (DFT-D) for the 94 elements H-Pu. *The Journal of Chemical Physics*, 132:154104, 2010.

[53] A. D. Becke and E. R. Johnson. A density-functional model of the dispersion interaction. *The Journal of Chemical Physics*, 123:154101, 2005.

[54] L. A. Burns, A. Vazquez-Mayagoitia, B. G. Sumpter, and C. D. Sherrill. Density-functional approaches to noncovalent interactions: A comparison of dispersion corrections (DFT-D), exchange-hole dipole moment (XDM) theory, and specialized functionals. *The Journal of Chemical Physics*, 134:084107, 2011.

[55] M. Dion, H. Rydberg, E. Schröder, D. C. Langreth, and B. I. Lundqvist. Van der Waals Density Functional for General Geometries. *Physical Review Letters*, 92:246401, 2004.

[56] O. A. v. Lilienfeld and A. Tkatchenko. Two- and three-body interatomic dispersion energy contributions to binding in molecules and solids. *The Journal of Chemical Physics*, 132:234109, 2010.

[57] M. W. Cole, D. Velegol, H.-Y. Kim, and A. A. Lucas. Nanoscale van der Waals interactions. *Molecular Simulation*, 35:849–866, 2009.

[58] F. Furche and T. Van Voorhis. Fluctuation-dissipation theorem density-functional theory. *The Journal of Chemical Physics*, 122:164106, 2005.

[59] F. Furche. Molecular tests of the random phase approximation to the exchange-correlation energy functional. *Physical Review B*, 64:195120, 2001.

[60] J. F. Dobson, A. White, and A. Rubio. Asymptotics of the Dispersion Interaction: Analytic Benchmarks for van der Waals Energy Functionals. *Physical Review Letters*, 96:073201, 2006.

[61] J. Toulouse, W. Zhu, J. G. Angyan, and A. Savin. Range-separated density-functional theory with the random-phase approximation: Detailed formalism and illustrative applications. *Physical Review A*, 82:032502, 2010.

[62] T. Brinck, J. S. Murray, and P. Politzer. Polarizability and volume. *The Journal of Chemical Physics*, 98:4305, 1993.

[63] F. L. Hirshfeld. Bonded-atom fragments for describing molecular charge densities. *Theoretica chimica acta*, 44:129–138, 1977.

[64] E. R. Johnson and A. D. Becke. A post-Hartree-Fock model of intermolecular interactions. *The Journal of Chemical Physics*, 123:024101, 2005.

[65] A. Olasz, K. Vanommeslaeghe, A. Krishtal, T. Veszpremi, C. Van Alsenoy, and P. Geerlings. The use of atomic intrinsic polarizabilities in the evaluation of the dispersion energy. *The Journal of Chemical Physics*, 127:224105, 2007.

[66] I.G. Kaplan. *Intermolecular Interactions: Physical Picture, Computational Methods and Model Potentials.* John Wiley and Sons, 2006.

[67] E. M. Lifshitz. The theory of molecular attractive forces between solids. *Soviet Physics JETP*, 2:73, 1956.

[68] S. H. Patil, K. T. Tang, and J. P. Toennies. Damping functions for the pairwise sum model of the atom-surface potential. *The Journal of Chemical Physics*, 116:8118, 2002.

[69] L. Romaner, D. Nabok, P. Puschnig, E. Zojer, and C. Ambrosch-Draxl. Theoretical study of PTCDA adsorbed on the coinage metal surfaces, Ag(111), Au(111) and Cu(111). *New Journal of Physics*, 11:053010, 2009.

[70] M. Methfessel and A. Paxton. High-precision sampling for Brillouin-zone integration in metals. *Physical Review B*, 40:3616–3621, 1989.

[71] A. Kokalj. Computer graphics and graphical user interfaces as tools in simulations of matter at the atomic scale. *Computational Materials Science*, 28:155–168, 2003.

[72] J. Furthmueller G. Kresse, M. Marsman. *VASP the GUIDE.* Computational Physics, Faculty of Physics, Universitaet Wien, 2012.

[73] H. J Monkhorst and J. D. Pack. Special points for Brillouin-zone integrations. *Physical Review B*, 13:5188–5192, 1976.

[74] O. Farkas and H. B. Schlegel. Methods for optimizing large molecules. Part III. An improved algorithm for geometry optimization using direct inversion in the iterative subspace (GDIIS). *Physical Chemistry Chemical Physics*, 4:11–15, 2002.

[75] P. Csaszar and P. Pulay. Geometry optimization by direct inversion in the iterative subspace. *Journal of Molecular Structure*, 114:31–34, 1984.

[76] G. Kresse and J. Furthmüller. Efficient iterative schemes for ab initio total-energy calculations using a plane-wave basis set. *Physical Review B*, 54:11169–11186, 1996.

[77] P. Pulay. Convergence acceleration of iterative sequences. The case of SCF iteration. *Chemical Physics Letters*, 73:393–398, 198.

[78] J. Baker and P. Pulay. Geometry optimization of atomic microclusters using inverse power distance coordinates. *The Journal of Chemical Physics*, 105:11100, 1996.

[79] Lorenz Romaner. *Modelling of organic semiconductors and their interaction wiht metallic surfaxces.* PhD thesis, Graz University of Technology, 2007.

[80] G. Heimel, L. Romaner, J. L. Bredas, and E. Zojer. Interface energetic and level alignment at covalent metal-molecule junctions: pi-conjugated thiols on gold. *Physical Review Letters*, 96:198606, 2006.

[81] Klaus Hermann. *Crystallography and Surface Structure: An Introduction for Surface Scientists and Nanoscientists.* WILEY-VCH Verlag GmbH und Co. KGaA, Weinheim, February 2011.

[82] Octave community. GNU Octave 3.8, 2014.

[83] T. Bucko, J. Hafner S. Lebegue, and J. G. Angyan. Tkatchenko-Scheffler van der Waals correction method with and without self-consistent screening applied to solids. *Physical Review B*, 87:06411, 2013.

[84] S. Duhm, A. Gerlach, I. Salzmann, B. BrÃűker, R.L. Johnson, F. Schreiber, and N. Koch. PTCDA on Au(1 1 1), Ag(1 1 1) and Cu(1 1 1): Correlation of interface charge transfer to bonding distance. *Organic Electronics*, 9:111âĂŞ118, 2008.

[85] J. D. Baran, J. A. Larsson, R. A. J. Woolley, Y. Cong, P. J. Moriarty, A. A. Cafolla, K. Schulte, and V. R. Dhanak. Theoretical and experimental comparison of SnPc, PbPc, and CoPc adsorption on Ag(111). *Physical Review B*, 81:075413, 2010.

[86] Ingo Kroeger. *Adsorption von Phthalocyaninen auf Edelmetalloberflächen.* PhD thesis, Julius-Maximilians-Universität Würzburg, 2010.

[87] Y. Y. Zhang, S. X. Du, and H.-J. Gao. Binding configuration, electronic structure, and magnetic properties of metal phthalocyanines on a Au(111) surface studied with ab initio calculations. *Physical Review B*, 84:125446, 2011.

[88] H. Yamane, A. Gerlach, S. Duhm, Y. Tanaka, T. Hosokai, Y. Y. Mi, J. Zegenhagen, N. Koch, K. Seki, and F. Schreiber. Site-Specific Geometric and Electronic Relaxations at Organic-Metal Interfaces. *Physical Review Letters*, 105:046103, 2010.

[89] D. G. de Oteyza, A. El-Sayed, J.M. Garcia-Lastra, E. Goiri, and T. N. Krauss. Copper-phthalocyanine based metal-organic intervades: The effect of fluorination, the stubstrate, and its symmetry. *The Journal of Chemical Physics*, 133:214703, 2010.

[90] I. Kröger, B. Stadtmüller, C. Kleimann, P. Rajput, and C. Kumpf. Normal-incidence x-ray standing-wave study of copper phthalocyanine submonolayers on Cu(111) and Au(111). *Physical Review B*, 83:195414, 2011.

[91] I. Kröger, B. Stadtmüller, C. Stadler, J. Ziroff, M. Kochler, A. Stahl, F. Pollinger, T.-L. Lee, J. Zegenhagen, F. Reinert, and C. Kumpf. Submonolayer growth of copper-phthalocyanine on Ag(111). *New Journal of Physics*, 12:083038, 2010.

[92] I. Chizhov, G. Scoles, and A. Kahn. The Influence of Steps on the Orientation of Copper Phthalocyanine Monolayers on Au(111). *Langmuir*, 16:4358–4361, 2000.

[93] B. Stadtmüller, I. Kröger, F. Reinert, and C. Kumpf. Submonolayer growth of CuPc on noble metal surfaces. *Physical Review B*, 83:085416, 2011.

[94] E. Mete, I. Demiroglu, M. F. Danisman, and S. Ellialtioglu. Pentacene Multilayers on Ag(111) Surface. *The Journal of Physical Chemistry C*, 114:2724–2729, 2010.

[95] M. Koudia, M. Abel, C. Maurel, A. Bliek, D. Catalin, M. Mossoyan, J.-C. Mossoyan, and P. Louis. Influence of Chlorine Substitution on the Self-Assembly of Zinc Phthalocyanine. *The Journal of Physical Chemistry. B*, 110:10058–10062, 2006.

[96] A. Sandy, S. Mochrie, D. Zehner, and D. Gibbs K. Huang. Structure and phases of the Au(111) surface: X-ray-scattering measurements. *Physical Review B*, 43:4667–4687, 1991.

[97] M. M. Dovek, C. A. Lang, J. Nogami, and C. F. Quate. Epitaxial growth of Ag on Au(111) studied by scanning tunneling microscopy. *Physical Review B*, 40:11973, 1989.

[98] P. Statiris, H. C. Lu, and T. Gustafsson. Temperature dependent sign reversal of the surface contraction of Ag(111). *Physical Review Letters*, 72:3574, 1994.

[99] M. Greif, L. Castiglioni, A. P. Seitsonen, S. Roth, J. Osterwalder, and M. Hengsberger. Photoelectron diffraction in the x-ray and ultraviolet regime: Sn-phthalocyanine on Ag(111). *Physical Review B*, 87:085429, 2013.

[100] C. Stadler, S. Hansen, F. Pollinger, C. Kumpf, E. Umbach, T.-L. Lee, and J. Zegenhagen. Structural investigation of the adsorption of SnPc on Ag(111) using normal-incidence x-ray standing waves. *Physical Review B*, 74:035404, 2006.

[101] R. A. J. Woolley, C. P. Martin, G. Miller, V. R. Dhanak, and P. J. Moriarty. Adsorbed molecular shuttlecocks: An NIXSW study of Sn phthalocyanine on Ag(111) using Auger electron detection. *Surface Science*, 601:1231–1238, 2007.

[102] . *The Journal of Chemical Physics*.

[103] R. Ahlrichs, M. Bär, M. Häser, H. Horn, and C. Kölmel. Electronic structure calculations on workstation computers: The program system turbomole. *Chemical Physics Letters*, 3:165–169, 1989.

[104] A. Gerlach, T. Hosokai, S. Duhm, S. Kera, O. T. Hofmann, E. Zojer, J. Zegenhagen, and F. Schreiber. Orientational Ordering of Nonplanar Phthalocyanines on Cu(111): Strength and Orientation of the Electric Dipole Moment. *Physical Review Letters*, 106:156102, 2011.

[105] Y. L. Huang, W. Chen, F. Bussolotti, T. C. Niu, A. T. S. Wee, N. Ueno, , and S. Kera. Impact of molecule-dipole orientation on energy level alignment at the submolecular scale. *Physical Review B*, 87:085205, 2013.

[106] T. Niu, M. Zhou, J. Zhang, Y. Feng, and W. Chen. Dipole Frientation Dependent Symmetry Reduction of Chloraluminum phthalocyanine on Cu(111). *The Journal of Physical Chemistry C*, 117:1013–1019, 2013.

[107] J. Zegenhagen. Surface structure determination with X-ray standing waves. *Surface Science Reports*, 18:202–271, 1993.

[108] J. Lüdecke, S. Skordas, G. J. Jackson, D. P. Woodruff, R. G. Jones, B. C. C. Cowie, R. Ithnin, and C. A. Papageorgopoulos. Structural study of Rb and Cl coadsorption on Cu(111): a case of overlayer compound formation. *Journal of Physics: Condensed Matter*, 9:4593, 1997.

[109] G. Witte, S. Lukas, P. S. Bagus, and C. Wöll. Vacuum level alignment at organic/metal junctions: "Cushion" effect and the interface dipole. *Applied Physics Letters*, 87:263502, 2005.

[110] T. Körzdörfer, S. Kümmel, N. Marom, and L. Kronik. When to trust photoelectron spectra from Kohn-Sham eigenvalues: The case of organic semiconductors. *Physical Review B*, 79:201205, 2009.

[111] J. P. Perdew. Self-interaction correction to density-functional approximations for many-electron systems. *Physical Review B*, 23:5048–5079, 1981.

[112] J. B. Neaton, M. S. Hybertsen, and S. G. Louie. Renormalization of Molecular Electronic Levels at Metal-Molecule Interfaces. *Physical Review Letters*, 97:216405, 2006.

[113] F. Evangelista, V. Carravetta, G. Stefani, B. Jansik, M. Alagia, S. Stranges, and A. Ruocco. Electronic structure of copper phthalocyanine: an experimental and theoretical study of occupied and unoccupied levels. *The Journal of Chemical Physics*, 126:124709, 2007.

[114] M. Gruber, G. Heimel, L. Romaner, J.-L. Bredas, and E. Zojer. First-principles study of the geometric and electronic structure of Au13 clusters: Importance of the prism motif. *Physical Review B*, 77:165411, 2008.